



University  
of Windsor

**WINSAT**

**University of Windsor Space and Aeronautics Team ([WinSAT](#)):**

**Structural & Thermal Subsystems**

Capstone Design Summer 2020

MECH-4200-B

Department of Mechanical, Automotive, and Materials Engineering

University of Windsor

August 7<sup>th</sup>, 2020

**University of Windsor Space and Aeronautics Team ([WinSAT](#)):**

**Structural & Thermal Subsystems**

**Mechanical Capstone Team**

Nirmit Khamar	104422586
Madeline McQueen	104570658
Trevor Parent	104620463
Taran Riar	104258886
Atilla Saadat	104411786
Marco Veliz Castro	104570333

Department of Mechanical, Automotive, and Materials Engineering

University of Windsor

Faculty Supervisor: Dr. Afshin Rahimi

August 7th, 2020

## SIGNATURE SHEET

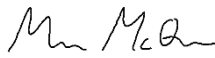
“No action by any design team member contravened the provisions of the Code of Ethics and we hereby reaffirm that the work presented in this report is solely the effort of the team members and that any work of others that was used during the execution of the design project or is included in the report has been suitably acknowledged through the standard practice of citing references and stating appropriate acknowledgments.”

Nirmit Khamar




104422586

Madeline McQueen



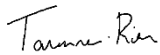
104570658

Trevor Parent



104620463

Taran Riar



104258886

Atilla Saadat



104411786

Marco Veliz Castro



104570333

## **ABSTRACT (NK)**

The University of Windsor Space & Aeronautics Team (WinSAT) is competing in the Canadian Satellite Design Challenge to design, build, test, and potentially launch a 3U cube satellite into low earth orbit. The satellite is designed to capture optical images of the earth's surface and transmit the data back down to the ground station and amateur radio operators. The WinSAT Structural and Thermal Division must design the satellite to pass several environmental and structural qualification tests, including a quasi-static acceleration test, vibrational test, thermal-vacuum test, bolt analysis and centre-of-mass validations. Using SolidWorks, multiple CAD models of all the various internal subsystems were developed as an assembly around the supporting external structure. For thermal simulations, a simplified model of the satellite was created in Siemens NX Space Systems Thermal for analysis to ensure each component is within the optimal temperature range. For the static analysis testing, the results proved that most of the stress placed by the 12g loads would be primarily on the midplane and where the rods and boards would meet. The vibrational testing will need further development in material selection to ensure the satellite model meets the fundamental frequency requirements. The thermal testing showed that each of the components meet the temperature extremes and are in the suitable operating ranges. With the changes to material selection, the satellite is structurally and thermally validated to continue with the assembly, integration, and environmental testing phase of satellite development.

## Table of Contents

SIGNATURE SHEET .....	ii
ABSTRACT ( <i>NK</i> ).....	iii
LIST OF FIGURES .....	vi
LIST OF TABLES .....	viii
LIST OF NOMENCLATURE .....	ix
1. INTRODUCTION ( <i>AS</i> ) .....	1
2. BENCHMARKING ( <i>AS</i> ).....	1
3. DESIGN CRITERIA, CONSTRAINTS, AND DELIVERABLES.....	2
3.1. EXTERNAL STRUCTURE ( <i>MM</i> ) .....	2
3.2. ANTENNA DEPLOYMENT SYSTEM ( <i>NK</i> ).....	4
3.3. PAYLOAD MODULE ( <i>MM</i> ) .....	4
3.4. REACTION WHEEL BOARD ( <i>MVC</i> ) .....	5
3.5. MAGNETORQUER BOARD ( <i>MVC</i> ) .....	5
3.6. ADCS COMPUTER BOARD ( <i>MM</i> ) .....	7
3.7. DEPLOYMENT SWITCHES ( <i>TR</i> ).....	7
3.7.1 MECHANICAL INTERFACE AND SPECIFICATIONS .....	7
3.8. SEPARATION SPRINGS ( <i>TR</i> ) .....	8
3.9. DESIGN OF SPHERICAL AIR BEARING TEST BED ( <i>MVC</i> ).....	9
3.10. DESIGN OF ELECTROMAGNETIC FIELD SIMULATOR ( <i>MVC</i> ).....	10
3.11. STRUCTURAL ASSEMBLY ( <i>MM</i> ) .....	11
3.12. THERMAL ANALYSIS ( <i>TP</i> ) .....	11
4. DESIGN METHODOLOGY .....	13
4.1. EXTERNAL STRUCTURE ( <i>MM</i> ) .....	13
4.2. ANTENNA DEPLOYMENT SYSTEM ( <i>NK</i> ).....	15
4.3. PAYLOAD MODULE ( <i>MM</i> ) .....	17
4.4. REACTION WHEEL BOARD ( <i>MVC</i> ) .....	18
4.4.1. MECHANICAL INTERFACE AND SPECIFICATIONS .....	18
4.4.2. RW BOARD MATERIAL .....	18

<b>4.5. MAGNETORQUER BOARD (MVC)</b> .....	19
<b>4.5.1. MECHANICAL INTERFACE AND SPECIFICATIONS</b> .....	19
<b>4.5.2. CORE MATERIAL</b> .....	19
<b>4.5.3. MOUNT MATERIAL</b> .....	20
<b>4.6. ADCS COMPUTER BOARD (MM)</b> .....	20
<b>4.7. DEPLOYMENT SWITCHES (TR)</b> .....	21
<b>4.8. SEPARATION SPRINGS (TR)</b> .....	23
<b>4.9. SPHERICAL AIR BEARING TEST BED (MVC)</b> .....	24
<b>4.10. ELECTROMAGNETIC FIELD SIMULATOR (MVC)</b> .....	26
<b>4.10.1. MATHEMATICAL MODELLING</b> .....	26
<b>4.10.2. MECHANICAL DESIGN</b> .....	29
<b>4.11. STRUCTURAL ASSEMBLY (MM)</b> .....	31
<b>5. MODEL IMPLEMENTATION</b> .....	33
<b>5.1. STRUCTURAL MODEL (MM)</b> .....	33
<b>5.2. THERMAL MODEL (TP)</b> .....	35
<b>6. MODEL TESTING/VALIDATION</b> .....	38
<b>6.1. STRUCTURAL MODEL</b> .....	38
<b>6.1.1. STATIC ANALYSIS (MM)</b> .....	38
<b>6.1.2. BOLT ANALYSIS (TR)</b> .....	45
<b>6.1.3. VIBRATIONAL ANALYSIS (AS)</b> .....	47
<b>6.1.4. CENTRE OF MASS VALIDATION (TR)</b> .....	49
<b>6.1.5. MOMENT OF INERTIA VALIDATION (TR)</b> .....	50
<b>6.2. THERMAL MODEL (TP)</b> .....	51
<b>7. PERFORMANCE METRICS AND SPECIFICATIONS</b> .....	55
<b>7.1. STRUCTURAL MODEL (NK+MM)</b> .....	55
<b>7.2. THERMAL MODEL (TP)</b> .....	58
<b>8. CONCLUSION (MM)</b> .....	59
<b>REFERENCES</b> .....	60
<b>APPENDIX A – COMPONENT DRAWINGS</b> .....	63

<b>APPENDIX B – STRUCTURAL SIMULATION RESULTS</b> .....	75
<b>APPENDIX C – THERMAL SIMULATION RESULTS</b> .....	79
<b>APPENDIX D – CAD MODELS</b> .....	83
<b>APPENDIX D – CODE</b> .....	84

## **LIST OF FIGURES**

Figure 1: CubeSat Structure Specification [1] .....	3
Figure 2: Magnetic hysteresis loop .....	6
<i>Figure 3: Depressed nose of retractable spring plunger</i> .....	8
Figure 4: Extended nose of retractable spring plunger .....	8
Figure 5: Deployment switch and Separation spring placement [3] .....	9
Figure 6: Contour of Earth’s magnetic field intensity at a 400 km altitude .....	11
Figure 7: Side Panel Design featuring Mass-Saving “Flower Design” .....	13
Figure 8: Segmented Threaded Spacers to Connect Rods to Top Plate .....	14
Figure 9: Midplane Connector Design .....	15
Figure 10: Solar Panel Plate Design (Viewed Horizontally) .....	15
Figure 11: Antenna Deployment System .....	16
Figure 12: Simplified Model of the ADS .....	17
Figure 13: Payload Board Assembly Design .....	18
Figure 14: ADCS Computer Board Design (View of Top Side) .....	21
Figure 15: ADCS Computer Board Design (View of Underside) .....	21
Figure 16: Microswitch Mounting Configuration .....	22
Figure 17: Microswitch Countersink Screws .....	23
Figure 18: Custom Spring Plunger (Viewed Horizontally) .....	23
Figure 19: CAD Model of Mounting Plate with 3-axis Balancing System .....	25
Figure 20: Assembly of SABTB System with Mounted ADCS Components .....	26
Figure 21: Z axis pair of coils. ....	27
Figure 22: Magnetic Field Homogeneity .....	28
Figure 23: Magnetic Field Intensity for 1 m Side Length 3-axis Helmholtz Cage .....	29
Figure 24: U-Channel Schematic from McMaster-Carr .....	30
Figure 25: CAD Model of Helmholtz Cage Assembly .....	31
Figure 26: Complete Satellite Assembly Design with Solar Panels .....	32
Figure 27: Complete Satellite Assembly Design without Solar Panels .....	33
Figure 28: Simplified Satellite Assembly (without Solar Panel Plates) .....	34
Figure 29: Simplified Thermal Assembly of External Components .....	36

Figure 30: Simplified Thermal Assembly of Internal Components .....	37
Figure 31: Thermal FEM Assembly .....	38
Figure 32: Simulation Assembly featuring Mesh, Fixtures, and Sample Loading (-Y shown) .....	39
Figure 33: Vertical Loading - Countersink Hole Stress Results Example (-Z shown) .....	40
Figure 34: Vertical Loading - Rod/Board Mating Interface Stress Result Example (+Z shown) .....	41
Figure 35: Vertical Loading - Displacement Result Example (-Z shown) .....	42
Figure 36: Horizontal Loading – Countersink Hole Stress Result Example (-Y shown) .....	43
Figure 37: Rod/Board Mating Interface Stresses in Horizontal Loading Static Simulation Results (+X shown) .....	43
Figure 38: Horizontal Loading - External Displacement Result Example (+Y shown) .....	44
Figure 39: Horizontal Loading – Internal Displacement Result Example (+Y shown) .....	44
Figure 40: Virtual Bolt .....	45
Figure 41: Bolt Connector Settings in SolidWorks .....	46
Figure 42: "Define Pin/Bolt Check Plot" Results .....	46
Figure 43: Bolt Analysis Results .....	47
Figure 44: Launch Random Vibration Qualification Environment [3] .....	48
Figure 45: Vibrational Simulation - Modal Response .....	48
Figure 46: Final Board Placement as Verified by COM Calculations .....	50
Figure 47: Maximum Temperature Results on Simulation Model for ISS Cold Case .....	53
Figure 48: Minimum Temperature Results on Simulation Model for ISS Cold Case .....	54
Figure 49: ISS Hot Case - No Internals .....	55
Figure 50: FR4 Material Parameters .....	57
Figure 51: Silicon Iron Material Parameters .....	57
Figure 52: Drawing of Payload Camera .....	63
Figure 53: Drawing of Camera Lens .....	64
Figure 54: Drawing of Lens Mount .....	64
Figure 55: Drawing of Payload Board Compute Stick .....	65
Figure 56: Drawing of DDR2 SRAM .....	65
Figure 57: Drawing of Nucleo-64 .....	66
Figure 58: Drawing of NXP .....	66
Figure 59: Retractable Spring Plunger Drawing .....	67
Figure 60: Separation Spring Plunger Drawing .....	67
Figure 61: Top Plate Drawing .....	68
Figure 62: Base Plate Drawing .....	68
Figure 63: Side Panel Left Drawing .....	69
Figure 64: Side Panel Right Drawing .....	69
Figure 65: Midplane Connector Drawing .....	70



Figure 66: Drawing of ADS.....	70
Figure 67: Solar Panel Plate Drawing.....	71
Figure 68: Camera Mount Design.....	71
Figure 69: Reaction Wheel Board Schematic .....	72
Figure 70: Magnetorquer Board Schematic .....	72
Figure 71: Reaction Wheel Schematic.....	73
Figure 72: SABTB Mounting Plate with 3-Axis Balancing System Schematic .....	73
Figure 73: SABTB Platform Schematic.....	74
Figure 74: Helmholtz Cage Schematic .....	74
Figure 75: Von-Mises Stress Plot of RW Board Under 12 g Quasi-Static Acceleration.....	75
Figure 76: Strain Plot of RW Board Under 12 g Quasi-Static Acceleration.....	75
Figure 77: Displacement Plot of RW Board Under 12 g Quasi-Static Acceleration .....	76
Figure 78: Von-Mises Stress Plot of Magnetorquer Mount Clamp w/ 5N Load .....	76
Figure 79: Strain Plot of Magnetorquer Mount Clamp with 5N Load Applied at Opening .....	77
Figure 80: Displacement Plot of Magnetorquer Mount Clamp with 5N Load Applied at Opening .....	77
Figure 81: Vertical Loading – Internal Strain Result Example (-Z shown).....	78
Figure 82: Horizontal Loading – Internal Strain Result Example (-Y shown) .....	78
Figure 83: CAD Model of SABTB Platform .....	83
Figure 84: CAD Model of Helmholtz Cage.....	83

## LIST OF TABLES

Table 1: External Structure Design Criteria [1] .....	3
Table 2: Component Operating Temperature Ranges.....	12
Table 3: ADCS component material comparison .....	18
Table 4: Magnetic Material Property Comparison.....	20
Table 5: Outgassing mass properties of the microswitch [41] .....	22
Table 6: Specifications of A-651 Air Bearing Module from Nelson Air [42].....	24
Table 7: Coil Parameters Required for Desired Field Homogeneity. ....	28
Table 8: Centre of Mass Values.....	49
Table 9: MOI Values at COM .....	50
Table 10: MOI Values at COM Aligned with Output Coordinate System .....	51
Table 11: MOI Values at Output Coordinate System .....	51
Table 12: Power conversions from electrical to thermal energy.....	52
Table 13: Von Mises Stresses and Displacements Obtained in Quasi-Static Analysis .....	56
Table 14: Material properties used for Each Component in Static Analysis .....	56
Table 15: Material Properties used for Thermal Modelling.....	58

Table 16: Optical Properties used for Thermal Modelling .....	58
Table 17: Temperature Range Results for ISS Hot Case .....	79
Table 18: Temperature Range Results for ISS Cold Case .....	80
Table 19: Temperature Range Results for Sun-Synchronous Hot Case .....	81
Table 20: Temperature Range Results for Sun-Synchronous Cold Case .....	82

## LIST OF NOMENCLATURE

ADCS	Attitude Determination and Control System
ADS	Antenna Deployment System
AIT	Assembly, Integration, and Testing
CAD	Computer Aided Design
CDR	Critical Design Review
COG	Centre of Gravity
COM	Centre of Mass
COR	Centre of Rotation
COTS	Commercial-Off-The-Shelf
CSA	Canadian Space Agency
CSDC	Canadian Satellite Design Challenge
CVCM	Collected Volatile Condensable Material
DIETR	Design, Interface, and Environmental Testing Requirements
DDR2 SRAM	Double Data Rate 2 Synchronous Dynamic Random-Access Memory
FEM	Finite Element Method
FOS	Factor of Safety
FR4	Flame Retardant 4 (material for printed circuit boards)
IR	Infrared Radiation
ISS	International Space Station
ITU	International Telecommunications Union
LEO	Low Earth Orbit
MBM2	Motherboard Module 2
MOI	Moment of Inertia
NASA	National Aeronautics and Space Administration
OBC	On Board Computer
PC-104	Standardized Small Computing Modules
PCB	Printed Circuit Board
PET	Polyethylene Terephthalate

PPOD	Poly-Picosatellite Orbital Deployer	
RF	Radio Frequency	
RW	Reaction Wheel	
SABTB	Spherical Air Bearing Test Bed	
SMAD	Space Mission Analysis and Design	
TML	Total Mass Loss	
UHF	Ultra-High Frequency	
VHF	Very High Frequency	
WinSAT	University of Windsor Space & Aeronautics Team	
$B_r$	Retentivity magnetic flux density	T
$B_{sat}$	Saturation magnetic flux density	T
$dl$	infinitesimal length wire	m
$H_c$	Coercivity magnetic field strength	A/m
$H_{sat}$	Saturation magnetic field strength	A/m
$I$	current	mA
$\hat{r}$	unit vector of distance between the point where the magnetic field is evaluated and the infinitesimal wire position	m
$\hat{u}$	unit vector orthogonal to both $dl$ and $\hat{r}$	m
$z$	distance between the point where the magnetic field is evaluated and the infinitesimal wire position	m
$\theta$	angle between $dl$ and $\hat{r}$	Rad
$\mu$	magnetic permeability	H/m
$\mu_i$	Initial magnetic permeability	H/m
$\mu_{max}$	Maximum magnetic permeability	H/m

## **1. INTRODUCTION (AS)**

WinSAT is a university engineering team currently competing in the CSDC. This competition iteration, ranging from 2018-2020, involves universities from across Canada tasked with designing, building, testing, and potentially launching a 3U cubic satellite (CubeSat) for LEO. CubeSats are measured in a standard unit; a single unit, “U”, is designated as a cube of approximately 10x10x10 cm. The CSDC requires a 3U cube satellite to be designed sized at 34.05x10x10 cm [1]. These satellites must contain all the necessary subsystems, health monitoring, redundancies, and components to carry out its mission objectives in orbit. WinSAT has presented the CubeSat designs at the CSDC CDR at ABB Bomem in October 2019. After a comprehensive analysis of our designs from competition judges, WinSAT placed first place in the CDR and now leads the competition moving into the environmental testing originally slated for late June 2020 [2].

WinSAT’s satellite development has been divided into seven different organizational and engineering divisions: Attitude Determination and Control Systems, Business, Command and Data Handling, Payload, Radio Communications, Structural, and Thermal. This capstone group and report will focus on the goals, research, designs, deliverables, and results from the Structural and Thermal subsystems of the satellite. As with all of the various subsystem development processes, the structural and thermal designs must consider the requirements and constraints set out by all the related stakeholders, the CSDC, WinSAT’s selected payload mission objectives, and the other satellite subsystems, as described in Section 3. The general objectives for the structural subsystem are to provide sufficient structural support for all internal subsystems, withstanding the launch environment and material stresses, whilst custom designing to adhere to internal component sizing, mounting, and maintaining overall required dimensions. The thermal subsystem will, ideally, passively control the satellite’s component temperatures to maintain operational temperature ranges through component placement and material selection.

## **2. BENCHMARKING (AS)**

An extensive literature review has been conducted throughout the design process of the CubeSat for research and development purposes. A variety of designs and configurations exist for nano satellites from various universities, companies, and space agencies around the world. Through the review of documents released by these satellite developers, the formulations, procedures, components, and design practices used for state-of-the-art CubeSats were studied

During the beginning of design phase, 3U CubeSat design standards drawn from the CSDC General Rules and Requirements [1] and DIETR [3]. These two documents explain the basic satellite orbital scenarios, dimensions, operational conditions, testing qualifications, and primary payload objectives. The rules and regulations for the CSDC were taken above all other satellite design procedures, as it pertains directly to the competition, and thus takes precedence over practices possibly used on other CubeSats. The nanosatellite development practices from the Canadian Space Agency was reviewed to comply with possible launch opportunities from CSA and due to the existing relationship between the CSDC and CSA [4].

The guidelines from the CSA are also relevant to our designs as the environmental testing of the satellite (the final milestone of the CSDC) takes place at the David Florida Laboratory, a CSA AIT facility in Nepean, Ontario, Canada. Spacecraft systems engineering standards were mainly derived from the Space Mission Analysis and Design textbook [5], which aided the subsystem development through step-by-step design procedures. Bolt analysis standards were derived from NASA's Requirements for Threaded Fastening Systems in Spaceflight Hardware [6]. The Warsaw University of Technology has released several design reviews regarding their in-orbit satellite PW-SAT2, designed to mitigate space debris, which was reviewed to assess satellite development expectations and challenges for university teams [7]. The initial theoretical calculations for nano satellite thermal analysis was derived from the thermal analysis report for California Polytechnic State University's CubeSat CP3 project [8].

The listed literature and state-of-the-art CubeSat developments are just a small fraction of information gathered during the research phase of our satellite development. Other sources included in-person discussions with satellite developers during CSDC workshops attended by WinSAT members. These events include the CSDC Peer-Design Review (Montreal Space Symposium 2019) and the CSDC Structural and Thermal Analysis Workshop (Magellan Aerospace in Winnipeg, Alberta, Canada). With the benchmarking and information gathering of in-orbit and in-development CubeSat systems, the chosen procedures, materials, components, and practices to meet our mission objectives are outlined in the subsequent sections.

### **3. DESIGN CRITERIA, CONSTRAINTS, AND DELIVERABLES**

#### **3.1. EXTERNAL STRUCTURE (*MM*)**

The external structure of the satellite is arguably the most important component of the satellite as it lays the foundation for which the internal components are housed in. The CSDC

guidelines lay out many design criteria which the external structure must adhere to. The external structure dimensional requirements and structural constraints are shown below in Figure 1 and Table 1 respectively.

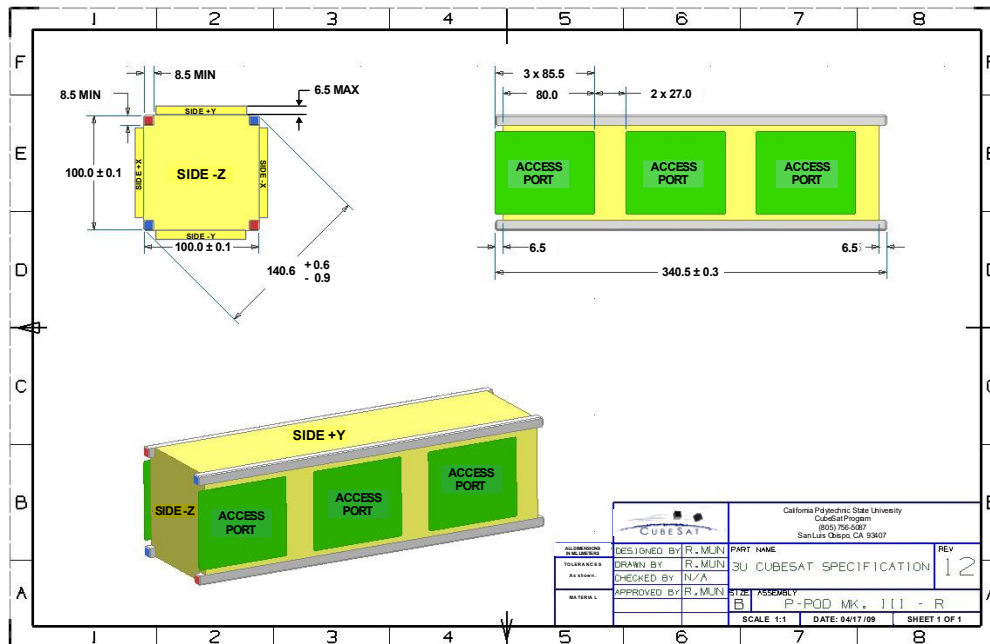


Figure 1: CubeSat Structure Specification [1]

Along with satisfying these constraints, the external structure must also be able to withstand the loading and vibrations to be exerted upon the satellite during the launch phase, validated through simulation and physical testing. These processes will be described further into this report.

Table 1: External Structure Design Criteria [1]

Criteria	Description
Configuration and Dimensions	The spacecraft configuration and physical dimensions shall be per Figure 1. This size and configuration are the standard of a 3U CubeSat. These dimensions apply to the spacecraft in the stowed (launch) configuration only.
Co-ordinate System	The spacecraft shall use the co-ordinate system as defined in Figure 1. The -Z face of the spacecraft will be inserted first into the PPOD.
Spacecraft Structure Material	Aluminium 7075, 6061, 5005, and/or 5052 shall be used for both the main spacecraft structure and the corner rails.
Corner Rails	The spacecraft shall have four rails, one per corner, along the Z axis. Rail surfaces that contact the launch dispenser guide rails shall have a hardness equal to or greater than hard-anodized aluminium.
Corner Rail Roundness	The edges of the spacecraft corner rails shall be rounded to a radius of at least 1.0 mm.

### **3.2. ANTENNA DEPLOYMENT SYSTEM (NK)**

The antenna deployment system is a combination of many individual parts that will assist with releasing the four antennas to allow for communications to the ground station. The ADS is situated at the Z+ face of the CubeSat, as such design constraints exist limiting the component thickness. The entire CubeSat must be a maximum of 34.05 cm in length which limits the height of any one component. In general, the ADS is composed of three main components and many individual sub-components. The main components include an aluminium base plate, a PCB and a cover plate. The entire ADS rests onto the top plate thus the positioning of the holes must be aligned through the four corners of the ADS.

The sub-components must create enough space so that every electrical component can go through and attach properly to the transceiver board. The RF team needed the exact design specifications so that they would accurately be able create RF traces and connections for the antenna release PCB. With the addition of four brackets that would hold the antennas in place in a coiled position, the required dimension spacing would need to be fixed to hold the other electrical components in place. The main electrical components are the balun transformers, U.FL connectors, and the switches.

The design specifications of the antennas themselves are decided based upon the required gain and operating frequency. The length of the antennas is determined by the wavelength. The antenna system is comprised of two UHF and two VHF antennas. The UHF uplink antennas have a 145MHz frequency and the VHF downlink antennas have a 437MHz frequency. These radio bands were chosen as they meet the ITU regulations for LEO communications in the allowable amateur radio frequencies. [9]

### **3.3. PAYLOAD MODULE (MM)**

The payload module consists of all components involved with capturing, processing, and transmitting photographs taken by the satellite. With the direction of the Payload team, who has done intensive analysis on the capturing and processing capabilities required, the structural team is given the specifications of the COTS to model into an assembly. The payload assembly once again uses a base PCB which follows the PC-104 board specification as it will be one of the internal components stacked using the rods. On the PCB, there are to be COTS components that were selected after analysis from the payload team. These components include: two cameras, their appropriate lenses, lens mounts, a DDR2 SDRAM component, and a Raspberry Pi Compute Module. A visual representation of these components and their

dimensions can be found in Figures 52-56 in Appendix A. From this point, the required design criterion is to create a sturdy board which houses all necessary components, has dimensions which fit within the allotted assembly space, and can withstand the required loading. In addition, a mounting bracket is required to transfer excess loading experienced by the vertically placed cameras to the external structure. This ensures that the cameras do not experience an excessive amount of stress.

### **3.4. REACTION WHEEL BOARD (MVC)**

Satellite pointing maneuvers are usually accomplished by the rotation of a solid mass known as RW. They induce a rotational inertia for maneuvering and momentum storage. RWs offer a high degree of pointing precision, with regards to attitude control, but are limited by the wheel saturation after continuous use, making the use of magnetorquers mandatory for momentum control. The RWs are desaturated by the magnetorquers in a process called momentum dumping [10].

The RW design proposed for this project consists of Aluminum 6061-T6 cylinders that are fitted onto the shaft of an EC-20 Maxon DC motor. The choice for this motor was limited to space ready, inexpensive commercial motors with low power consumption. The motor specifications and wheel material were received from the ADCS team. The RW were sized to provide maximum momentum and to fit within the PC-104 spec board dimensions. Typically, 3 RWs provide control in all directions. However, a fourth wheel will be used in a pyramid configuration for fault-tolerance control in case of a single RW failure [11].

Finally, the structure of the RW board must be made of a material capable of withstanding a 12G quasi-static acceleration without excessive deformation and without the material yielding.

### **3.5. MAGNETORQUER BOARD (MVC)**

Magnetorquers are devices that create a magnetic dipole moment from the interaction between the spacecraft's magnetorquers and the earth's magnetic field. Magnetorquers are long copper wires wound around an iron-ferrite core [12]. Given that there is an inverse proportionality to the third power between the dipole moment and the orbital altitude [13], magnetorquers are typically used as attitude control system actuators for low earth orbit satellites. Magnetorquers are an effective method for attitude control at low earth orbit because they have inherent advantages, offering simplicity, reliability, and cost effectiveness [12]. Therefore, a magnetorquer with a large output torque, low residual moment, small size,



and low weight is designed. However, this report is only concerned with the mechanical and material aspects of the magnetorquer design.

Generally, satellites employ three orthogonally mounted magnetorquers to induce a magnetic dipole in all body axes directions [12]. Therefore, the shape and orientation of the magnetorquer design must employ a combination of torquerods and aircore to provide control about the three body axes.

When a ferromagnetic material is placed in a coil of wire with current flowing through it, the magnetic field strength  $H$  generated by the coil causes the atoms in the material to align with the field. The purpose of this is to increase the magnetic flux density  $B$ . However, this does not occur instantaneously, but rather the aligning process lags behind the magnetizing field [14]. Increasing  $H$  of the magnetizing field gradually, results in  $B$  eventually reaching a saturation point where all the atoms in the material have aligned with the induced magnetic field. If  $H$  is then decreased,  $B$  will decrease but lagging behind  $H$ . However when  $H$  is decreased back to zero,  $B$  will still have a positive value known as retentivity [14].  $B$  will not reach a value of zero until  $H$  has reached a certain negative value known as the coercive force [14]. Further decreasing  $H$  in the negative direction will cause  $B$  to eventually reaching a saturation limit again but in the opposite direction. This cycle can be continued to form a closed loop which can be seen in Figure 2. This loop is called a hysteresis loop.

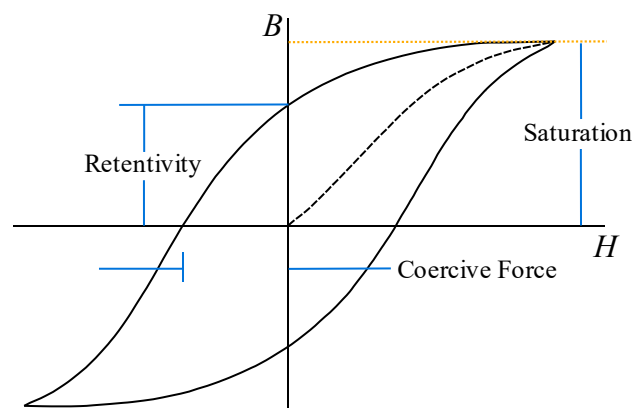


Figure 2: Magnetic hysteresis loop

There are energy and heat losses associated with the reversing of the magnetization of a material which are called hysteresis losses. These losses are proportional to the area of the hysteresis loop [14]. Therefore, to reduce the energy waste in the form of heat, the cores of the magnetorquer rods shall be designed with a material with a narrow hysteresis loop.

Finally, the supports to hold the torque rods in place shall be designed in a manner that will allow for easy installation. The material selected for the magnetorquer board must be light and withstand a quasi-static acceleration of 12G's without excessive deformation.

### **3.6. ADCS COMPUTER BOARD (*MM*)**

The ADCS Computer Board must use algorithms developed by the ADCS team to control the ADCS actuators (RW's and magnetorquers). With the direction of the ADCS team, the structural team is given the names of the COTS to model into an assembly. The main component of this board is a COTS computer called Nucleo-64 which is connected to a standard PC-104 stacking board. On the underside, there is an additional component called NXP. A visual representation of these components and their dimensions can be found in Figures 57-58 in Appendix A. From this point, the required design criterion is to create a sturdy board which houses all necessary components, has dimensions which fit within the allotted assembly space, and can withstand the required loading.

### **3.7. DEPLOYMENT SWITCHES (*TR*)**

A deployment switch must be able to keep the satellite off when needed, as well as eject the CubeSat from a carrier called P-POD. The P-POD will be attached to the launch vehicle which will transport the satellite to the appropriate orbit altitude. During the launch, all electrical systems on the satellite need to be inactive [3]. This is to ensure that no electrical or RF interference from the satellite components will occur. Once the satellite is ejected from the launch vehicle, the electrical systems will turn on and the deployment timer is started. To implement this strategy, electrical microswitches are needed. The official CSDC guidelines require the use of minimum three mechanical deployment switches, and at least one deployment switch needs to be on the Z rail standoffs. Figure 1 shows the location of the Z face and the rails.

#### **3.7.1 MECHANICAL INTERFACE AND SPECIFICATIONS**

Based on the CSDC guidelines, two deployment switches are placed on the Z-rail standoffs and one deployment switch of the roller variety is placed on the corner rail. The microswitches on the Z-rail standoffs need to be actuated, a retractable spring plunger (Figure 59 in appendix A) is used to provide mechanical input to the switch. The retractable spring is required to have a maximum end force below 3N.

When the satellite is placed in the P-POD, the nose of the plunger is depressed and sits flush with the surface as seen in Figure 3. During this state, the microswitch is actuated and all electrical systems on the satellite stay inactive. Once the satellite is ejected, the nose of the spring plunger extends as seen in Figure 4, causing the lever of the microswitch to release to its de-actuated position which triggers the electrical systems to turn on.

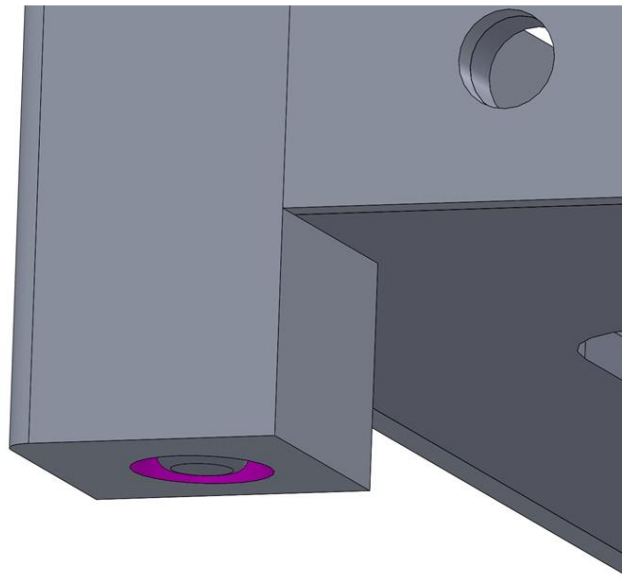


*Figure 3: Depressed nose of retractable spring plunger*

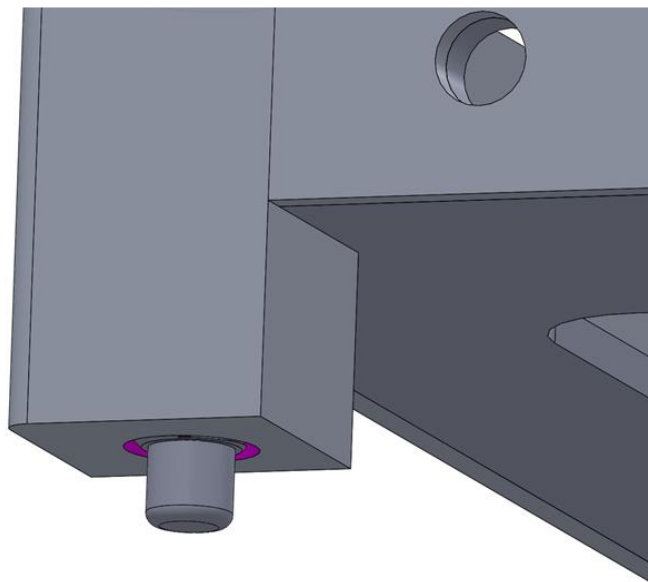


*Figure 4: Extended nose of retractable spring plunger*

### **3.8. SEPARATION SPRINGS (TR)**

The elastic potential energy inside the separation springs provide the force necessary for the satellite to be ejected from the P-Pod. CSDC guidelines require the presence of two

separation springs on the Z face of the satellite, two spring plungers (shown in Figure 60 in Appendix A) will be placed diagonally on the corner rails as shown in Figure 5. Like the retractable spring plunger used in the deployment switch mechanism, the end force exerted by each spring plunger cannot exceed 3.34N. The separation springs also operate similarly to the retractable spring plunger, once the satellite is placed inside the P-Pod the nose of the spring plunger is compressed and the elastic potential energy is stored within the spring. Once the P-Pod door opens, the spring force from the separation springs and the retractable spring plunger push the satellite out of the P-Pod.

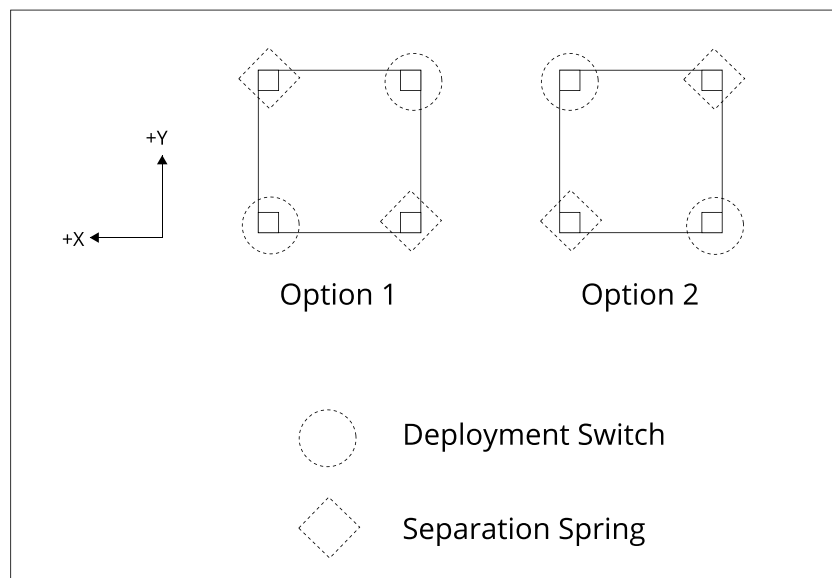


Figure 5: Deployment switch and Separation spring placement [3]

### 3.9. DESIGN OF SPHERICAL AIR BEARING TEST BED (MVC)

A SABTB utilizes a spherical air bearing to simulate weightlessness, to test the ADCS control systems of a spacecraft. Spherical air bearing systems are composed of a small singular semi-spherical bearing that is suspended on top of a thin layer of clean dry air [15].

The proposed SABTB system will experience torque-free motion and be capable of movement about the principal axes. The ADCS components to be tested will be placed on top of a platform mounted to the semi-spherical air bearing. However, the mounting of these components causes a misalignment in the COG and COR, introducing gravitational torques that affect the weightlessness simulation [16].

To achieve the desired torque-free motion, the COG and COR of the system with the mounted ADCS components must be aligned, and this is done with a precise balancing system [16]. The need for this precise balancing makes the design of the SABTB complex and requires

careful design considerations to ensure modifications are possible for multiple ADCS component configurations. Additionally, the balancing system and process is designed to be robust and simple.

The construction of the air bearing itself is the most complicated part of the entire SABTB system. Manufacturing of an air bearing requires special dedicated machinery and is not available for the WinSAT team to use. Due to this, the air bearing and air supply system are COTS components. Apart from the air bearing, all the other components of the SABTB system are custom designed but made from COTS materials.

### **3.10. DESIGN OF ELECTROMAGNETIC FIELD SIMULATOR (MVC)**

A Helmholtz cage is a device that can produce a controlled magnetic field. It is composed of two parallel coils. If the coils are symmetric and are placed sufficiently close to each other, it is possible to generate a uniform magnetic field in one direction [17]. In order to generate a magnetic field in the three dimensions, three orthogonal coil pairs are required, one pair per axis. The Helmholtz cage is paired with the air-bearing platform previously described. The aim of this system is to provide a testing facility for ADCS control algorithms.

The main requirement of the proposed Helmholtz cage is the capability of generating the magnetic field of a LEO. Earth's Magnetic Field intensity decreases with the altitude [13]; therefore, if the Helmholtz cage can recreate the field at very low altitudes, it will also be able to recreate the field at higher altitudes. For this project, the CSDC outlines that the competitors must design their satellites to operate in an altitude range of 400 to 800 km. A 400 km altitude is studied, and the magnetic field intensity, in this case, is shown in Figure 6. The field distribution shown in this figure is only an approximation since Earth's magnetic field is not constant and changes slowly.

As seen in Figure 6, the maximum magnetic field intensity observed at the altitude of 400 km is approximately 50000 nT; this means that, for any orbit simulation, the Helmholtz cage must be capable of producing a magnetic field intensity of this value at a minimum with the combined effects of all coils.

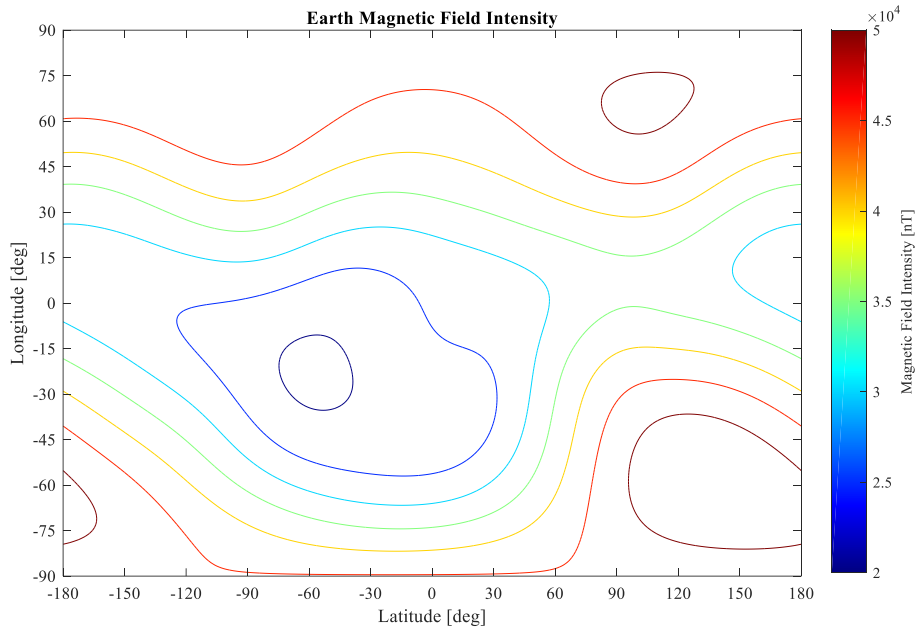


Figure 6: Contour of Earth's magnetic field intensity at a 400 km altitude

Additionally, the Helmholtz cage must be capable of nullifying the magnetic field in the testing environment. In short, the Helmholtz cage must be able to generate the magnetic field of the testing environment and the desired orbit magnetic field simultaneously.

Finally, the airbed will be positioned at the centre of the Helmholtz cage. The magnetic field measured at this location is to be uniform and solely depend on the current orbital position simulated. In summary, the magnetic field generated at the centre of the Helmholtz cage must have ample homogeneity in a region that encompasses the entirety of the ADCS components.

### 3.11. STRUCTURAL ASSEMBLY (MM)

The complete structural assembly must consist of all components described above in their appropriate locations. The placement of all internal components is to be determined by the COM calculations. This is because, as defined by the CSDC, the COM of the satellite must not be located more than 2.0 cm from the spacecraft's geometric centre in the X and Y axes, and not more than 7.0 cm from the spacecraft's geometric centre in the Z axis [18]. The assembly must also feature all bolts and nuts used to construct the satellite. The placement and type of screw required must be estimated during design and then confirmed by the bolt analysis during model testing and validation.

### 3.12. THERMAL ANALYSIS (TP)

An accurate thermal analysis of the satellite is needed to ensure the satellite components maintain their functionality throughout the satellite's lifetime. The satellite consists of several

components, each of which must be maintained within a specific temperature range during operation. Included in these ranges are an operating range, which a component must stay within during its operation, and a survival range, which a component must always remain within. Temperatures experienced outside of the operating range can lead to communication or accuracy errors, while temperatures outside the survival range can lead to critical failures causing permanent damage. Since the satellite is always considered operational throughout its orbit, the operating temperature ranges were used as the design restrictions for this analysis.

The goal of the thermal analysis is to acquire the minimum and maximum temperatures experienced by each component for various orbital conditions. The two orbits of interest were sun-synchronous and ISS orbits. These orbits were analysed since the satellite is required to survive these scenarios as required by the CSDC specifications. The temperature extremes recorded from these analyses will be compared to the required temperatures for operational stability, as shown below in Table 2. If the temperatures observed during the simulations surpass the operating ranges, several passive thermal control devices can be employed to the satellite design, such as changes to the surface finishes of materials as well as the addition of insulation materials.

*Table 2: Component Operating Temperature Ranges*

Component	Operating Minimum (°C)	Operating Maximum (°C)
Solar Cell [19], [20]	150	-80
ADCS Chip [21]	85	-40
MBM2 Chip [22]	85	-40
Beagle Bone Black [23]	90	-40
Payload Chip [24]	80	-25
Battery [25]	50	-10
Cameras [26]	55	-10
RW Motors [27]	100	-40
Iron Ferrite [28]	90	-55
FR4 [29]	100	-85
Aluminum 6061-T6 [30], [31]	583	-200
PET [32]	130	-60

Following the completion of the thermal analysis, the extreme temperature values were observed to lie within the operating range for each component. These results are discussed in section 6.2.

## 4. DESIGN METHODOLOGY

### 4.1. EXTERNAL STRUCTURE (MM)

The chosen external structure design is a straightforward yet effective design that features only two side panels, as well as top/bottom plates. Many other CubeSat designs utilize four side panels, but the chosen design can achieve the required support with only two side panels which is beneficial for a less complex structure. This is because the panels are designed with integrated corner rails and the structure wraps around to the unsupported face, giving each corner an “L-shaped” look. The four major components of the external structure (two side panels, top plate, and bottom plate) are connected using a total of sixteen M3 counterbore screws (as verified by the bolt analysis).

The design of the main components conforms to the CSDC specifications in terms of dimensioning and material selection, but they were designed to minimize mass while preserving strength. This was accomplished through a “flower design” of strategically placed holes on the side panels and top and bottom plates. The “petals” are triangles with rounded edges to secure the sturdiness that triangles provide in a design, while the curves ensure that manufacturing using a CNC machine would be possible. A depiction of this design choice can be seen below in the side panel design in Figure 7.

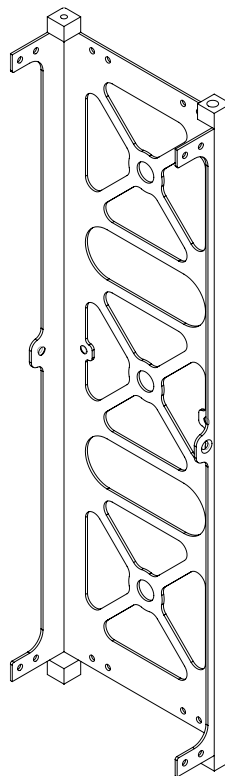


*Figure 7: Side Panel Design featuring Mass-Saving “Flower Design”*



As mentioned in the design criteria, the main satellite structure must be made of one or more of the following materials: Aluminium 7075, 6061, 5005, and 5052. The team has chosen Aluminium 6061 for the entirety of the structure because it has the least amount of material out-gassing of the given options [33].

The selected external structure design also features vertical threaded rods which attach to the top and bottom plates. To screw the rods to the top and bottom plates simultaneously, the bottom plate has an integrated threaded hole which the rods are simply screwed into. Then, there are threaded spacers which screw onto the top of the rods. These threaded spacers are segmented so it can fit M3 on the bottom (for the rods) and M3.5 on the top (for countersink screws connecting the spacer and the top plate). A wireframe image of one of the segmented threaded spacers and its dimensions can be seen below in Figure 8 so that the difference in hole size on each end can be seen.

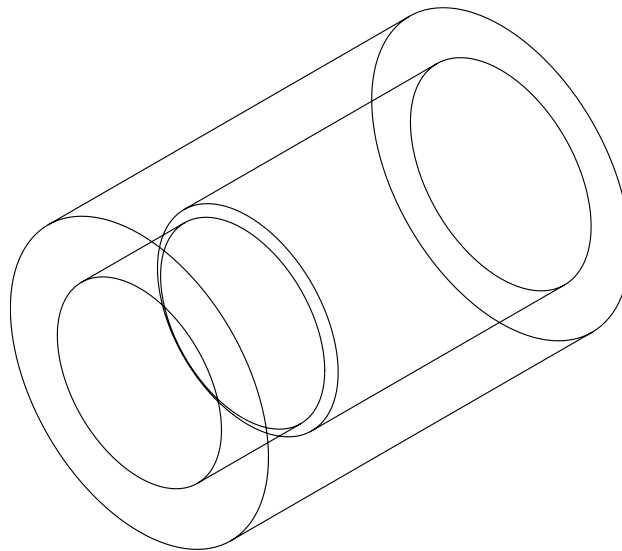


*Figure 8: Segmented Threaded Spacers to Connect Rods to Top Plate*

Additional components of the external structure include two “midplane connectors” to provide support and prevent excess stresses or deflections in the centre of the structure. They are attached to the side panels using 8 M3 countersink screws. The midplane connectors are also important to the stability of the payload board which will be discussed later in this report. The design and dimensions of these connectors can be seen below in Figure 9.

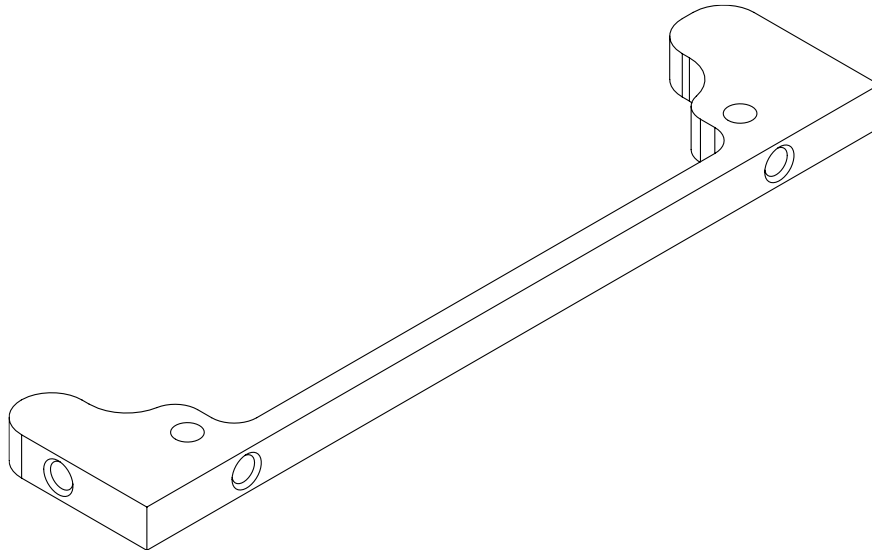


*Figure 9: Midplane Connector Design*

The last component of the external structure are the solar panel plates. These plates have been extensively analysed and designed by the electrical teams, but for mechanical purposes are simply thin sheets of FR4 which cover four sides of the satellite. These plates are connected to the side panels using an additional 16 counterbore screws. Figure 10 shows one of the plates, where 2 different sized holes can be seen in each corner. The larger set of holes is to fit the head of the bolt which connects the side panels to the top/bottom plate, and the smaller holes are to connect the solar panel plate to the side panel.

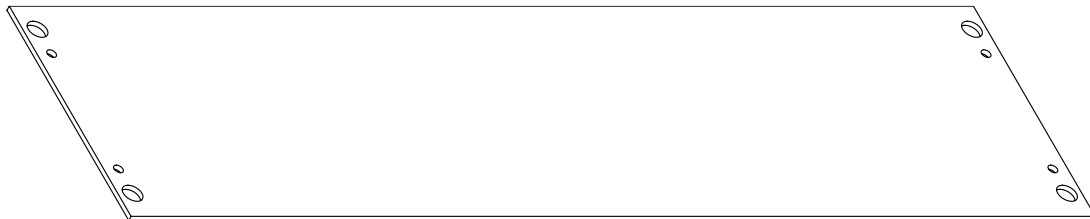


*Figure 10: Solar Panel Plate Design (Viewed Horizontally)*

For further reference, more detailed drawings of the external components (including dimensions) can be found in Figures 61-66 of Appendix A.

#### **4.2. ANTENNA DEPLOYMENT SYSTEM (NK)**

The antenna deployment system is modelled and designed using SolidWorks. The antenna deployment system has a multitude of different electrical and mechanical components attached by either M2 screws or soldered onto the PCB component. In many competitions, about 51% of teams fail due to power, mechanical, and communications failure, therefore extensive consideration was taken for the ADS[34]. The overall design is shown in Figure 11.

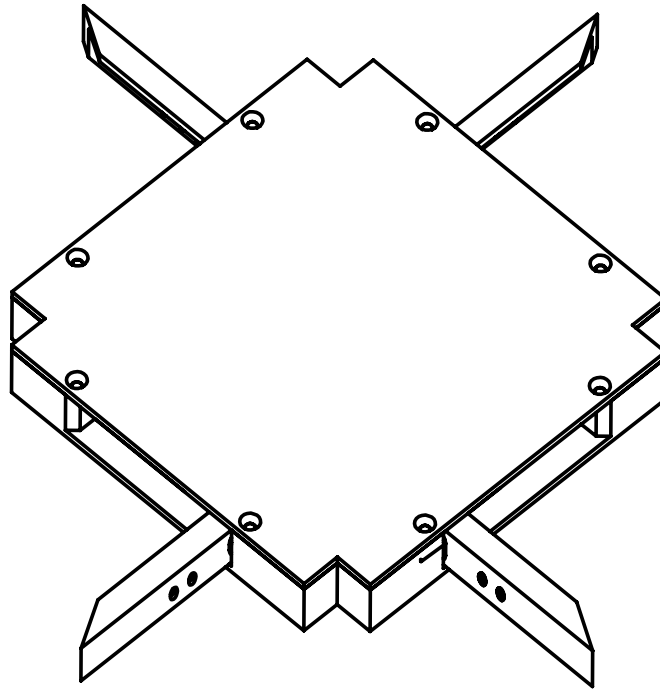


*Figure 11: Antenna Deployment System*

The release mechanism for the antennas will rely on the brackets to place the antennas in a coiled position. These antennas will not move out of place due to the brackets and the antenna doors, which are held in by tension using a burn wire. Previously, there were ideas of using resistors instead of nichrome wire, but with the testing done by the RF team, nichrome wire was a suitable substitute instead of resistors. For each bracket containing the antennas, they each contain a lever switch that is soldered onto the PCB. This switch will turn on based on the information received from the transceivers. Once the lever switch turns on, a current will pass through and cause the nichrome wire to heat up and burn the wire attached to the door to allow the antennas to be released. For there to be enough tension, a spring was placed that would have the burn wire attached which will wrap around a corner rail and pass through the nichrome wire.

A simplified model of the ADS was constructed for simulation and testing. This simulation model would not contain any electrical components such as the switches, UFL connectors, balun connectors, and the PCB. This is shown in Figure 12.

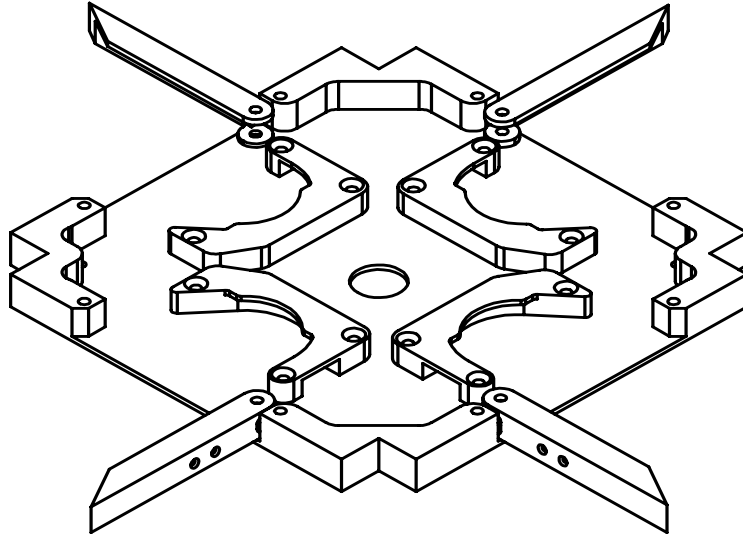


*Figure 12: Simplified Model of the ADS*

### **4.3. PAYLOAD MODULE (MM)**

Starting at the base of the module, the PCB has the DDR2 soldered onto it. In turn, the DDR2 and the compute stick are attached together, and the compute stick also rests on a section of the PCB which protrudes to the correct height. This design avoids cantilever forces on the compute stick. The cameras are connected to the PCB by 90-degree male pin headers with eight pins which are in turn electrically connected to other critical satellite components. Attached to the front face of each camera are appropriately sized lens mounts, as each camera uses a different sized lens. Once the lens is attached to the lens mount, the payload board set up is complete. The complete board assembly can be seen below in Figure 13. In addition to the primary payload components, there must be structural components used to support the vertically placed cameras by attaching them to the external structure. This is done with a custom camera mount which has been designed to attach to the back of the camera and wrap over the top to meet the external structure. This mount will be made of the same material that was chosen for the external structure, Aluminium 6061. The mounts will be attached using two M3 screws per camera and will be in turn soldered onto the previously mentioned midplane connectors. The design and dimensions of the camera mounts can be seen in Figure 67 in Appendix A.

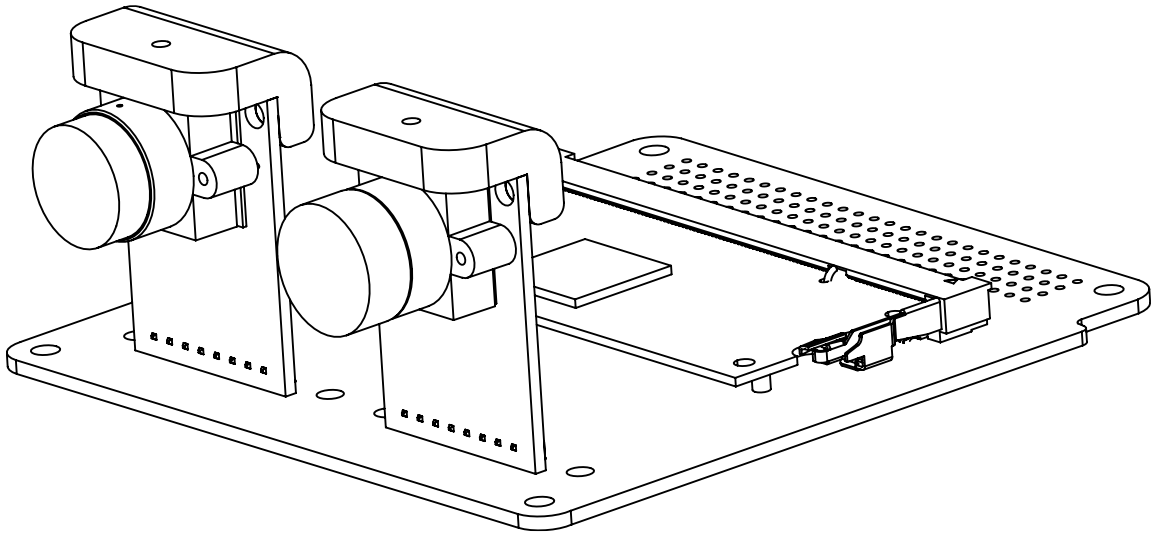


Figure 13: Payload Board Assembly Design

#### 4.4. REACTION WHEEL BOARD (MVC)

##### 4.4.1. MECHANICAL INTERFACE AND SPECIFICATIONS

The optimal size for the reaction wheels, as determined by the Attitude Determination & Control Systems (ADCS) division, was 44mm. However, this wheel size was too large given the PC-104 spec board dimensions. The reaction wheel casing and wheels were modeled to their maximum sizes to fit within the board dimensions at a 23-degree incline from the surface. This resulted in a wheel size of 38mm, which was handed off to the electrical ADCS (electrical) team for further momentum calculations. The RW board was designed to fit the largest possible RW to not interfere with the rest of the satellite structure and satisfy the requirements and constraints provided by the ADCS (electrical) team. The RW model drawing can be seen in Figure 68 in Appendix A.

##### 4.4.2. RW BOARD MATERIAL

For magnetorquer mount materials, there are three viable options for the casing materials, which are Aluminum 6061-T6 or 3D-printed plastics (PLA and PET). Given the complex design of the RW board, it is preferred to use 3D-printing as it decreases manufacturing complexity, as machining would require multiple steps to achieve the same product [35]. Material property comparison is shown in Table 3 below.

Table 3: ADCS component material comparison

Material	Density [kg/m <sup>3</sup> ]	Yield Strength [MPa]
Aluminium 6061-T6 [36]	2700	276
PET Plastic [37]	70 - 1450	47 - 90
PLA Plastic [38]	1000 - 2470	2 - 103

Simulations of launch conditions were imposed on the RW board through FEA, to analyze the structure material behavior. The results of the FEA (shown in Figures 74, 75, 76 in Appendix B) show that PET plastic provides the necessary strength requirements as to not deform and yield under launch conditions. The maximum stress experienced by the RW board is 63 kPa under a 12G load. This stress is much lower than the yield strength of the PET plastic [37] making it a suitable choice.

## **4.5. MAGNETORQUER BOARD (MVC)**

### **4.5.1. MECHANICAL INTERFACE AND SPECIFICATIONS**

As previously stated, this report is solely focusing on the mechanical aspects. The constraints and requirements used for the mechanical models were obtained from the ADCS (electrical) team and the satellites mass and moments of inertia.

Given the constraint that all torquerods and aircores are to be orthogonal to each other, an L-shaped design was developed for the magnetorquer board with the aircore placed underneath the PCB as shown Figure. 69 in Appendix A. This design provides ample space for all circuit board components required by the magnetorquer. Clamping mounts were developed to allow for easy torque rod installation and to minimize weight. These clamp mounts are positioned at the ends of the torque rods. Aircore and mounts are attached to PCB with M2 bolts.

### **4.5.2. CORE MATERIAL**

The two main types of magnetic materials are hard and soft magnetic materials. Where hard magnetic materials possess high retentivity and hysteresis losses. In contrast, soft magnetic materials have low retentivity and hysteresis losses [39]. It is also worth mentioning that soft magnetic materials can easily be magnetized and demagnetized while hard magnetic materials have the opposite characteristics.

The type of material chosen for this magnetorquer design was soft magnetic due to its inherent lower hysteresis loss. Other criteria that were considered were high initial permeability, high maximum permeability, high saturation value, low coercivity, low retentivity, high resistivity, and low density. Table 4 below shows the materials considered and their magnetic properties.

Table 4: Magnetic Material Property Comparison

Property Material	$\mu_i$	$\mu_{max}$	$B_{sat}$ [T]	$H_c$ [A/m]	$B_r$ [T]	$H_{sat}$ [A/m]	Resistivity [ $\Omega \cdot m$ ]	Density [kg/m <sup>3</sup> ]
4% Silicon-Iron	15e-3	17647	1.60	41.38	1.51	127.32	47e-3	7670
45 Permalloy +	4e-3	12732	0.54	9.00	0.28	1000.00	45e-3	8170
Hipernik	4.5e-3	62500	1.47	11.47	1.41	43.77	50e-4	8250
78 Permallaoy	8e-3	48000	0.84	3.98	0.66	79.58	16e-3	8600
4-79 Mo-Permalloy	20e-3	117500	0.77	2.39	0.62	13.53	55e-3	8720
Supermalloy	100e-3	222222	0.73	0.64	0.24	12.73	60e-3	8770

Upon completion of the material comparison, the material chosen for the torque rod cores was 4% Silicon-Iron. The magnetic properties of the ceramic ferrite core sufficed the control requirements and was a light and cost-effective choice.

#### 4.5.3. MOUNT MATERIAL

Two options for the mount manufacturing that were considered were machining and 3D-printing. The materials that would be used for the previously mentioned manufacturing procedures are Aluminium 6061-T6, PLA plastic, or PET plastic. Plastics are the preferred option given their light weight and flexibility in design due to 3D-printing [35].

The important criteria the chosen material was that it must provide ample bending of the mount clamp without the structure yielding. Other criteria considered were, cost of manufacturing and weight. Material properties comparison is shown in Table 4 in the previous section

Upon completion of finite-element-analysis (FEA), the material chosen for the mounts was PET plastic. The results of the FEA (Shown in Figures 77, 78, 79 in Appendix B) depict it provides ample bending without yield. Under a load of 2 N, the mount clamp displaces 3.6 mm and results in a stress of 47 MPa. With yield stress of PET plastic falling between 47 MPa and 90 MPa [37], it was determined that the clamp will bend sufficiently to allow the torquerods to be inserted.

#### 4.6. ADCS COMPUTER BOARD (MM)

The design methodology of the ADCS computer board is quite simple. The PCB has the Nucleo-64 board soldered onto its top side and the NXP board soldered onto its underside. The design of this board can be seen below in Figures 14 and 15.

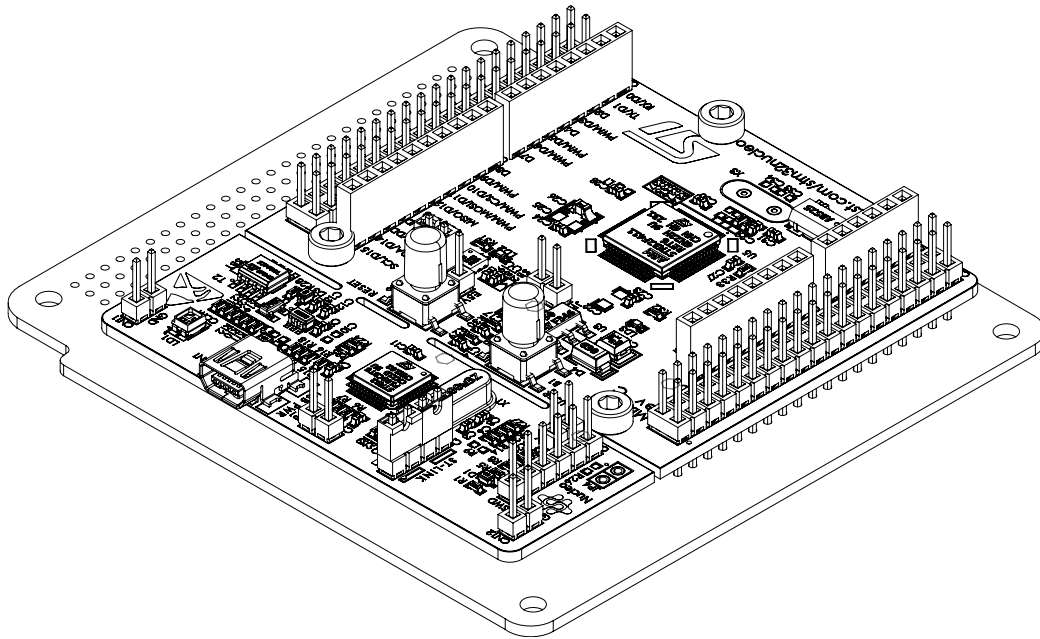


Figure 14: ADCS Computer Board Design (View of Top Side)

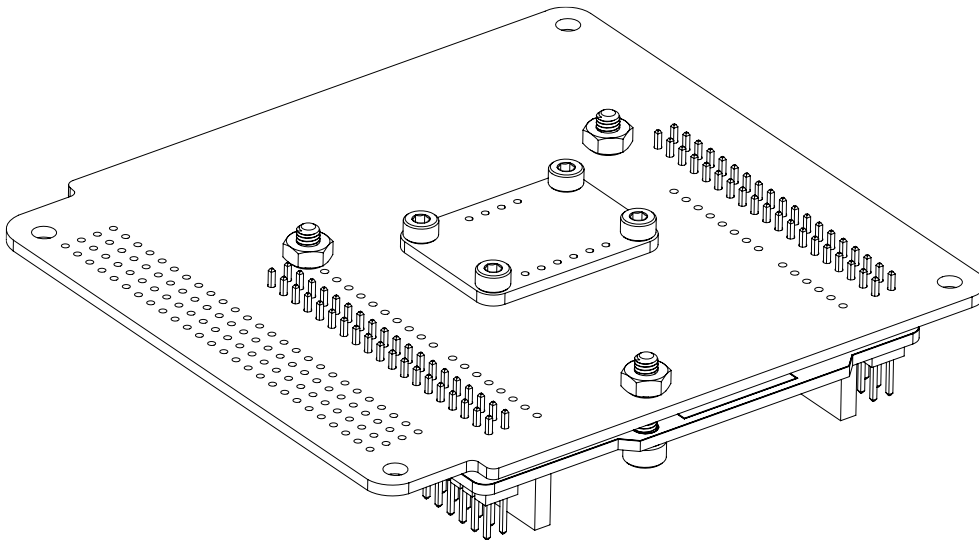


Figure 15: ADCS Computer Board Design (View of Underside)

#### 4.7. DEPLOYMENT SWITCHES (TR)

The requirements provided by the CSDC does not specify the type of electrical switches that can be utilized. As a result, the smallest microswitch that is structurally compatible to the rest of the structure was chosen. In addition, the material properties of the microswitch were analysed and verified to meet the required criteria as shown in Table 5. According to the CSDC guidelines, overall TML  $\leq 1.0\%$  and CVCM  $\leq 0.1\%$  is required [3]. When certain materials are subjected to the vacuum of space, outgassing can occur [40]. Outgassing can have negative effects on the CubeSat's functions.



Table 5: Outgassing mass properties of the microswitch [41]

Material	TML	CVCM
PBT	0.35	0.08
Copper alloy	0.24	0.08
Silver alloy	0.16	0.1
spring steel	0	0

Figure 16 shows how the microswitch is mounted on the side panel using M2 countersink screws and M2 nuts. Countersink screws are chosen to make the assembly of the satellite easier and keeping modularity in mind. Figure 17 shows how the countersink screws sit flush with the base plate's vertical surface. This allows for the two side plates design being implemented to be possible. The flush side of the base plate is then covered by the side panel during the assembly. The deployment switch mechanism can be assembled independently of every other major structural part. Only the components that make up the actual switch mechanism (the microswitch, the retractable spring plunger, the screws, nuts, and the base plate) are required for the assembly and testing of the deployment switches.

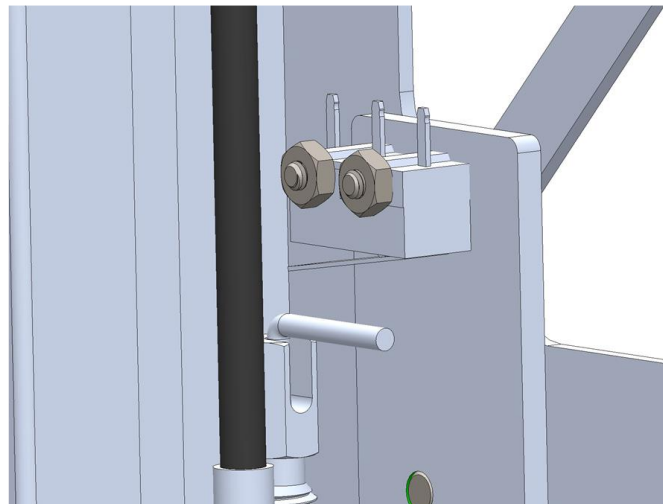


Figure 16: Microswitch Mounting Configuration

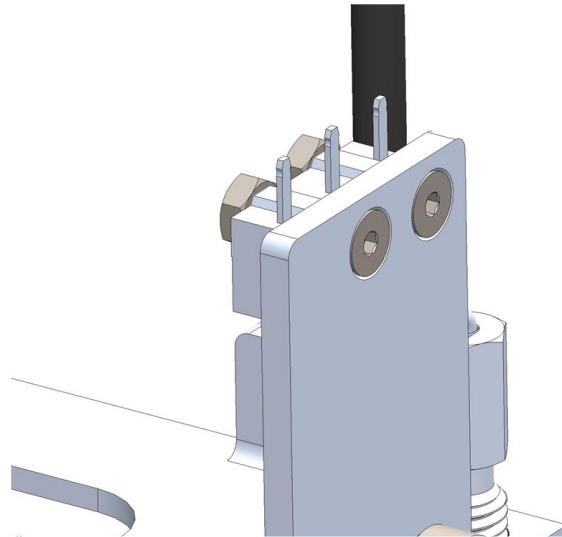


Figure 17: Microswitch Countersink Screws

#### 4.8. SEPARATION SPRINGS (TR)

Just like the retractable spring plungers being used in the deployment switches, the separation spring is installed on the Z face of the standoff rails. The biggest hurdle in incorporating the separation springs in the design was to find a suitable COTS spring plunger that satisfies the force requirements set forth by the CSDC. Due to time constraints and lack of resources, a custom spring plunger was designed based on the constraints. The custom spring plunger is M3 in size, Figure 18 provides a cross-sectional side view of the custom plunger to demonstrate the relevant details. Unfortunately, after being advised by the machinists it was concluded that it would not be feasible to manufacture this custom component. The manufacturing machines available at our disposal simply do not have the low tolerances necessary to machine the parts required for this custom spring plunger assembly.

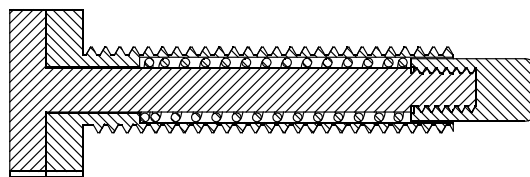


Figure 18: Custom Spring Plunger (Viewed Horizontally)

Ultimately a suitable COTS spring plunger was found that satisfies the design criteria and that is compatible with the rest of the structure. Figure 60 in Appendix A shows the dimensions of the spring plunger that is incorporated in the final design of the CubeSat.

#### 4.9. SPHERICAL AIR BEARING TEST BED (MVC)

From the various investigations conducted into the selection of an air bearing, the A-651 Air Bearing Module by Nelson Air was selected. This air bearing was selected due to its small diameter of 50 mm and large range of motion of  $\pm 45^\circ$  in the roll and pitch axes. From the investigations carried out, many of the COTS air bearing do not have capabilities of  $45^\circ$  rotation the roll and pitch axes. The increased rotational capabilities allow for ADCS controls to be tested in more complex manoeuvres. Additionally, this air bearing was selected as it offers a maximum load capacity of 15 kg, which is much more than what is required for the ADCS components, but will allow for masses to be added to the balancing system without much concern. The bearing parameters are shown in Table 6 below.

Table 6: Specifications of A-651 Air Bearing Module from Nelson Air [42]

Parameter	Value
Sphere Diameter	50 [mm]
Rotation Range	$\pm 45$ [ $^\circ$ ]
Load Capacity	15 [kg]
Base Mass	115 [g]
Sphere Mass	70 [g]
Moment of Inertia	0.02 [ $\text{g}\cdot\text{m}^2$ ]

The air bearing requires a nominal air supply pressure of 6.895 kPa [42] and so the Campbell Hausfeld 1.3 HP portable air compressor was chosen as the COTS component to satisfy this requirement. Additionally, the air bearing requires air to be filtered to 1  $\mu\text{m}$  or better, oil free, and dry ( $-15^\circ\text{C}$  dew point) [42]. This requires an air handling system to filter the air supply, and so the PneumaticPlus SAU2030M-N02G Three Stage air filtering system is chosen as the COTS component to satisfy this requirement. In short, the first stage of this air filtering system is a coalescing filter and so removes oil particles from the air supply. The second stage removes water vapour from the air supply and finally the third stage possess a pressure regulator that filters out small particles.

As previously mentioned, the misalignment of the COG and COR induces a gravitational torque, and so to experience torque-free motion this misalignment must be corrected [16]. Any shift in the COG in the roll and pitch axes cause the air bearing to tilt.

Shifts above the COR makes the air bearing top heavy and making it tip. Finally, if there are shifts below the COR, the air bearing will act like a pendulum.

To solve the issue of misalignment in the COG and COR a 3- axis balancing system is added to the SABTB [16]. This balancing system is comprised of 8 threaded rods, 4 rods are aligned with the roll and pitch axes, and 4 are located on the bottom side of the mounting plate and are aligned with the yaw axis. To lower the COG slotted masses are placed on the yaw axis aligned rods and to adjust the COG in the roll and pitch plane smaller masses such as nuts are threaded onto the roll and pitch axes rods. It is also possible to utilize the roll and pitch plane rods as fine mass adjustments and the yaw rods as a coarse mass adjustment. The mounting plate with the 3-axis balancing system is shown in below in Figure 19.

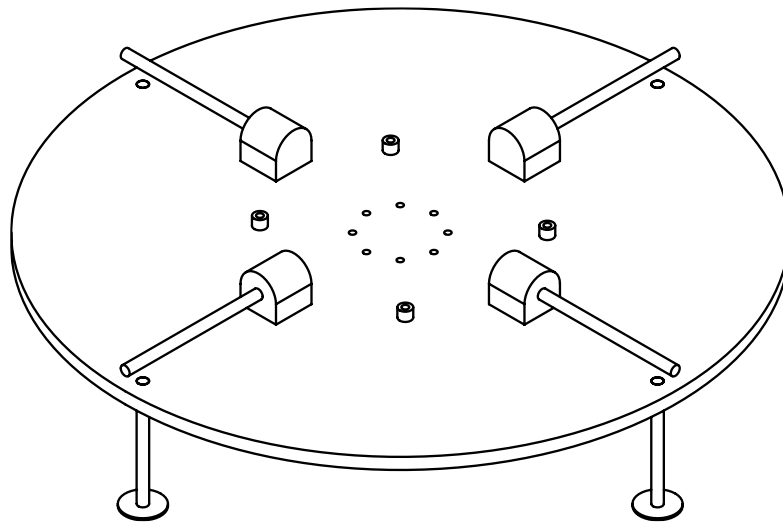


*Figure 19:CAD Model of Mounting Plate with 3-axis Balancing System*

The process of misalignment correction is done by first using an inertial sensor to take measurements of the unloaded air bearing. Then the air bearing is loaded with the ADCS component along with gradual mass increments to the balancing rods until the current measurements made are within a tolerable limit of the unloaded air bearing.

The air bearing will rest on top of a pedestal that is constructed using COTS materials such as schedule-40 PVC piping and plywood boards. This pedestal has a height of 426.34 mm and this is to ensure that the ADCS components are in the center of the Helmholtz cage. Flat end caps will be glued to the ends of the PVC piping and will have holes drilled into them in order to attach the air bearing and plywood base. The mounting plate has a diameter of 308.4 mm and a thickness of 6.35 mm. This diameter was chosen so sufficiently large balancing rods could be fitted to provide a robust balancing adjustment. The mounting plate will be cut from

a plate of plexiglass. Below in Figure 20 is shown the fully assembled SABTB system with the ADCS components mounted

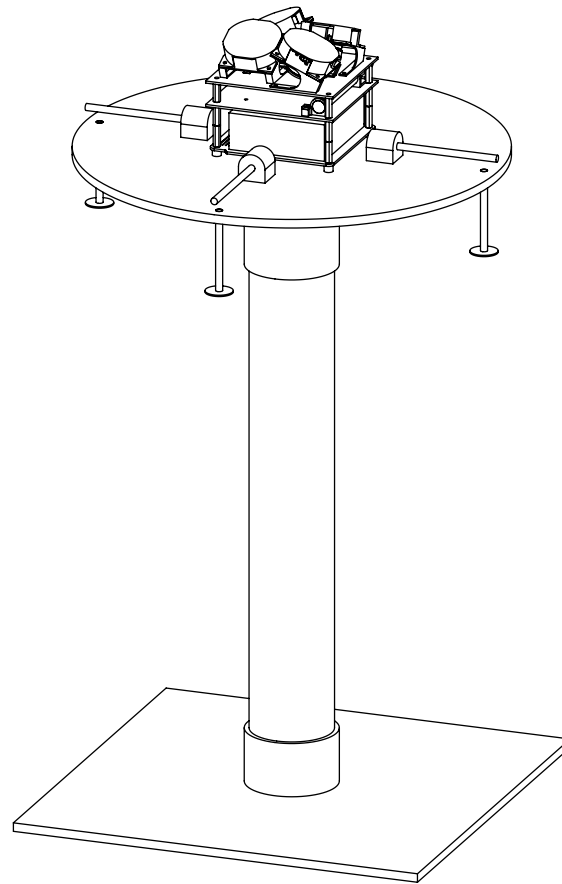


*Figure 20: Assembly of SABTB System with Mounted ADCS Components*

## **4.10. ELECTROMAGNETIC FIELD SIMULATOR (MVC)**

### **4.10.1. MATHEMATICAL MODELLING**

As previously mentioned, the Helmholtz cage is composed of mutually orthogonal pairs of coils in three axes. Prior to describing the physical manifestation of the Helmholtz cage, the requirements laid out in the previous section are quantified with their respective mathematical equations. The parameters of the of the cage, such as coil size, have been determined from the desired homogeneity region.

Determining the equation that describes the magnetic field generated by the interior of the cage was the initial step in the design of the Helmholtz cage. The magnetic field generated at a point by current flowing through a wire can be described using the Biot-Savart law. This law states that an infinitesimal magnetic field by current passing through an infinitesimal length of wire can be expressed with the following equation:

$$d\mathbf{B} = \frac{\mu I}{4\pi} \frac{d\mathbf{l} \times \hat{\mathbf{r}}}{z^2} = \frac{\mu I}{4\pi} \frac{d\mathbf{l} \sin \theta}{z^2} \hat{\mathbf{u}} \quad (1)$$

Square coils were utilized instead of the circular coils as they generate a larger homogenous field compared to circular coils. To simplify the analysis only a single square coil pair is considered and then extending the results of this analysis to the other coil pairs.

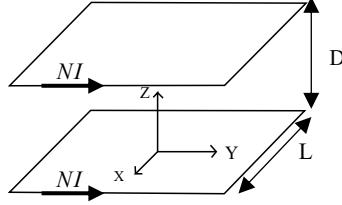


Figure 21: Z axis pair of coils.

The equations governing the magnetic field at along the Z axis of a pair of square coils are shown below. (2) describes the magnetic field of a single side of a square coil as a function of a point along its Z axis. (3) combines the effects of all four sides of a square coil, with an offset of the zero point, and superimposing the coil pair.

$$B_{side}(z) = \frac{\mu NI}{\pi} \frac{L^2}{(4z^2 + L^2)\sqrt{4z^2 + 2L^2}} \quad (2)$$

$$B(z) = 4 \left( B_{side} \left( z + \frac{b}{2} \right) + B_{side} \left( z - \frac{b}{2} \right) \right) \quad (3)$$

It has been noted that as the distance between the coil pair is increased, the magnetic field intensity weakens and varies in shape as seen in Figure 22. To achieve a uniform field at the mid-plane of a square Helmholtz cage a coil spacing distance of 0.5445 times the side length of a coil. Figure 22 depicts the study of a  $\pm 10\%$  tolerance in the value of the coil spacing distance  $b$ .

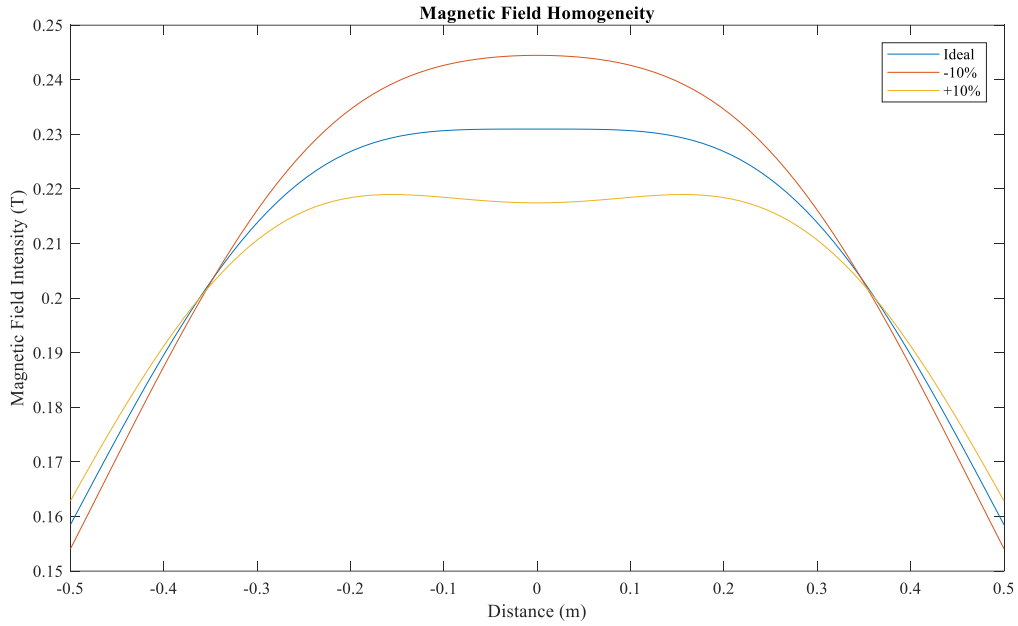


Figure 22: Magnetic Field Homogeneity

A homogenous magnetic field region of  $4.189 \times 10^{-3} m^3$  provides an ample volume for the air bearing and ADCS components to rotate and experience the same magnetic field gradient. This uniform magnetic field volume is achieved with a field uniformity length of 20 cm. To reduce the amount of magnetic wire used and produce a magnetic field intensity of  $50 \mu T$  at minimum, 80 turns and a 10-mA current is used on each coil. The coil parameters are summarized in Table 7 and results are shown in Figure 23. It is important to note that the analysis previously carried out does not consider the effect the magnetic field of each coil pair has on each other. The measured values of magnetic field intensity and homogeneity region will vary from the ones calculated in this report.

Table 7: Coil Parameters Required for Desired Field Homogeneity.

Coil Parameter	Value
Number of turns	80
Current	10 [mA]
Side length	1 [m]
Spacing between coils	0.5445 [m]

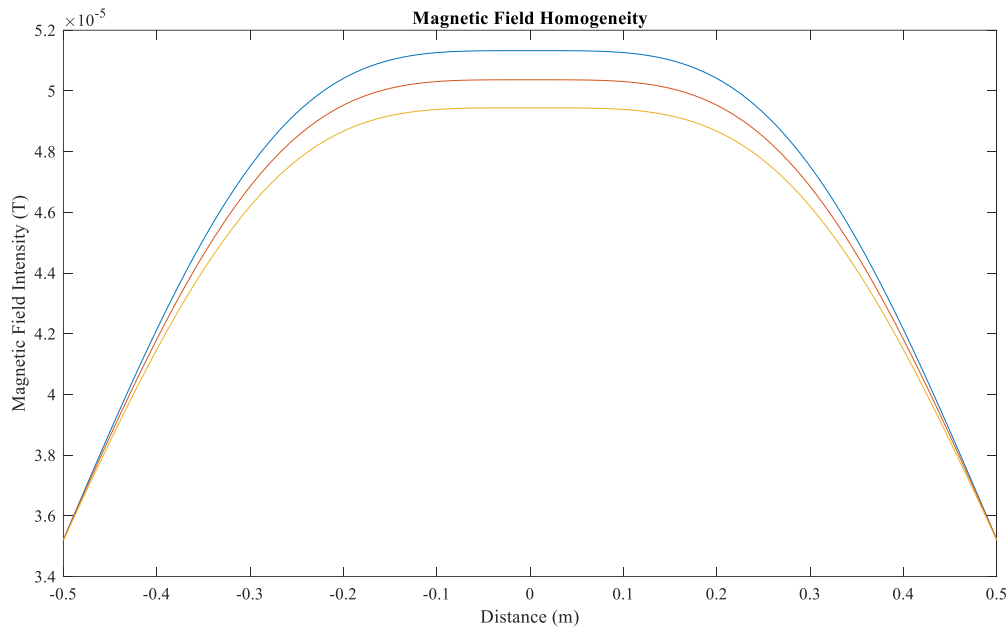


Figure 23: Magnetic Field Intensity for 1 m Side Length 3-axis Helmholtz Cage.

#### 4.10.2. MECHANICAL DESIGN

The structure of the Helmholtz cage will be made from Aluminium 6063 U-channel bars. Aluminium 6063 was chosen for the structure as this material is a paramagnetic material (material with a low magnetic permeability).

The U-channel bars have a cross-section profile with a base of  $\frac{3}{4}$  inch,  $\frac{3}{8}$ -inch side length, and a  $\frac{3}{64}$ -inch thickness. The U-channel bar schematics are shown in Figure 24. The profile of these bars provides a gap in which the magnetic wire loops can be placed.

Each side of the U-channel coil is connect using triangular supports that are fastened using M5 stainless steel screws. The six individual coils are wrapped with the magnetic material in the gap provided by the U-channel bars, and the coil pairs will be attached so their respective magnetic fields add to the same direction.



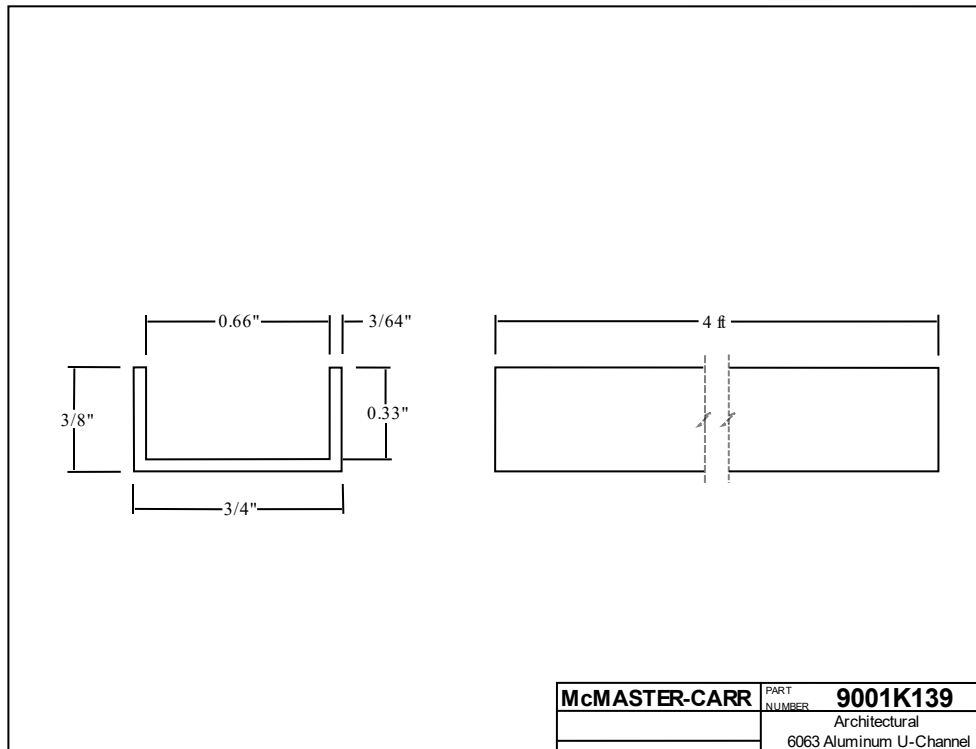
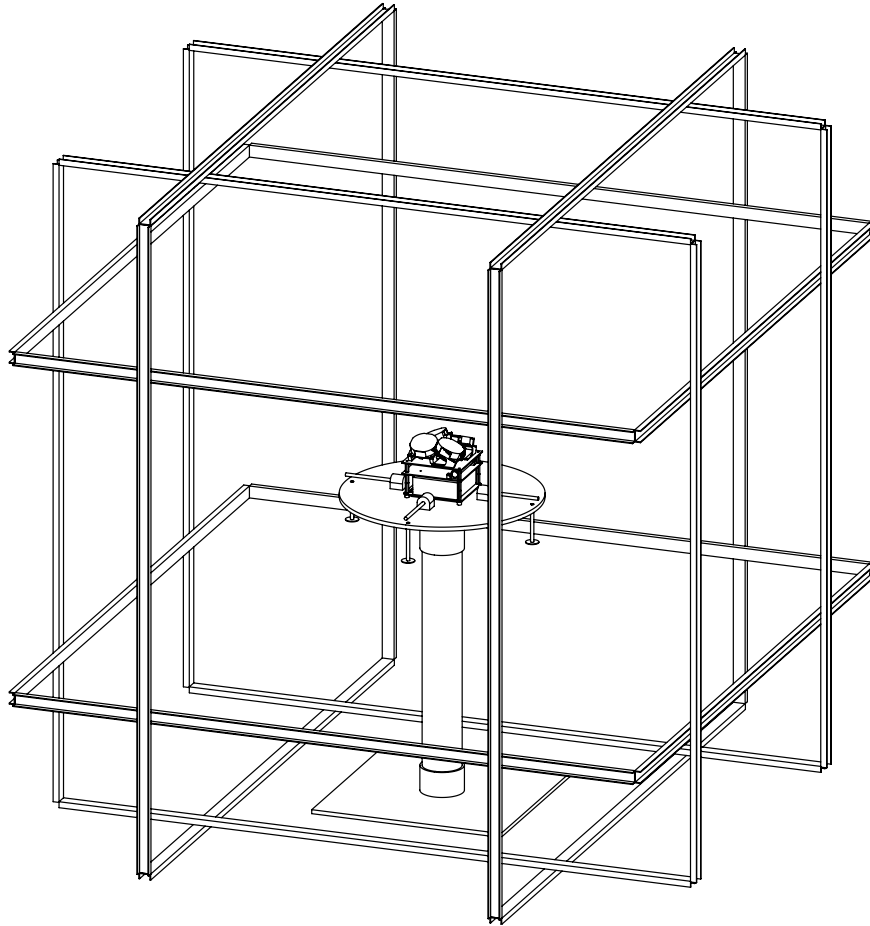


Figure 24: U-Channel Schematic from McMaster-Carr

The coils of the proposed Helmholtz cage are assembled in a nested structure, where one pair of coils placed inside the other. This results in an inner, middle, and outer coil pair. However, this nested structure causes each successive coil pair to be slightly larger than the one it encases. Due to this the distance between each coil pair  $b$  increases but the ratio of  $b = 0.5445L$  is maintained. The dimensions  $b$  are 544.5 mm, 554.9 mm, and 565.4 mm for the inner, middle, and outer coils, respectively. Figure 25 shows the assembled Helmholtz cage.



*Figure 25: CAD Model of Helmholtz Cage Assembly*

The magnetic wire windings used for the Helmholtz cage will be made of AWG14 copper wire. This wire has a nominal current of 5.9 A, diameter of 1.63 mm, and a resistance of 8.28  $\Omega$ /km. As previously stated, to produce the desired magnetic field, each coil requires 80 wire windings. For the given coil dimensions shown in Figure 73 in Appendix A, the resistances for 80 windings are 2.649  $\Omega$ , 2.700  $\Omega$ , and 2.751  $\Omega$  for the inner, middle, and outer coils, respectively.

#### **4.11. STRUCTURAL ASSEMBLY (MM)**

The external structure's vertical threaded rods are very important for the assembly of the satellite. These M3 rods allow the internal components to be stacked in their desired vertical position by having custom spacers between them since each internal board conforms to the PC-104 standard. The custom spacers are made from a hollow metal tube and are simply cut to the desired lengths. This is an inexpensive and practical solution for board separation. This design choice ensures that the internal components remain securely in place without any excess complexity.

The board location has been verified by the COM calculations and the spacers are cut accordingly, where four spacers of the same length are needed for each board separation (one per rod). There are seven internal boards and therefore twenty-eight spacers are required (four rods times seven different lengths). Since the external structure design and assembly has already been discussed, the next step of assembly, the addition of the internal boards, is very simple. The completed assembly can be seen below (with and without solar panels) in Figures 26 and 27.

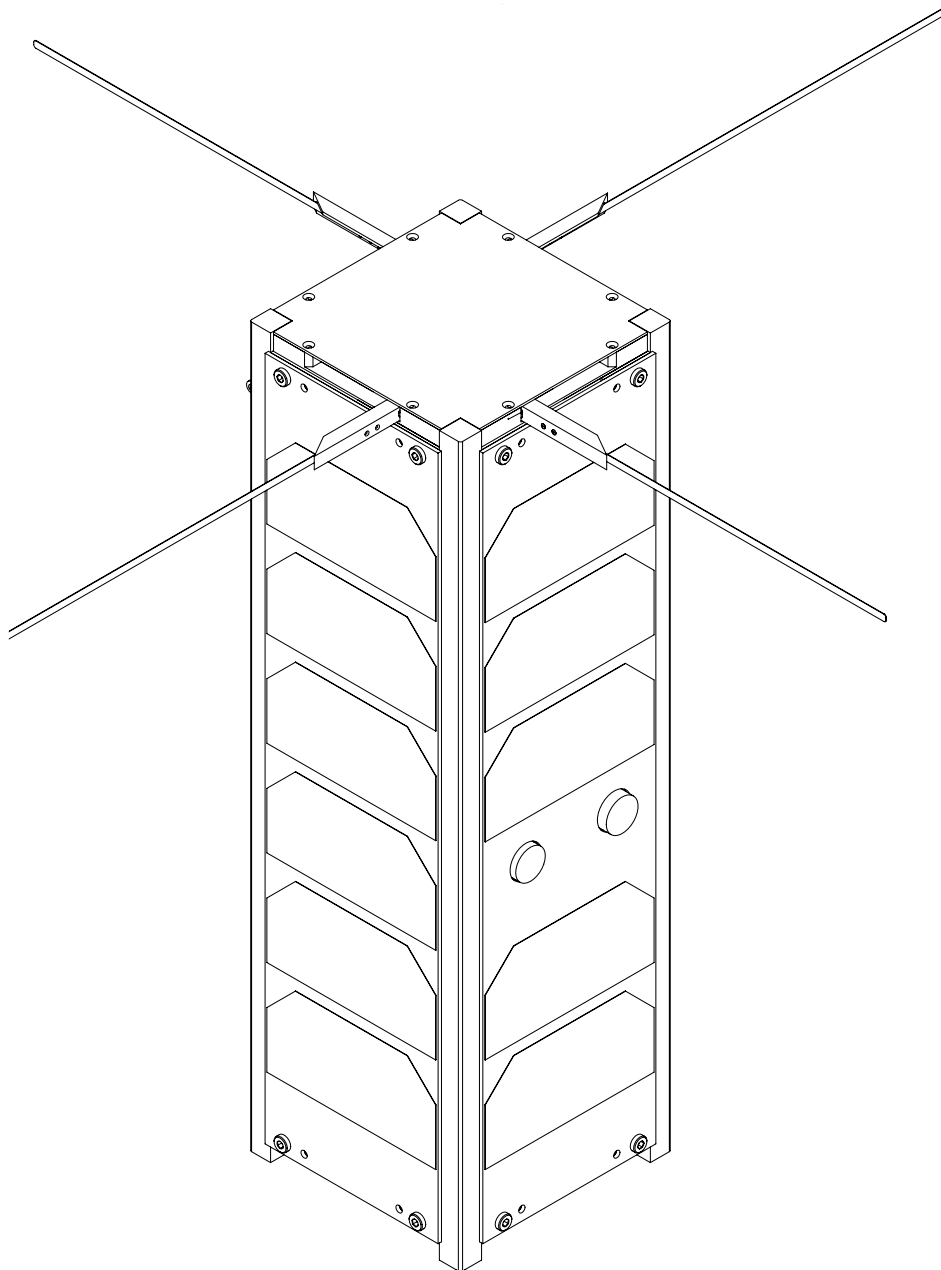


*Figure 26: Complete Satellite Assembly Design with Solar Panels*

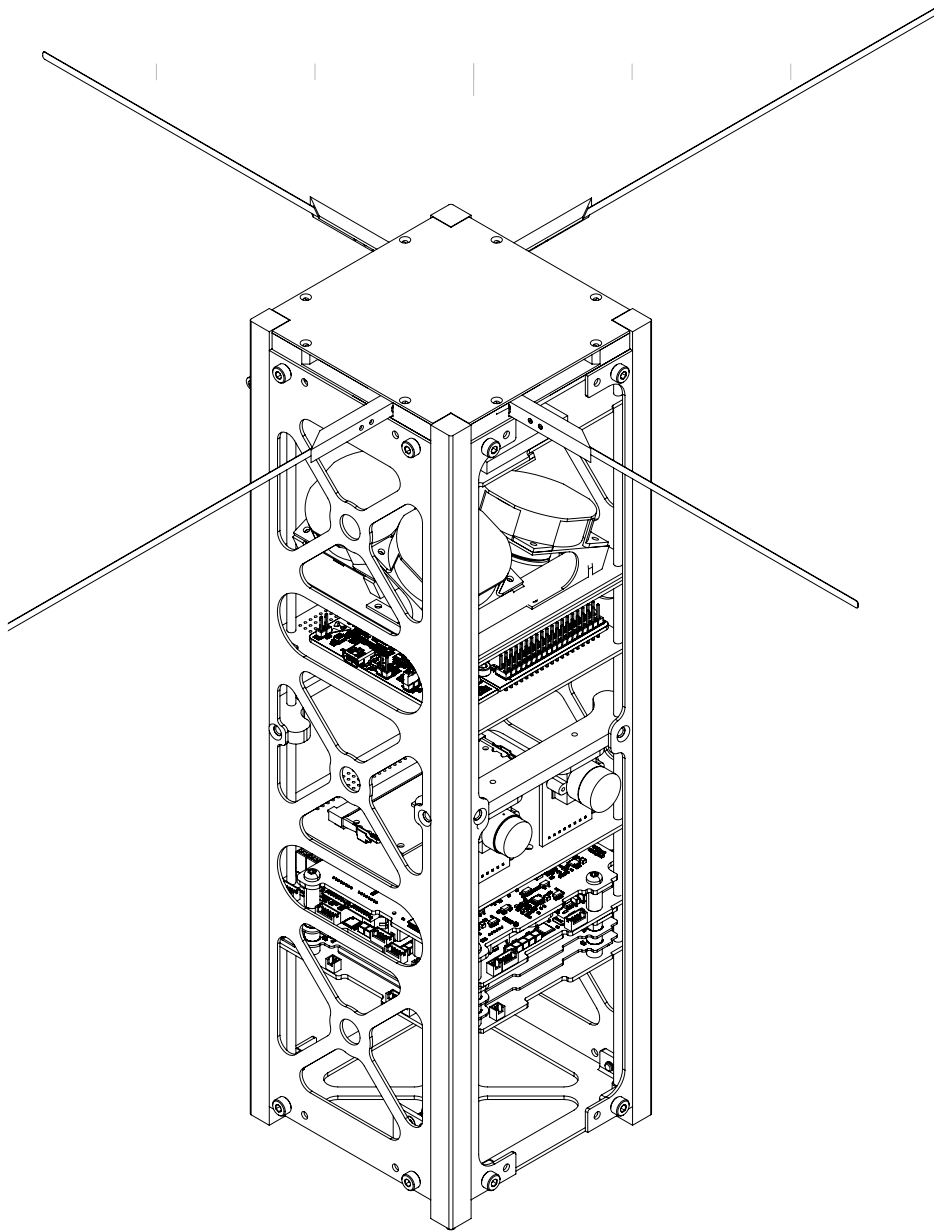


*Figure 27: Complete Satellite Assembly Design without Solar Panels*

## **5. MODEL IMPLEMENTATION**

### **5.1. STRUCTURAL MODEL (MM)**

The virtual model which was made to test and validate the structure of the satellite was created and simulated using SolidWorks. First, internal components such as the OBC, battery module, and ADCS components needed to be simplified. Since the CAD models of COTS components are so visually intensive, they need to be simplified or SolidWorks will not be able to handle simulating them. The simplification was done by modelling the boards with basic shapes such as squares and circles. This will decrease the complexity of the components and

will make it easier for SolidWorks to mesh and simulate, all while preserving the important mass and material properties of the components. The mass properties remain the same by investigating the mass and density of the real components and designing the simplified parts to match exactly. An image of the simplified assembly model can be seen below (without solar panel plates) in Figure 28

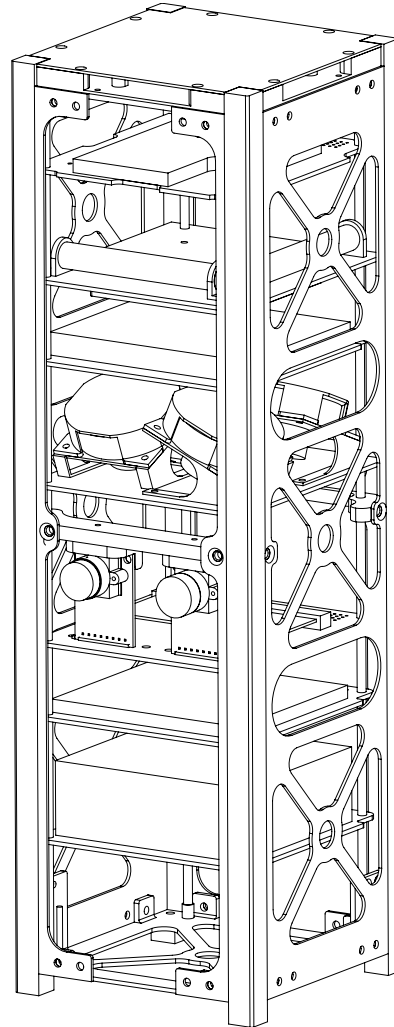


*Figure 28: Simplified Satellite Assembly (without Solar Panel Plates)*

Once the simulation assembly was complete, the next step was to set the appropriate parameters of the model to properly run the required simulations. These parameters include mesh size and refinement, contact sets, virtual bolts, and fixed connections.

The mesh size was automatically generated by SolidWorks' meshing process, and then was modified for certain parts where the loads would be felt more vigorously (i.e. the external structure). The side panels, top plate, and base plate were all set to a mesh size of 0.75 mm. This is half of the smallest dimension of these parts (as they are only 1.5 mm thick) because it

is a meshing standard that there should be at least two meshing elements across the thickness of a part [43].

The defining of contact sets is another very important step in preparing the assembly for simulation. Each area of a component which contacts another component was selected and set to either the “no penetration” setting or the “bonded” setting. “No penetration” is used when there will also be a bolt holding the parts together, whereas “bonded” is used when the parts are welded or connected in some other way. This ensures that when forces on the assembly were simulated, there was no interference between parts which would have given false results.

Physical bolts were not included in the simulation assembly for simplification, as it reduces run time. Instead, virtual bolts were included at all connection points and were assigned a bolt type, length, and pre-tension. These bolt variables were verified by research papers and the bolt analysis study which will be discussed in the next section of the report.

Finally, the fixed connections were applied at the 8 end caps of the satellite. This represents how the satellite will be held in place when it is fitted into the PPOD. Since most of the intense loadings will take place during the launch stage, this was the condition simulated with the simplified structural model.

Once the model parameters were applied successfully, the model was ready for the testing and validation stage, which will be discussed in the next section.

## **5.2. THERMAL MODEL (*TP*)**

The thermal model was created using Siemens NX software, using the structural assembly as a reference. One of the most important methodologies considered for the CAD assembly creation was geometry idealization. The computational time required to complete thermal simulations is heavily dependent on the complexity of the model. The necessity of each geometric aspect of the existing structural model was considered. Components such as fasteners, springs, switches, antennas, electrical connections, etc. were omitted from the model, as these components are not critical to the thermal behavior of the satellite. Additionally, several design features such as fillets, fastener holes, and flanges were removed from the model, as these features add unnecessary complexity to the thermal model. The exclusion and simplification of these components greatly reduced the computation time required for the model to be simulated, which allowed for more tests to be conducted on the model.

Initially, a model was created with only the external components, including the solar panels, aluminum and FR4 side panels, antenna deployment housing, aluminum rods, and top and bottom aluminum plates. These components were all modelled as thin, flat plates to reduce the model's complexity. The simplified model for the external components can be seen in Figure 29.

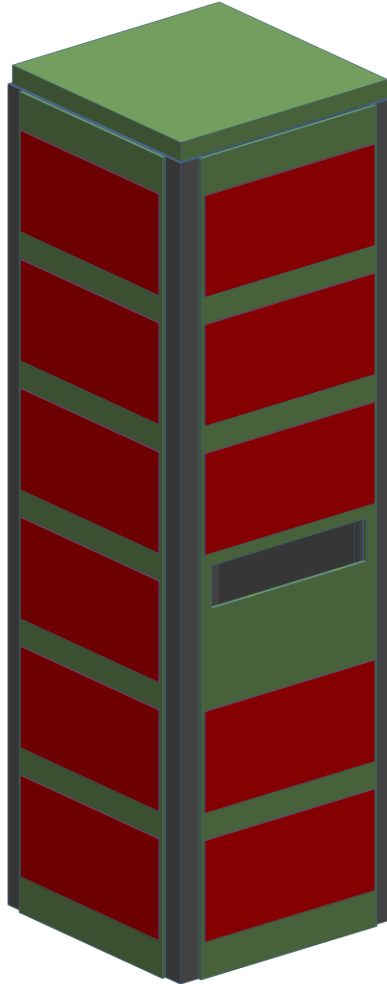


*Figure 29: Simplified Thermal Assembly of External Components*

This external shell model was used for initial simulations since the exclusion of the internal components and internal heat generation allowed the model to exist in its most basic form. This made it easier to understand the simulation behavior and provided the knowledge that any errors observed in later versions of the model would be resulting from a new addition, such as an internal component. The results of this process will be discussed in section 6.2.

The simplified CAD design of the internal components consisted of six PCB boards and two midplane connecting bars. The focus for the internal thermal analysis was on the PCB boards for the payload, MBM2, ADCS, and battery. These four boards hold the computer chips

and battery module, all of which significantly contribute to the radiative heat flux generated within the satellite. These components also require a careful analysis, since they have very tight operating temperature ranges that need to be maintained. Simplified models were created for the RWs and magnetorquers as well. Each PCB was modelled as a flat FR4 board with an internal copper substrate layer. The critical electrical components of interest mounted on top of these PCBs, such as the MBM2 and battery, were modelled as rectangular prisms. The cameras on the payload board were modelled as solid cylinders protruding through the siding of the external shell. The simplified assembly model for the internal components can be seen in Figure 30.

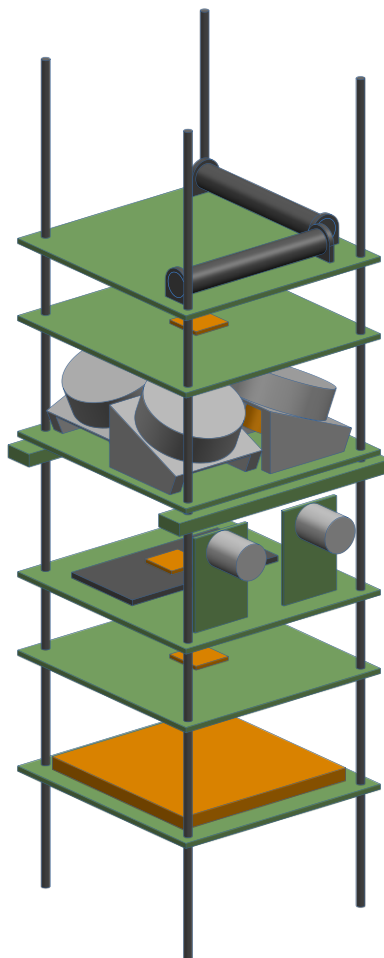


*Figure 30: Simplified Thermal Assembly of Internal Components*

The internal component models were integrated into the external thermal assembly to create the full thermal model of the satellite. This model was created with the proper constraints and distancing, to allow the model to accurately represent the location and connections exhibited within the more complex structural assembly model. A 3-dimensional tetrahedral mesh was created and applied to each CAD component in the assembly. These meshes were



used to create an FEM model. Each mesh was modelled with the corresponding material and optical properties for each component. This allowed for accurate modelling of the amount of heat transfer from each surface, whether that be through methods of radiation or conduction. The thermal FEM assembly is shown below in Figure 31.

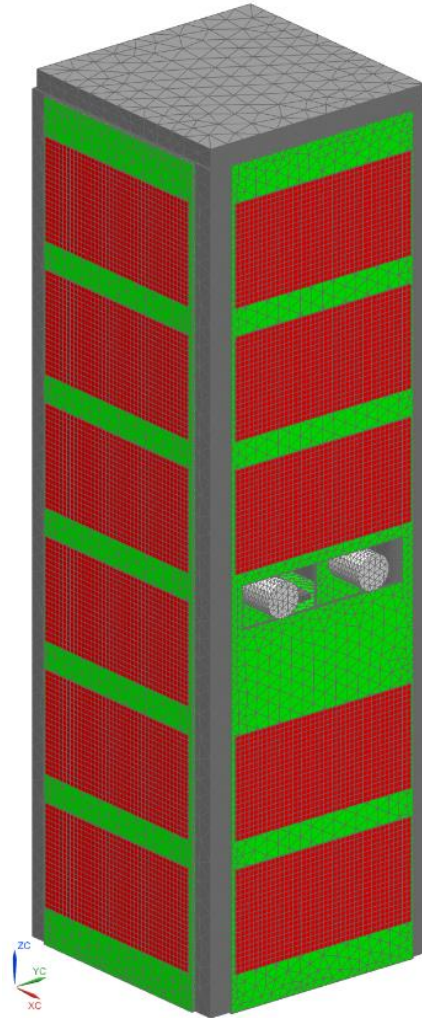


*Figure 31: Thermal FEM Assembly*

## **6. MODEL TESTING/VALIDATION**

### **6.1. STRUCTURAL MODEL**

The structural model which was described in section 7.1 will be used (and slightly modified as required) for the three structural based simulations which are required by the CSDC guidelines. Their descriptions and results can be found in the sections below.

#### **6.1.1. STATIC ANALYSIS (MM)**

The CSDC guidelines state that during the quasi-static acceleration testing, the satellite must endure an acceleration of 12 g in every axis direction [18]. Knowing this physical testing requirement makes it apparent that six simulations must occur, one for each axis direction.

The same meshing, fixed constraints, and virtual bolts as was described in section 5.1 remains valid for the static analysis, but in addition, the gravity loading must be applied in the desired direction (different for each simulation run). A depiction of the assembly fixtures, meshing, and loads can be seen below in Figure 32.

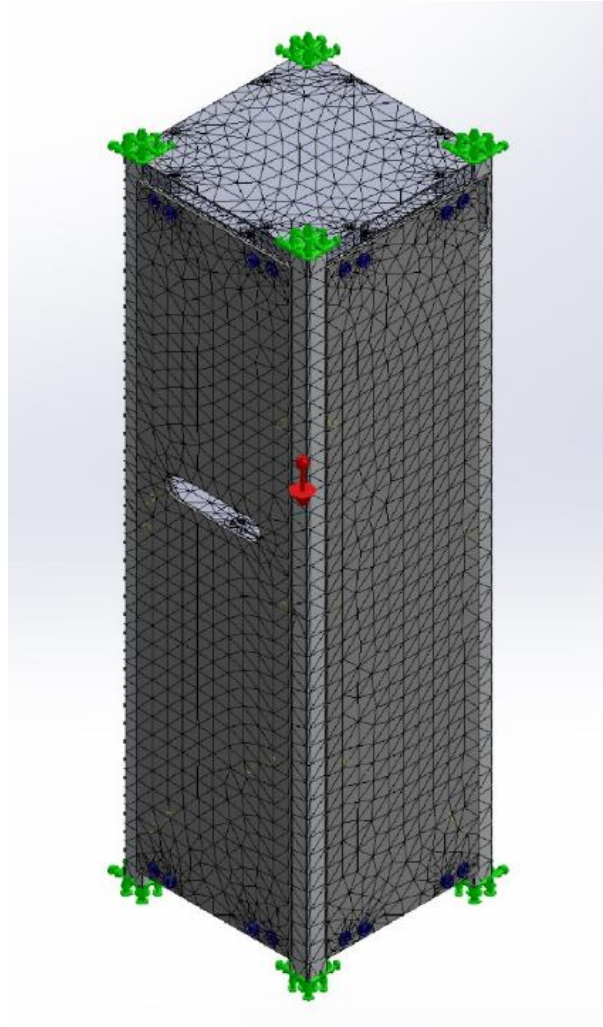


*Figure 32: Simulation Assembly featuring Mesh, Fixtures, and Sample Loading (-Y shown)*

The results of the simulations showed stress, displacement, and strain results which were all well beneath their critical values and limitations set by the CSDC. The maximum stress in each component is well below the required yield strength, even when a FOS of 2 is applied, and the maximum displacement was under 1 mm which was the limit decided upon by the team. Therefore, the results presented below are satisfactory and the current design will be graduated into the AIT phase.

### I. +/- Z STATIC ANALYSIS (VERTICAL LOADING)

The Z axis of the satellite is the vertical axis which runs parallel with the stacking rods and corner rails as defined by the CSDC [1]. The static analyses with the 12 g load applied in both positive and negative Z directions both showed very similar results.

When the stress results of these two simulations were investigated, the main source of stress was found to be in and around the countersink holes designed to connect the midplane connectors to the side panels. This stress concentration area is somewhat expected considering the tight tolerances that putting a countersink hole in that area causes. However, the stresses caused in these locations remained below the yield stress of Aluminium 6061 using a FOS of 2. A close-up image of one of these bolt hole stress points can be seen below in Figure 33.

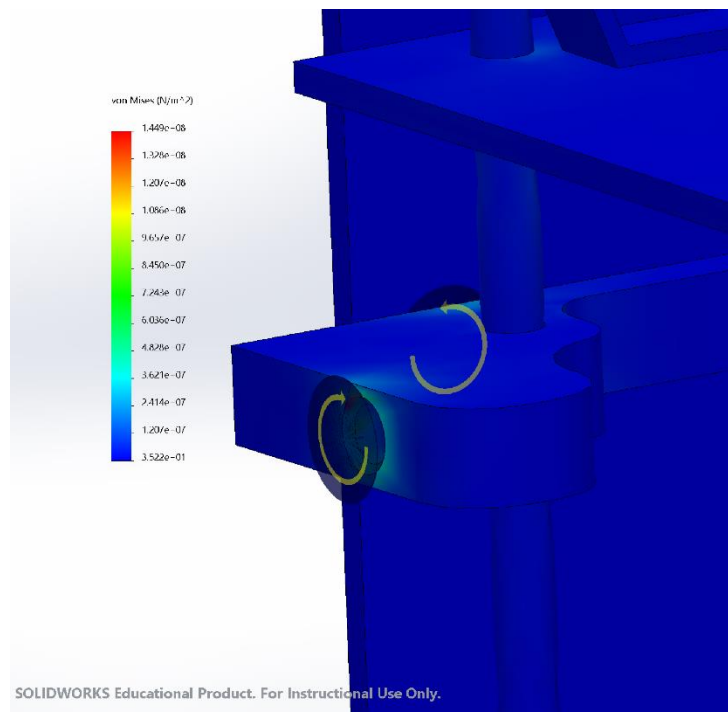


Figure 33: Vertical Loading - Countersink Hole Stress Results Example (-Z shown)

Other notable areas with elevated stresses for the +/- Z loading static analysis include the area around where each board and rod meet. An image of one of these stress points can be seen below in Figure 34. This stress is expected because although the external structure is dissipating much of the loading, some is still transferred to the attached rods and thus the boards. Since these components are not as sturdy as the external structure plates due to the basic nature of forces on thin beams, it is expected that more loads are seen here. Again, these loads are well below the stress limitations set by the FOS and are deemed appropriate.

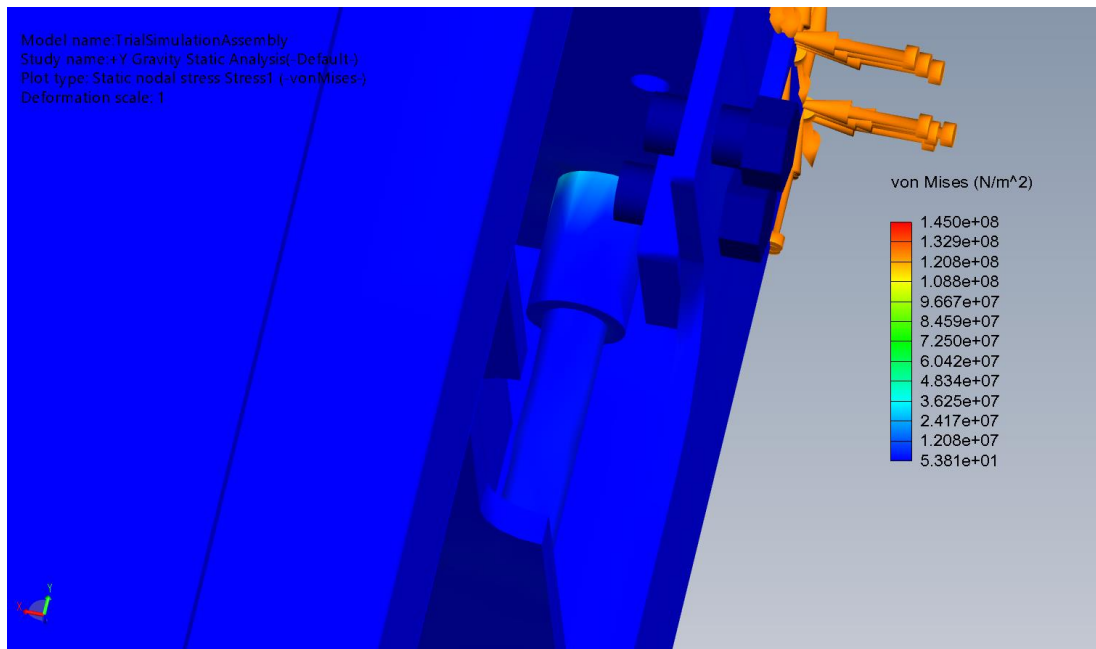
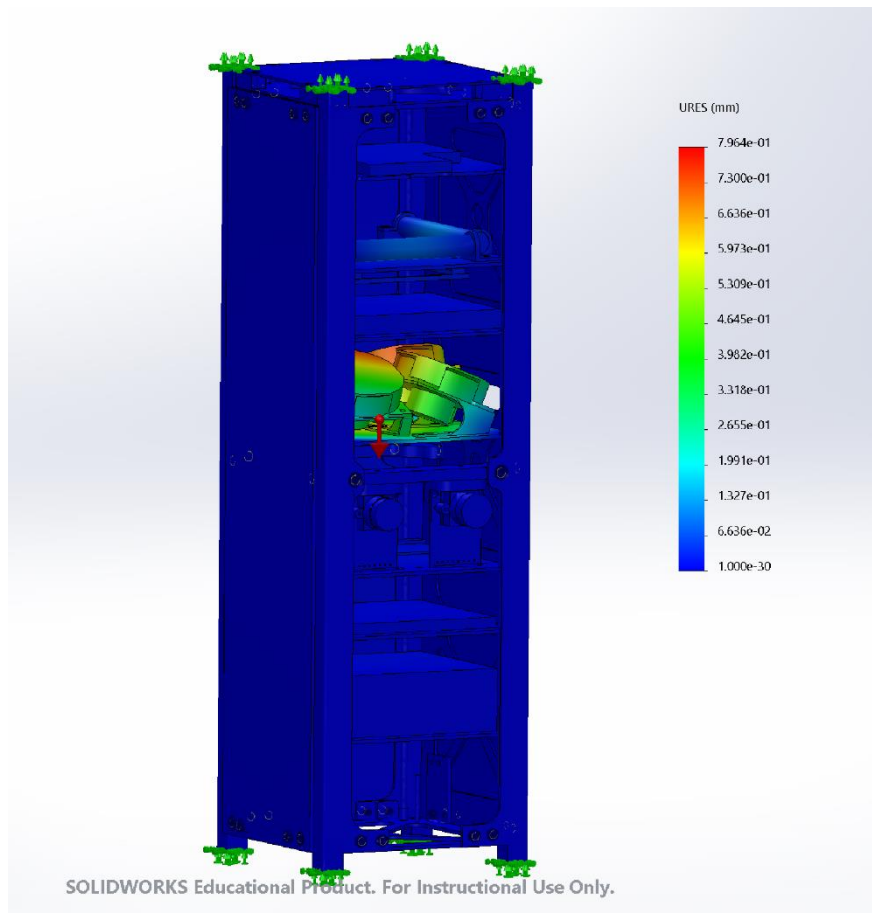


Figure 34: Vertical Loading - Rod/Board Mating Interface Stress Result Example (+Z shown)

The two static analysis performed with loading on each Z axis showed that the most displacement occurred on the RW board. This result could have been predicted simply by looking at the design of the board itself. Since there is space between the RW's and their casing, and between the motors and the PCB, it should be expected that a vertical loading causes deflection in these areas. However, the displacement is less than 1 mm and is negligible based on the team's decided displacement limit. A depiction of the displacement results that were seen for static analysis in both the negative and positive Z axes can be seen below in Figure 35.



*Figure 35: Vertical Loading - Displacement Result Example (-Z shown)*

## **II. +/- X AND +/-Y STATIC ANALYSIS (HORIZONTAL LOADING)**

When loading is applied in the X or Y axis (in either positive or negative direction), the static results are nearly identical. This is because the satellite is nearly symmetric about the Z axis, except for the payload and magnetorquer boards.

The stress results of these 4 simulations are relatively similar to the Z axis simulations, where the most notable stress points occur in the countersink bolt holes and the area where the boards and rods meet. An example of these stress points can be seen below in Figures 36 and 37.

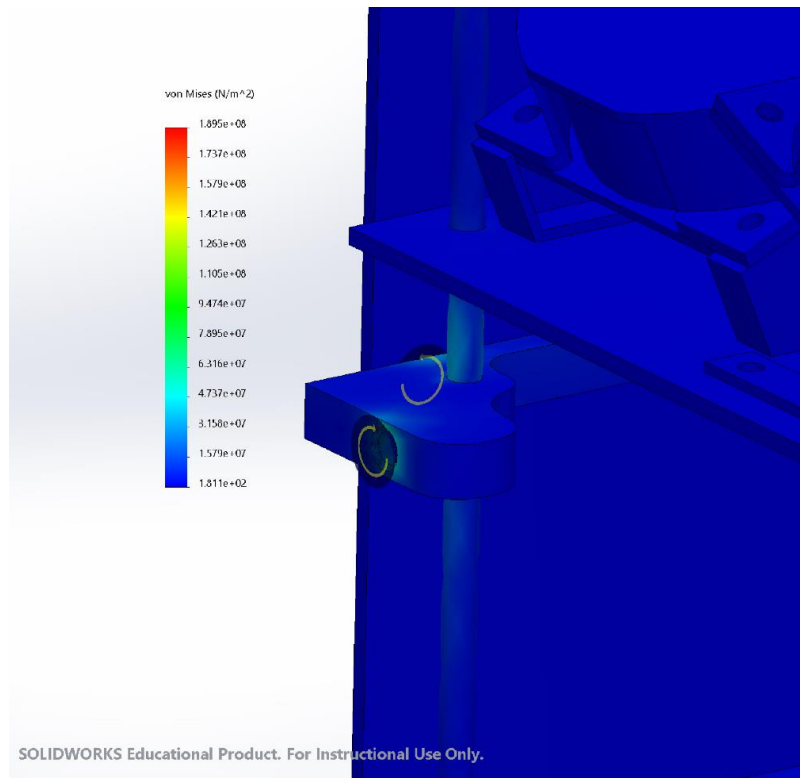


Figure 36: Horizontal Loading – Countersink Hole Stress Result Example (-Y shown)

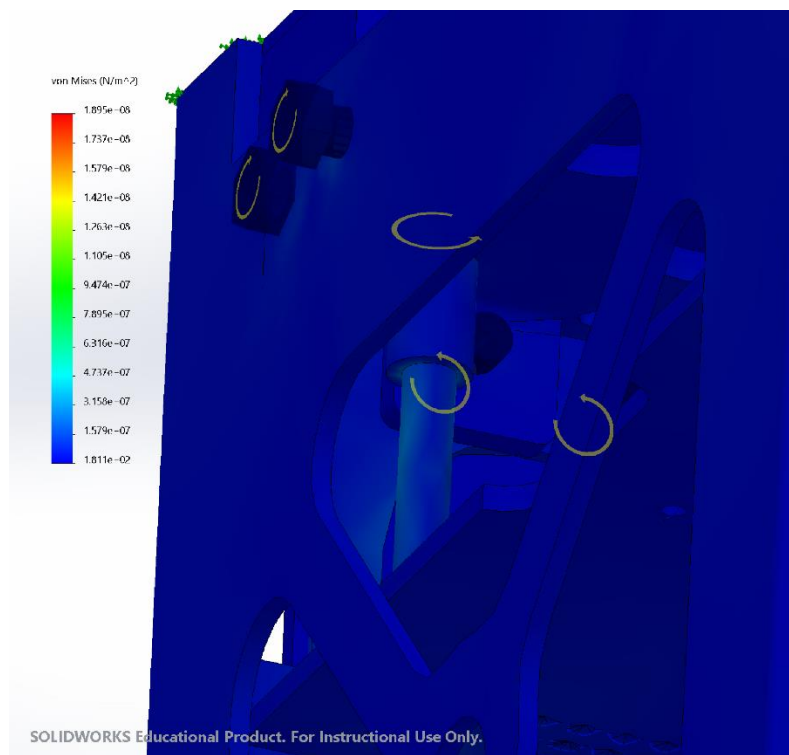


Figure 37: Rod/Board Mating Interface Stresses in Horizontal Loading Static Simulation Results (+X shown)

However, the displacement results of the horizontal loading static simulations are where the major differences occur compared to the vertical loading. Here, quite a large displacement

is seen on the particular solar panel plate which is being “pushed on” by the applied gravitational force. An example of this result can be seen below in Figure 38. Figure 39 shows a similar result on the internal component which can also be seen below.

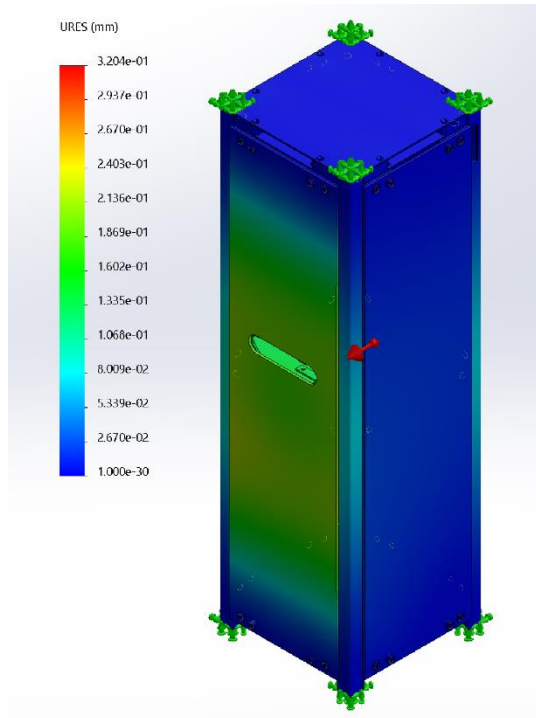


Figure 38: Horizontal Loading - External Displacement Result Example (+Y shown)

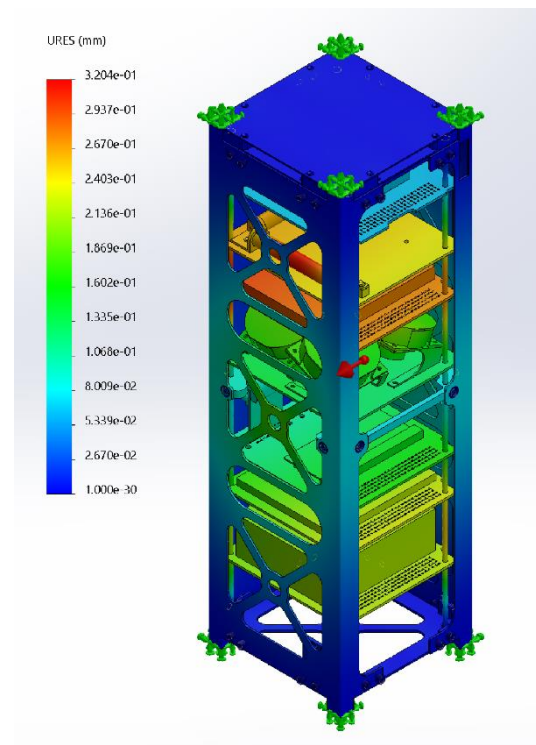


Figure 39: Horizontal Loading - Internal Displacement Result Example (+Y shown)

Once again, this displacement is still less than the decided upon limit of 1 mm and is thus acceptable. To avoid any potential conflict, future teams may choose to add an additional set of bolts to hold the solar panel plates to the side panels closer to the middle of the satellite. This would remove the displacement that has been seen in the current results as it will have more support and will be unable to deflect.

Strain results were also generated by SolidWorks static simulations. Although there are no specific strain requirements listed by the CSDC, it should be noted that the strain results were very low for loading in all directions (in the range of  $10^{-3}$ ). Once again, the horizontal loading axes (X and Y) have experienced very similar results in both loading directions. Since these results are excess information, examples of horizontal and vertical loading strain results have been listed in Figures 80-81 of Appendix B.

### **6.1.2. BOLT ANALYSIS (TR)**

To validate the choice of bolts being used, bolt analysis is conducted using SolidWorks simulation tool. The simplified CAD assembly of the model is used for simulation purposes, every component without a bolt connection is removed from the assembly. Instead of using CAD models of bolts, virtual bolts are added in its place. Figure 40 shows how a virtual bolt looks after being defined. The settings applied for M3 counterbore and countersink screws are the same, Figure 41 shows the detailed settings used. The simulation model is then configured using the no penetration contact setting where applicable.

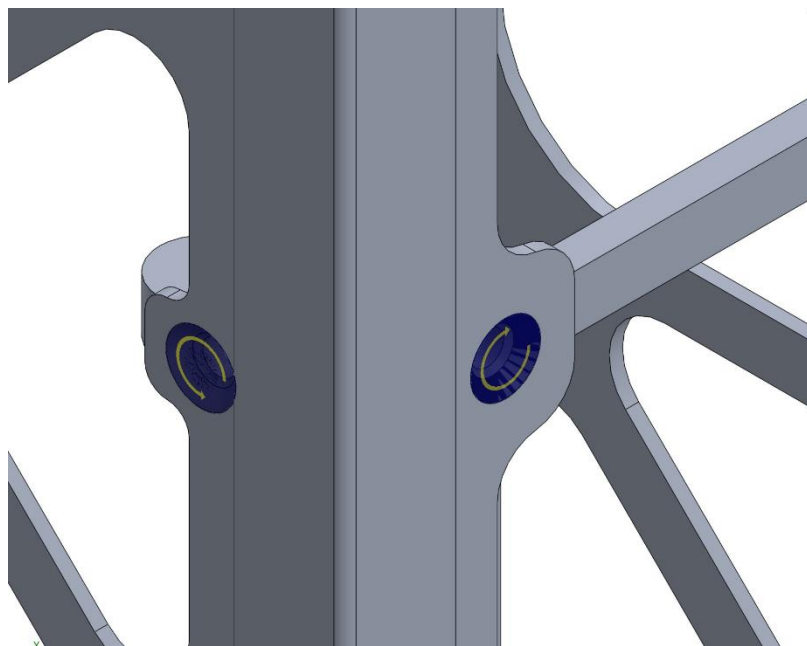


*Figure 40: Virtual Bolt*



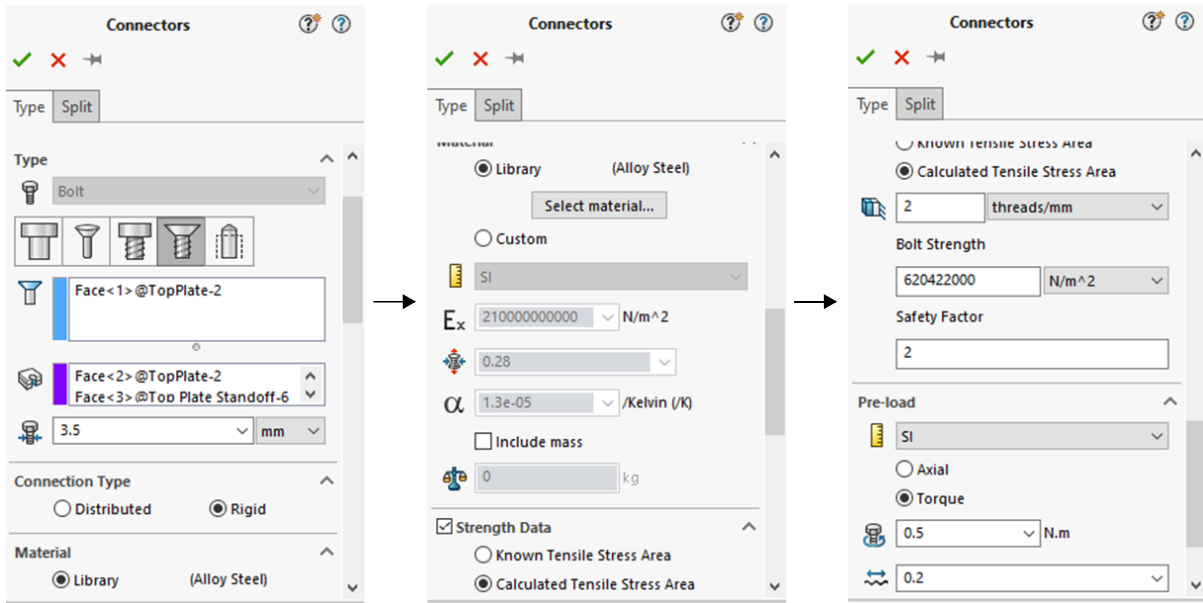


Figure 41: Bolt Connector Settings in SolidWorks

These bolt connections need to withstand a quasi-static acceleration of 12g. To simulate these conditions, static loading needs to be applied in +/- X, +/-Y and +/- Z axes separately, conducting 6 simulations in total. The steps to conduct bolt analysis are similar to the static analysis conducted in section 6.1.1, the simplified assembly model is meshed and run. After the simulation is completed and the results of static analysis are available, the “Define Pin/Bolt Check Plot” function is used which opens a dialog box shown in Figure 42.

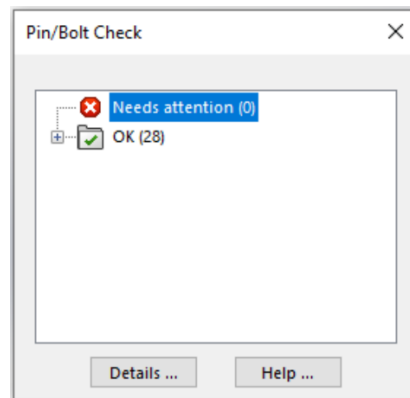
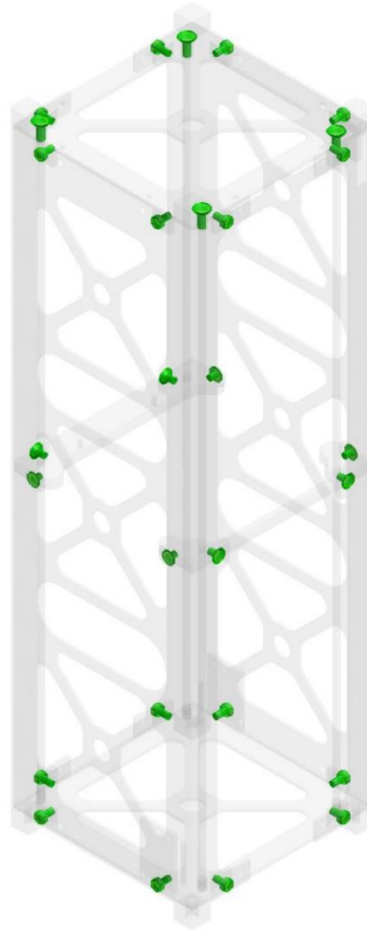


Figure 42: "Define Pin/Bolt Check Plot" Results

This dialog box categorizes the bolts into two sections, the bolt connections that survived the static loading and meet the FOS of 2, and the bolt connections that did not meet the FOS. The results were found to be similar in all 6 simulations, all bolts met the targeted FOS of 2. Figure 43 shows a visual representation of what SolidWorks provided for each simulation result; the green colour indicates that the bolt has passed the requirements.



*Figure 43: Bolt Analysis Results*

### **6.1.3. VIBRATIONAL ANALYSIS (AS)**

During the ascent of the launch vehicle, the satellite will be subject to various random vibrations at different frequencies. This could cause significant damage to onboard electronics and fasteners as the vibrations could loosen electrical connections and fastener integrity. To validate the satellite will nominally operate after the launch sequence, the CSDC has set out two requirements to be met: “the spacecraft shall have a fundamental frequency of at least 90 Hz in each axis” and “the spacecraft shall be designed to withstand the qualification-level launch random vibration environment” [3]. The Launch Random Vibration Qualification Environment is displayed on a Power Spectral Density (PSD) graph in Figure 44. This qualification is defined and applied to the simplified structural model defined in Section 5.1. The created vibration study in SolidWorks is subject to different external loads and parameters compared to the static analysis in Section 6.1. The external loads for the vibrational analysis is expressed by a single global Base Excitation, defining the “Variation with Frequency” component with the datapoints from the PSD graph in Figure 44. To simplify the damping

effect definitions of the satellite, the Rayleigh damping model in SolidWorks is used, defined by the following relationship,

$$\text{Damping Matrix} = \alpha[M] + \beta[K] \quad (4)$$

where  $[M]$  is the mass matrix and  $[K]$  is the stiffness matrix. The damping effect is tuned through the constants  $\alpha$  and  $\beta$ . To simplify the analysis towards a general case solution, the constants for  $\alpha$  and  $\beta$  were selected from a vibrational analysis report on CubeSats [5], resulting in  $\alpha = 3.372e - 4$  and  $\beta = 0.9186$ .

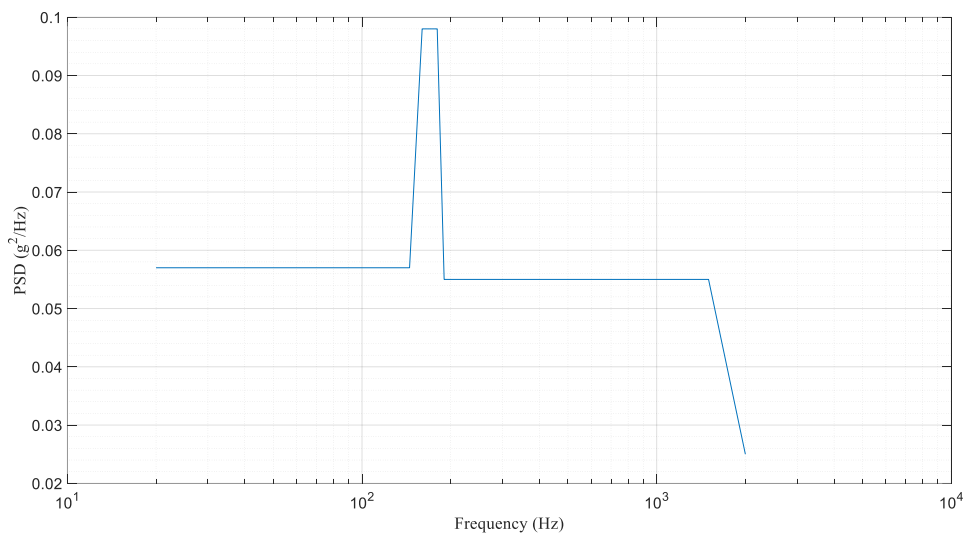


Figure 44: Launch Random Vibration Qualification Environment [3]

With the defined study parameters, the vibration simulation was conducted and resulted in the frequency response displayed in Figure 45.

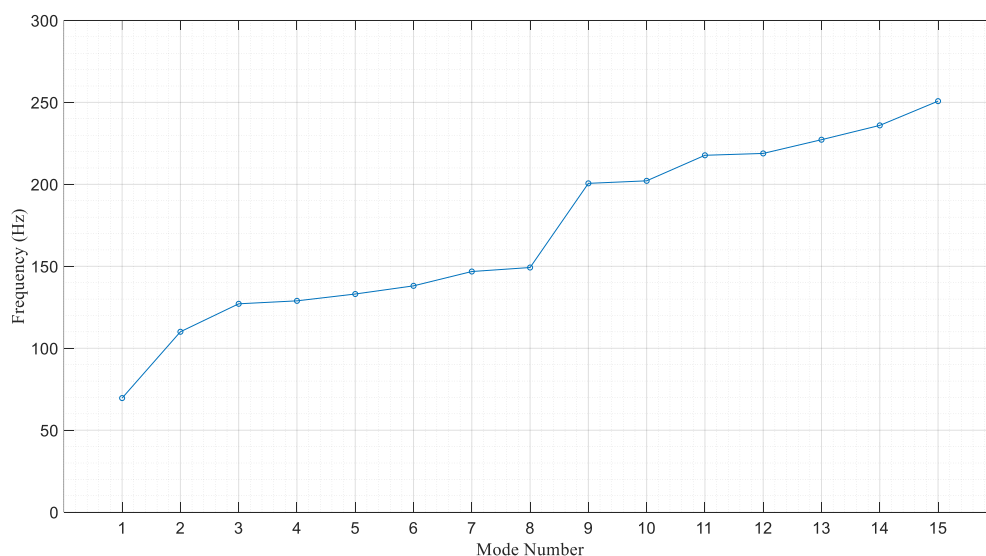


Figure 45: Vibrational Simulation - Modal Response

It is evident from the response that the current satellite model with all the internal components does not satisfy the requirement of the fundamental frequency (Mode Number 1) being at least 90Hz. These results stand in contrast with the vibration analysis results computed for the CDR, which satisfied the 90Hz fundamental frequency requirement however did not account for internal components. Upon further inspection of the stress results from the vibrational analysis, the RW module was identified as the component leading to this decrease in fundamental frequency. The leading hypothesis is that the material stiffness of the selected RW casing (PET) is not high enough to regulate the lower frequency vibrations within the RW module. Further development is required to select new RW casing materials with a higher material stiffness (preferable a 3D printable variant of PET such as Polyether Ether Ketone), that meets the fundamental frequency requirements. Since the reaction wheel casing is 3D printable, the design changes would not be substantial or invasive to current designs, thus the validation of the is left for post-capstone finalization.

#### 6.1.4. CENTRE OF MASS VALIDATION (*TR*)

The overall structure of the CubeSat contains 7 different boards in a stacking configuration, each with its special purpose and unique mass properties. For the design to be efficient, i.e. minimize the use of wires to connect the different boards and components, the placement of the boards is strategically determined. The final placement of the boards and the relative distance between each board is shown in Figure 46.

Based on the requirements provided by the CSDC, the COM must be within 2.0 cm from the geometric centre in the X and Y axes, and within 7.0 cm from the geometric centre in the Z axis [3]. To find the COM, the CAD model of the final CubeSat assembly is used. First, a geometric centre is defined for the structure. Using the COM tool available in SolidWorks, the COM is found using the defined geometric centre as a reference. The results generated are shown below in Table 8, all results are well below the required values. The slight imbalance present in the Z axis is due to the ADS being at the top, the imbalance present in the X axis is due to the position of the two cameras on the payload module.

*Table 8: Centre of Mass Values*

<b>Axis</b>	<b>Actual distance (mm)</b>	<b>Required distance (mm)</b>
<i>x</i>	2.62	< 20
<i>y</i>	0.67	< 20
<i>z</i>	4.82	< 70

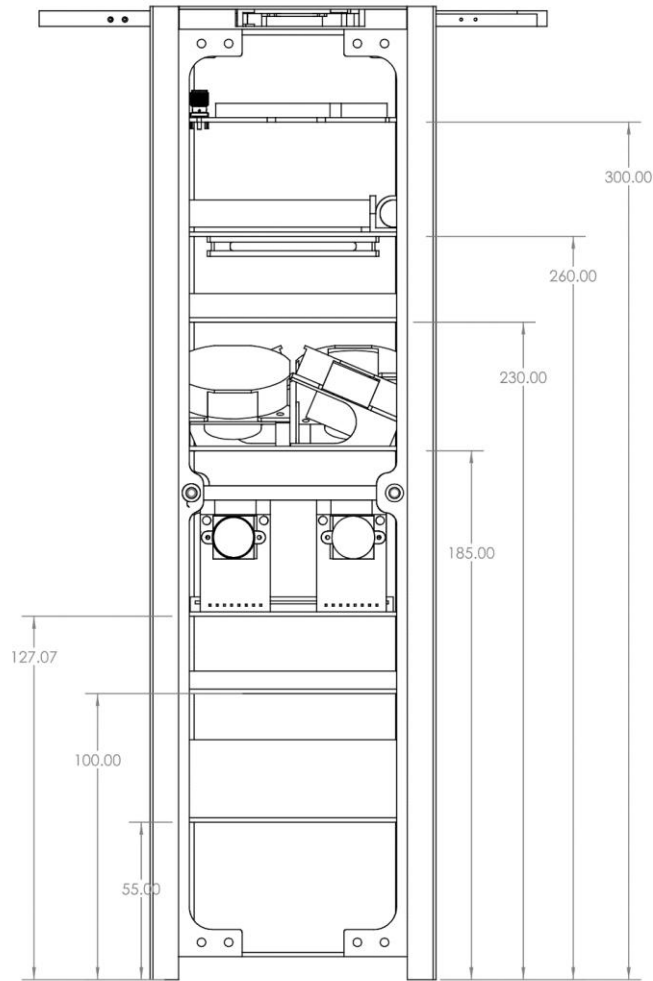


Figure 46: Final Board Placement as Verified by COM Calculations

### 6.1.5. MOMENT OF INERTIA VALIDATION (TR)

There are no formal requirements provided by the CSDC for the MOI. However, the values for MOI are crucial for the operation of the ADCS. The torque needed to be applied by the ADCS will be a function of the MOI values. The results from the MOI analysis conducted using SolidWorks are shown in the tables below.

Table 9: MOI Values at COM

<b>Principal axes of inertia and principal moments of inertia (<math>g \cdot mm^2</math>)</b>			
Taken at the centre of mass			
$I_x$	(0.00, 0.01, 1.00)	$P_x$	2928048.93
$I_y$	(0.32, -0.95, 0.01)	$P_y$	14683124.5
$I_z$	(0.95, 0.32, -0.01)	$P_z$	1477391.92

Table 10: MOI Values at COM Aligned with Output Coordinate System

<b>Moments of inertia (<math>g \cdot mm^2</math>)</b>							
Taken at the centre of mass and aligned with the output coordinate system.							
$L_{xx}$	14764629		$L_{yx}$	-27038.4		$L_{zx}$	41410.1
$L_{xy}$	27038.41		$L_{yy}$	14691731		$L_{zy}$	79147.82
$L_{xz}$	41410.1		$L_{yz}$	79147.82		$L_{zz}$	2928725

Table 11: MOI Values at Output Coordinate System

<b>Moments of inertia (<math>g \cdot mm^2</math>)</b>							
Taken at the output coordinate system.							
$I_{xx}$	14798265.81		$I_{yx}$	-24543.48		$I_{zx}$	59350.14
$I_{xy}$	-24543.48		$I_{yy}$	14734482.46		$I_{zy}$	83736.89
$I_{xz}$	59350.14		$I_{yz}$	83736.89		$I_{zz}$	2939116.66

## 6.2. THERMAL MODEL (TP)

The focus of the thermal analysis was to simulate the temperature distributions experienced by the satellite during the hottest (hot case) and coldest (cold case) orbits throughout the satellite's life. The hot case is modelled during the December solstice, where the Earth is closest to the sun, resulting in the highest intensity radiation from the sun. On the other hand, the cold case is modelled during the June solstice, resulting in the lowest solar flux value [5].

The hottest temperature was hypothesized to occur when the satellite is in direct view of the sun, whereas the coldest temperature would be when the satellite is in the eclipse region (moon blocking the solar flux). The orbital conditions were modelled and applied to the two orbits of interest for this analysis, sun-synchronous and ISS. Although both orbits were simulated, the primary focus was on the ISS orbital scenarios, as this launch type is more common for current-day satellites [44].

Based on a literature review, it was assumed that no convective heat transfer would occur, since space acts as a vacuum with no intermediate moving fluid between components [45]. As a result, the thermal simulations were conducted with radiative and conductive methods of heat transfer only. The main method of heat transfer experienced by the satellite is through radiation. The exterior components of the satellite experience IR from the Earth, Earth albedo, and a constant solar flux from the sun, each of which were modelled for this analysis.

The radiative heat transfer to the environment is extremely significant since an assumption was made that outer space acts as a vacuum with an absolute temperature of 0°K [5].

Due to the large distance between the sun and the Earth, it is assumed that the sun’s rays are parallel once they reach the Earth. Thus, when the satellite is in the eclipse region, it is assumed that no heat flux is received from the sun and there is no penumbra in the shadow cast by the Earth [46]. Additionally, a boundary condition of 20°C was imposed on the satellite during the initial ascent. This created a starting point for the simulated temperatures to begin deviating from.

Conductive heat transfer between all contacting surfaces was also modelled for this application, with the assumption that thermal contact resistance is negligible. This assumption is rationalized by the fact that space has no intermediate fluid between the rough surface contacts of components [47]. No fluid resistance occurs, allowing for perfect contact conductance to be used within the model.

As discussed earlier, some of the internal components such as the computer chips, battery, and RW motors generate heat internally due to energy transformation from the electrical energy to heat energy. Table 12 below displays the electrical power conversion to heat load, as well as the assumed values for the energy conversion efficiency.

*Table 12: Power conversions from electrical to thermal energy*

Component	Electrical Power (W)	Conversion Efficiency	Thermal Load (W)
Payload Chip	3.0	33%	1.0
Battery	1.0	100%	1.0
RW Motor	1.0	50%	0.5
MBM2 Chip	0.38	100%	0.38
ADCS Chip	0.05	100%	0.05

These thermal loads were applied to the top surfaces of the corresponding component model geometry. These heating loads are continuously being applied throughout the orbit since the electrical components of the satellite will be in constant operation. Internal radiation was modelled to occur between all geometrical faces inside the satellite. View factor calculations were computed internally by Siemens NX, ensuring proper radiative communication between each surface.

With all the assumptions and modelling aspects considered above, the satellite was simulated through the hot and cold case conditions in the sun-synchronous and ISS orbits. An example of the maximum and minimum temperature distributions outputted by the simulation results is shown below in Figure 47 and Figure 48.

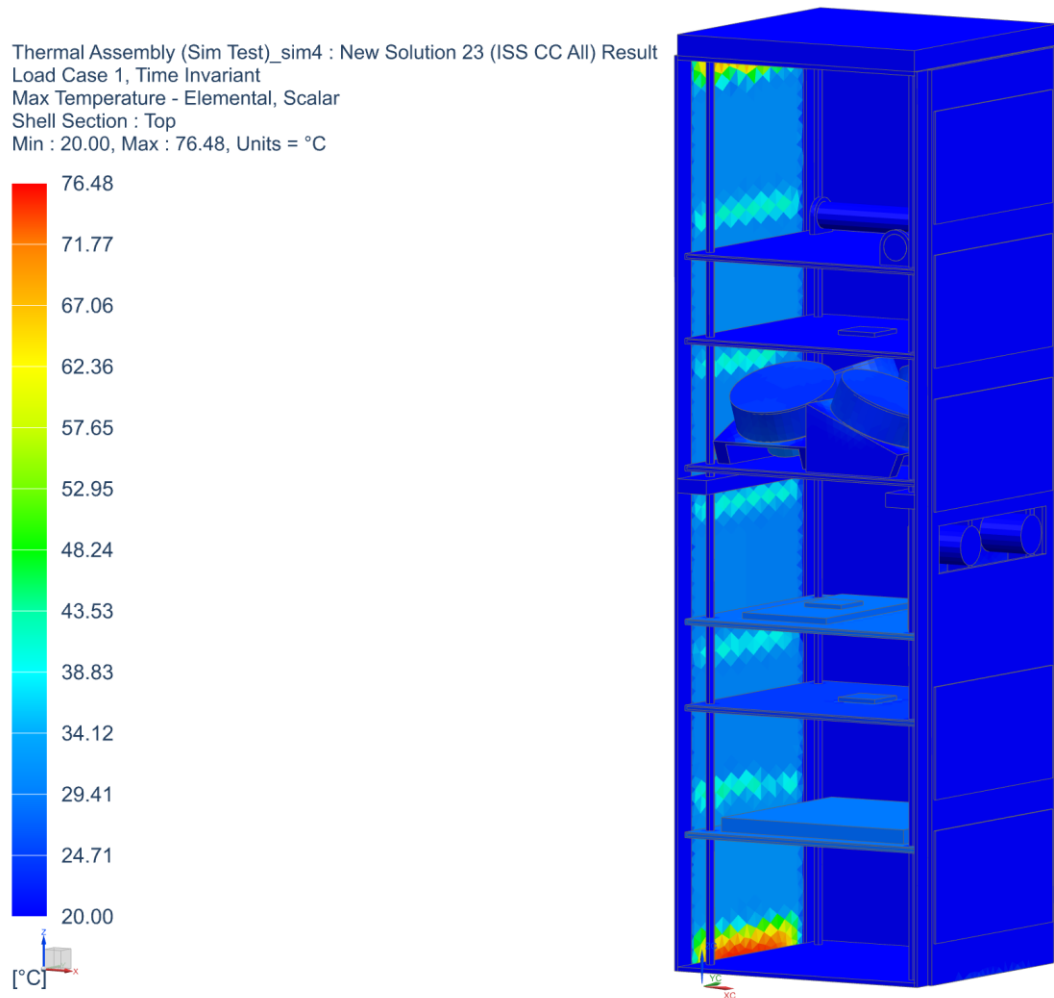
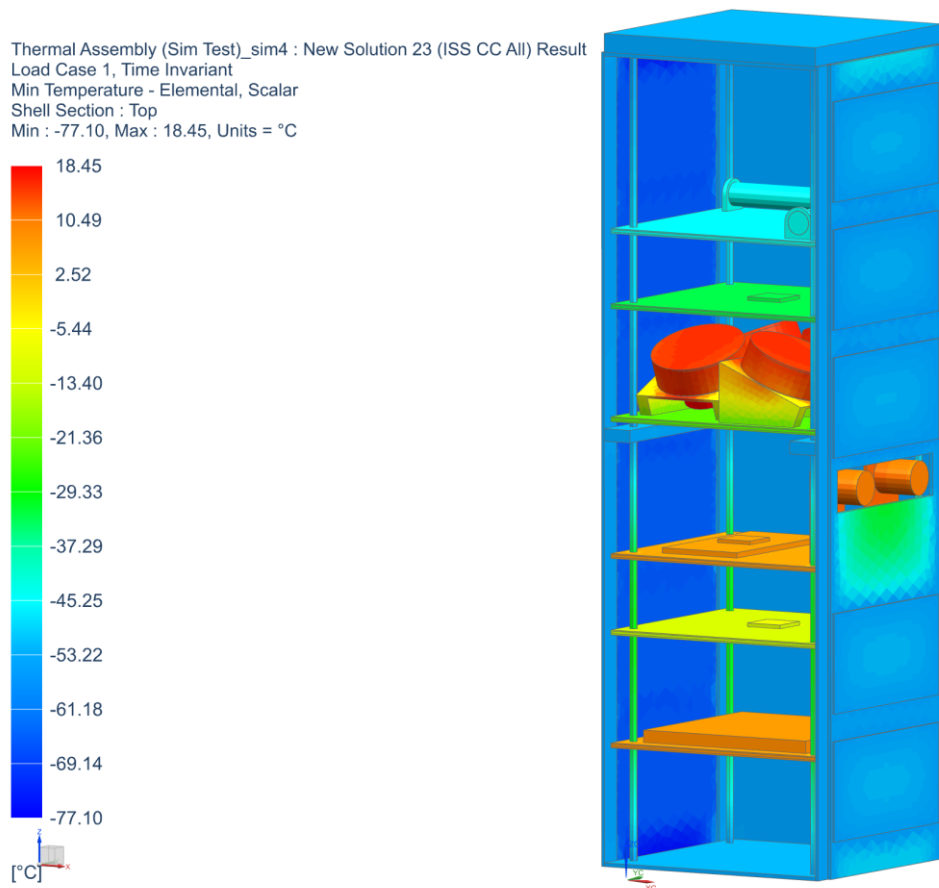


Figure 47: Maximum Temperature Results on Simulation Model for ISS Cold Case





*Figure 48: Minimum Temperature Results on Simulation Model for ISS Cold Case*

The results from each simulation has been summarized by Tables 17 through 20 in Appendix C to show the temperature extremes each component experienced for these conditions. By comparing the simulation results to the required operating temperature ranges in Table 2, the temperature extremes experienced by each component safely lie within the operating ranges. This means that the satellite will remain thermally stable during its operation. Additionally, this means that no changes to the structure of the satellite, such as passive heating elements like insulation, are needed. This is highly preferred for our satellite design, since this allows the design to be lighter, less expensive, and require fewer electrical loads (resulting from active thermal control systems such as heaters or refrigerators).

Various simulations had been conducted on a version of the satellite model that only included the external components. These simulations were conducted to see if changes to the complexity of the model (the addition of internal components and heat generation) would affect the temperatures experienced by the external components (FR4 boards and solar cells). It was found that this was not the case. When comparing the results for the maximum temperature of the solar cells and FR4 boards in Table 17 with the results shown in Figure 49, it can be seen

that they are quite similar. If the temperatures experienced by the external components were the only results of interest, it would be adequate to model the external components alone, with no internal components or internal heat generation.

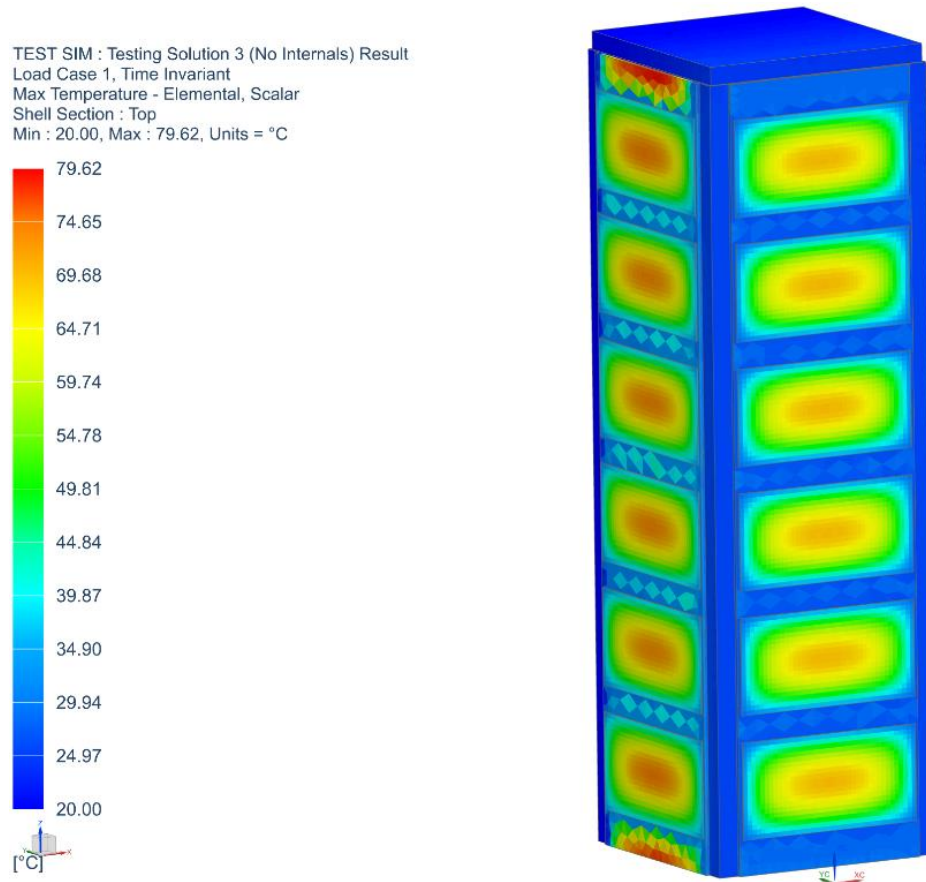


Figure 49: ISS Hot Case - No Internals

## 7. PERFORMANCE METRICS AND SPECIFICATIONS

### 7.1. STRUCTURAL MODEL (NK+MM)

After completing the simulations of the simplified structural model (static analysis, vibrational analysis, and bolt analysis), the performance results were obtained numerically and can be seen below in Table 13. Additionally, a description of the material specifications used to run the simplified structural model is also presented below in Table 14. These performance specifications will be useful for future teams attempting to re-create or improve our results.

Table 13: Von Mises Stresses and Displacements Obtained in Quasi-Static Analysis

Axis	Min Stress (Pa)	Max Stress (Pa)	Min Displacement (mm)	Max Displacement (mm)
X	2.56E+02	1.87E+08	0	1.26E+00
Y	5.38E+02	1.45E+08	0	7.97E-01
Z	1.80E+02	1.85E+08	0	3.20E-01
-X	1.22E+02	1.46E+08	0	1.28E+00
-Y	3.52E+01	1.44E+08	0	7.96E-01
-Z	1.81E+02	1.90E+08	0	1.23E+00

Table 14: Material properties used for Each Component in Static Analysis

Material	How is Material Defined?	Components
Aluminum 6061-T6 [33]	Through SolidWorks material library	<ul style="list-style-type: none"> <li>• Side Panels</li> <li>• Top Plate</li> <li>• Base Plate</li> <li>• Rods</li> <li>• Midplane Connectors</li> <li>• Reaction Wheels</li> <li>• Camera Mounts</li> </ul>
FR4	See Figure MMX for parameters	<ul style="list-style-type: none"> <li>• All PC-104 specification boards</li> <li>• Solar Panels</li> <li>• DDR2 SRAM</li> <li>• Compute Stick</li> </ul>
PET	Through SolidWorks material library	<ul style="list-style-type: none"> <li>• Reaction Wheel Casing</li> <li>• Cameras</li> <li>• Lens Mounts</li> </ul>
Silicon Iron	See Figure MMX for parameters	<ul style="list-style-type: none"> <li>• Torquerods</li> </ul>

Properties Appearance CrossHatch Custom Application Data Favorites Sheet Metal

Material properties  
Materials in the default library can not be edited. You must first copy the material to a custom library to edit it.

Model Type: Linear Elastic Isotropic  Save model type in library

Units: SI - N/m<sup>2</sup> (Pa)

Category: Plastic

Name: FR4

Description: -

Source:

Sustainability: Undefined

Property	Value	Units
Elastic Modulus	2.413165054e+10	N/m <sup>2</sup>
Poisson's Ratio	0.136	N/A
Shear Modulus		N/m <sup>2</sup>
Mass Density	1850	kg/m <sup>3</sup>
Tensile Strength	70000000	N/m <sup>2</sup>
Compressive Strength		N/m <sup>2</sup>
Yield Strength	70000000	N/m <sup>2</sup>
Thermal Expansion Coefficient	7e-05	/K
Thermal Conductivity	0.343	W/(m·K)
Specific Heat	1300	J/(kg·K)
Material Damping Ratio		N/A

Figure 50: FR4 Material Parameters

Properties Appearance CrossHatch Custom Application Data Favorites Sheet Metal

Material properties  
Materials in the default library can not be edited. You must first copy the material to a custom library to edit it.

Model Type: Linear Elastic Isotropic  Save model type in library

Units: SI - N/m<sup>2</sup> (Pa)

Category: Plastic

Name: Silicon Iron

Description: -

Source:

Sustainability: Undefined

Property	Value	Units
Elastic Modulus	124105631.3	N/m <sup>2</sup>
Poisson's Ratio	0.21	N/A
Shear Modulus		N/m <sup>2</sup>
Mass Density	6700	kg/m <sup>3</sup>
Tensile Strength		N/m <sup>2</sup>
Compressive Strength		N/m <sup>2</sup>
Yield Strength	50000000	N/m <sup>2</sup>
Thermal Expansion Coefficient		/K
Thermal Conductivity		W/(m·K)
Specific Heat		J/(kg·K)
Material Damping Ratio		N/A

Figure 51: Silicon Iron Material Parameters

## 7.2. THERMAL MODEL (TP)

Each mesh created in the thermal model was given a set of associated material properties. The physical properties considered are shown below in Table 15. Most of the material properties were gathered through literature reviews, but the properties for copper and polycarbonate were generated internally by the Siemens NX software. Additionally, the optical properties used for radiative heat computations are displayed in Table 16.

*Table 15: Material Properties used for Thermal Modelling*

<b>Component</b>	<b>Density (kg/m<sup>3</sup>)</b>	<b>Specific Heat (J/kg·°C)</b>	<b>Thermal Conductivity (W/m·K)</b>
304 Stainless Steel [48]	8000	500	16.2
Aluminum 6061-T6 [33]	2700	896	167
Copper (NX internal)	8920	387	385
FR4 [49]	1850	290	1200
Iron [50]	7870	440	76.2
PET [51]	1350	1275	0.3
Polycarbonate (NX internal)	1200	1540	0.196
Solar Cell [52]	240	820	4.0

*Table 16: Optical Properties used for Thermal Modelling*

<b>Component</b>	<b>Absorptivity</b>	<b>Emissivity</b>
304 Stainless Steel [53]	0.52	0.15
Aluminum 6061-T6 [54]	0.16	0.06
Copper [55]	0.32	0.02
FR4 [49]	0.80	0.80
Iron [55]	0.85	0.56
PET [56], [57]	0.94	0.92
Polycarbonate [55]	0.17	0.28
Solar Cell [58]	0.88	0.85

## 8. CONCLUSION (*MM*)

Throughout the Capstone Design Course, the team has focused on the design, simulation, testing requirements as outlined by the CSDC [1][3]. The team has successfully completed these mentioned design goals, required research, designs, deliverables, and/or have obtained meaningful results from the Structural and Thermal subsystems of the satellite.

The general objectives for the structural subsystem were to provide sufficient structural support for all internal subsystems, withstanding the launch environment and material stresses, whilst custom designing to adhere to internal component sizing, mounting, and maintaining overall required dimensions. These objectives have been extensively verified by the static and bolt. The vibrational analysis has laid out the initial simulation results for eventual validation of the fundamental frequency requirements. These analyses were completed with various loading conditions and in all axes. Many of the simulations satisfied all requirements, apart from the RWs in the vibrational analysis (as was previously discussed). After a slight modification of materials, the satellite is slated to be complete and ready to enter the AIT phase from a structural standpoint.

The thermal subsystem was required to passively control the satellite's component temperatures to maintain operational temperature ranges through component placement and material selection. These objectives have been achieved throughout the various thermal modelling procedures and simulation techniques applied. Since the temperatures of the components were well below their operational limit at all orbital scenarios, the simulations were indeed successful, and the full thermal subsystem is ready to be developed during the satellite AIT process.

Looking to the future, the current team will be handing off the current designs and simulation results to the next WinSAT team who will begin the AIT process and eventually bring the design into fruition and compete in the CSDC. The satellite, system testing rigs, and WinSAT lab are expected to continue development (pending COVID-19 restrictions) and compete in competitions besides the CSDC to procure a potential launch provider (Canadian CubeSat Project or European Space Agency CubeSat Competition).

## REFERENCES

- [1] “General Rules & Requirements,” *Canadian Satellite Design Challenge Management Society*, 2018. [Online]. Available: <https://drive.google.com/file/d/0B28Xxh64YZ6OUFRQbDAXbkVWaHVWcTR2Z1JEUVRPanBzNIJ/view?usp=sharing>.
- [2] Lawrence Reeves, “ABB Quebec City Host CSDC Workshop and Design Reviews,” 2019. .
- [3] “Design, Interface, and Environmental Testing Requirements,” 2014.
- [4] “How to Build a CubeSat,” 2018.
- [5] J. R. Wertz and W. J. Larson, *Space Mission Analysis and Design*. Microcosm;, 1999.
- [6] “REQUIREMENTS FOR THREADED FASTENING SYSTEMS IN SPACEFLIGHT HARDWARE,” Washington, DC, 2012.
- [7] Students’ Space Association, “CRITICAL DESIGN REVIEW,” Warsaw, 2016.
- [8] J. Friedel and S. McKibbin, “Thermal Analysis of the CubeSat CP3 Satellite,” San Luis Obispo, CA, 2011.
- [9] ITU-R, “Nomenclature of the frequency and wavelength bands used in telecommunications V Series Vocabulary and related subjects,” vol. 8, p. 5, 2015.
- [10] I. Proper, “REACTION WHEEL DESIGN, CONSTRUCTION AND QUALIFICATION TESTING,” *Earth and Space Science*, 2010.
- [11] K. D. Kumar, Godard, N. Abreu, and M. Sinha, “Fault-tolerant attitude control of miniature satellites using reaction wheels,” *Acta Astronaut.*, vol. 151, no. May, pp. 206–216, 2018, doi: 10.1016/j.actaastro.2018.05.004.
- [12] Z. Meili and Q. Hongyu, “Design of three axis magnetorquer for microsattellites,” in *3rd International Conference on Instrumentation and Measurement, Computer, Communication and Control, IMCCC 2013*, 2013, no. 201201010, pp. 579–582, doi: 10.1109/IMCCC.2013.130.
- [13] L. A. Bauer, “Theoretical changes of the magnetic elements with altitude,” *Trans. Am. Geophys. Union*, vol. 6, no. 1, p. 64, Jul. 1925, doi: 10.1029/TR006i001p00064.
- [14] B. D. Cullity and C. D. Graham, *INTRODUCTION TO MAGNETIC MATERIALS Second Edition*. Hoboken, New Jersey : IEEE/Wiley, 2009.
- [15] S. Glitt, “ACS Air Bearing Test-Bed Design,” Naval Postgraduate School, 2010.
- [16] T. USTRZYCKI, “SPHERICAL AIR BEARING TESTBED FOR NANOSATELLITE ATTITUDE CONTROL DEVELOPMENT,” York University, 2011.
- [17] D. S. Batista, F. Granziera, M. C. Tosin, and L. F. De Melo, “Three-Axial Helmholtz Coil Design and Validation for Aerospace Applications,” *IEEE Trans. Aerosp. Electron. Syst.*, vol. 54, no. 1, pp. 392–403, 2018, doi: 10.1109/TAES.2017.2760560.
- [18] “The Canadian Satellite Design Challenge General Rules & Requirements,” no. 3, 2014.

- [19] “AZUR Space Solar Cell Customer Information,” *AZUR Space*. .
- [20] V. Khorenko, C. Baur, G. Siefer, and M. Schachtner, “BOL AND EOL CHARACTERIZATION OF AZUR 3G LILT SOLAR CELLS FOR ESA JUICE MISSION,” in *E3S Web of Conferences 16*, 2016.
- [21] Cortex, *STM32F401xB STM32F401xC (ADCS Datasheet)*. 2019.
- [22] “CubeSat Kit™ Motherboard Module (MBM) 2,” *Pumpkin Inc.*, 2017. .
- [23] G. Coley, *BeagleBone Black System Reference Manual*. 2013.
- [24] “Raspberry Pi Compute Module 3+,” *Raspberry Pi*, 2019. .
- [25] E. Pavlovskis, *User Manual: 3rd Generation CubeSat Battery Family*. 2015.
- [26] Arducam, *2MP SPI Camera User Guide*. 2015.
- [27] Maxon, “EC 20 flat Ø20 mm, brushless, 3 Watt (RW Motor Datasheet).” .
- [28] Fair-Rite\_Products\_Corp, “Ferrite Storage and Operating Conditions.” .
- [29] D. Dai, “Thermal Modeling of Nanosat,” San Jose State, 2012.
- [30] Aluminum-guide, “Aluminum strength at low temperatures.” [Online]. Available: <https://aluminium-guide.com/en/prochnost-alyuminiya-pri-nizkix-temperaturax/>. [Accessed: 01-Feb-2020].
- [31] Matweb, “Aluminum 6061-T6; 6061-T651 Datasheet.” [Online]. Available: [http://www.matweb.com/search/datasheet\\_print.aspx?matguid=1b8c06d0ca7c456694c7777d9e10be5b](http://www.matweb.com/search/datasheet_print.aspx?matguid=1b8c06d0ca7c456694c7777d9e10be5b). [Accessed: 01-Feb-2020].
- [32] Omnexus, “Polyethylene Terephthalate (PET): A Comprehensive Review.” [Online]. Available: <https://omnexus.specialchem.com/selection-guide/polyethylene-terephthalate-pet-plastic>. [Accessed: 01-Feb-2020].
- [33] “Aluminum 6061-T6; 6061-T651,” *Aerospace Specification Metals Inc.* [Online]. Available: <http://asm.matweb.com/search/SpecificMaterial.asp?bassnum=MA6061T6>. [Accessed: 01-Feb-2020].
- [34] A. Alanazi and J. Straub, “Statistical Analysis of CubeSat Mission Failure,” in *32nd Annual AIAA/USU Conference on Small Satellites*, 2018, pp. 1–8.
- [35] A. P. Zwicker, J. Bloom, R. Albertson, and S. Gershman, “The suitability of 3D printed plastic parts for laboratory use,” *Am. J. Phys.*, vol. 83, no. 3, pp. 281–285, 2015, doi: 10.1119/1.4900746.
- [36] M. S. Dargusch and S. M. Keay, *Light Metals Technology 2009*. Stafa-Zurich, Switzerland: Trans Tech Publications Ltd, 2009.
- [37] F. Dominici, F. Sarasini, F. Luzi, L. Torre, and D. Puglia, “Thermomechanical and morphological properties of poly(ethylene terephthalate)/anhydrous calcium terephthalate nanocomposites,” *Polymers (Basel)*, vol. 12, no. 2, 2020, doi: 10.3390/polym12020276.
- [38] S. T. Lee, A. R. Rahmat, and W. A. W. . Rahman, *Poly(lactic Acid) - PLA Biopolymer Technology and Applications*. Waltham, MA, USA: Elsevier Inc., 2012.



- [39] D. Schuller, D. Hohns, R. Loeffler, T. Bernthaler, D. Goll, and G. Schneider, "Analysis of soft magnetic materials by electron backscatter diffraction as a powerful tool," *AIP Adv.*, vol. 8, no. 4, 2018, doi: 10.1063/1.4994200.
- [40] "Outgassing Test Facility Brings New Materials into Space Industry," *NASA Spinoff*. .
- [41] "Outgassing Data for Selecting Spacecraft Materials Online," *National Aeronautics and Space Administration*, 2018. .
- [42] "A-65x PIglide HB: Hemispherical Air Bearing Module." [Online]. Available: <https://www.pi-usa.us/en/products/air-bearings-ultra-high-precision-stages/a-65x-piglide-hb-hemispherical-air-bearing-900712/#specification>. [Accessed: 03-Aug-2020].
- [43] K.-H. Chang, "Design Theory and Methods Using CAD/CAE."
- [44] H. Riebeek, "Catalog of Earth Satellite Orbits," *NASA Earth Observatory*, 2009. [Online]. Available: <https://earthobservatory.nasa.gov/features/OrbitsCatalog#:~:text=Most scientific satellites%2C including NASA's,have a low Earth orbit.&text=The height of the orbit,satellite moves around the Earth.> [Accessed: 27-Mar-2020].
- [45] NASA, "Staying Cool on the ISS," 2001. [Online]. Available: [https://science.nasa.gov/science-news/science-at-nasa/2001/ast21mar\\_1#:~:text=%22In space there is no,invisible to the human eye.](https://science.nasa.gov/science-news/science-at-nasa/2001/ast21mar_1#:~:text=%22In space there is no,invisible to the human eye.) [Accessed: 27-Mar-2020].
- [46] NASA, "Diagram of Umbra and Penumbra," 2014. [Online]. Available: <https://www.nasa.gov/audience/forstudents/k-4/stories/umbra-and-penumbra>. [Accessed: 27-Mar-2020].
- [47] NASA, "Staying Cool on the ISS," 2001. .
- [48] "AISI Type 304 Stainless Steel," *Aerospace Specification Metals Inc.* [Online]. Available: <http://asm.matweb.com/search/SpecificMaterial.asp?bassnum=mq304a>. [Accessed: 01-Feb-2020].
- [49] J. Yoo, T. Kim, H. Jin, J. Seon, and D. Glaser, "A Thermal and Mechanical Analysis of Trio Cinema Cubsat Mission." [Online]. Available: [http://mstl.atl.calpoly.edu/~workshop/archive/2011/Spring/Posters/poster\\_jaegun\\_trio\\_cinema.pdf](http://mstl.atl.calpoly.edu/~workshop/archive/2011/Spring/Posters/poster_jaegun_trio_cinema.pdf). [Accessed: 01-Feb-2020].
- [50] "Iron Datasheet," *MatWeb*. [Online]. Available: <http://www.matweb.com/search/datasheet.aspx?matguid=654ca9c358264b5392d43315d8535b7d&ckck=1>. [Accessed: 01-Feb-2020].
- [51] "Polyethylene Terephthalate Polyester ( PET, PETP ) - Properties and Applications," *AZO Materials*, 2003. [Online]. Available: [https://www.azom.com/article.aspx?ArticleID=2047#:~:text=Polyethylene terephthalate polyester \(PETP\) is a hard%2C stiff%2C,amorphous to fairly high crystalline.](https://www.azom.com/article.aspx?ArticleID=2047#:~:text=Polyethylene terephthalate polyester (PETP) is a hard%2C stiff%2C,amorphous to fairly high crystalline.) [Accessed: 01-Feb-2020].
- [52] "Optical absorption and thermal conductivity of GaAsPN absorbers grown on GaP in view of their use in multijunction solar cells," *HAL Archives*, 2015. [Online]. Available: <https://hal.archives-ouvertes.fr/hal-01166475/document>. [Accessed: 01-Feb-2020].



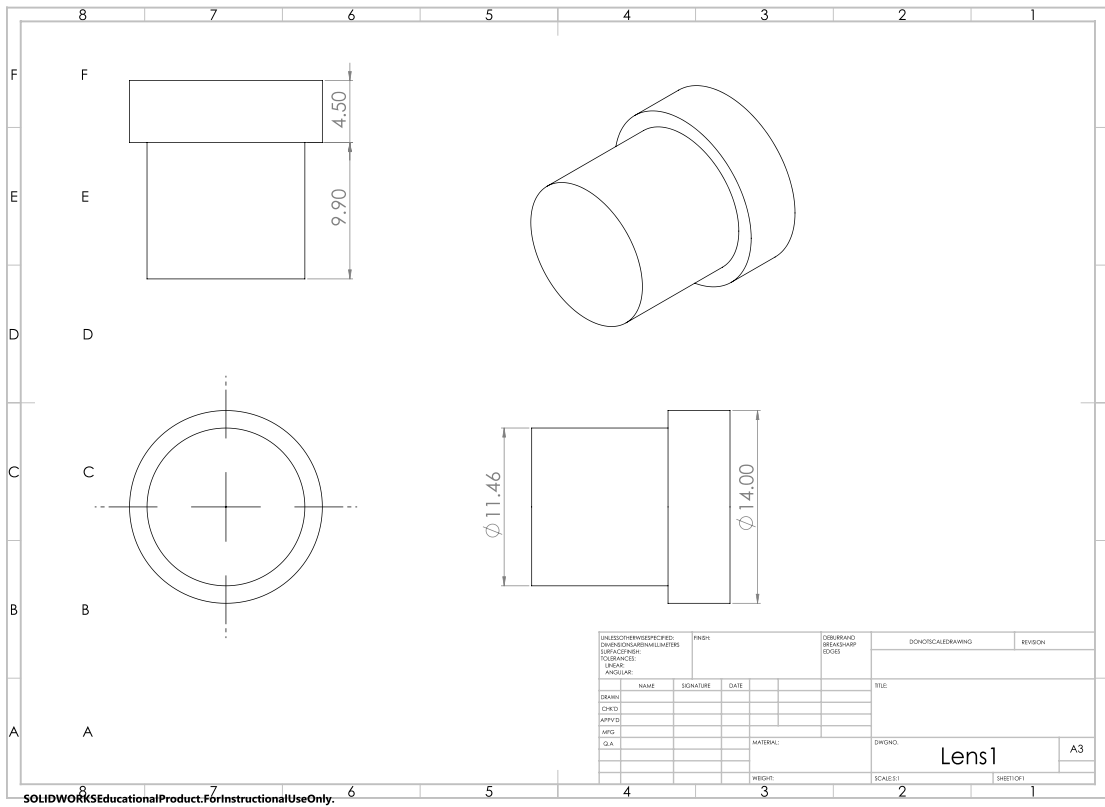


Figure 53: Drawing of Camera Lens

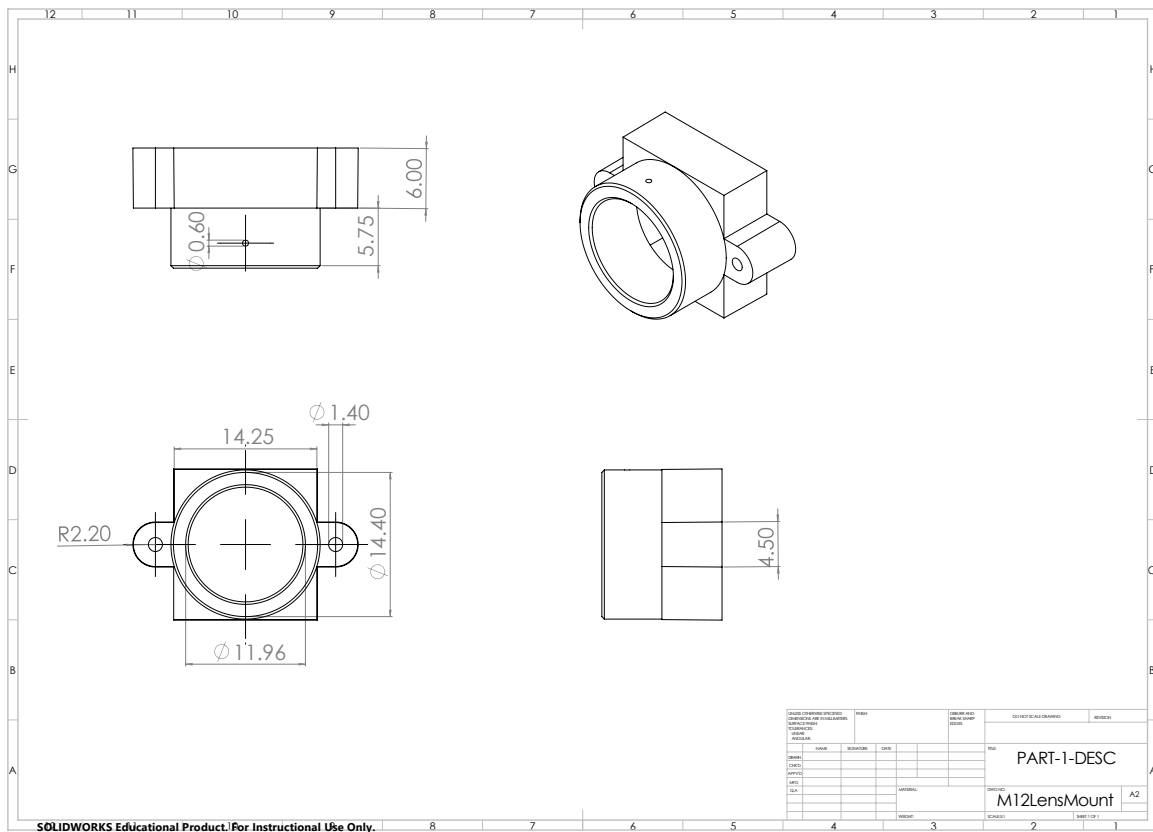


Figure 54: Drawing of Lens Mount

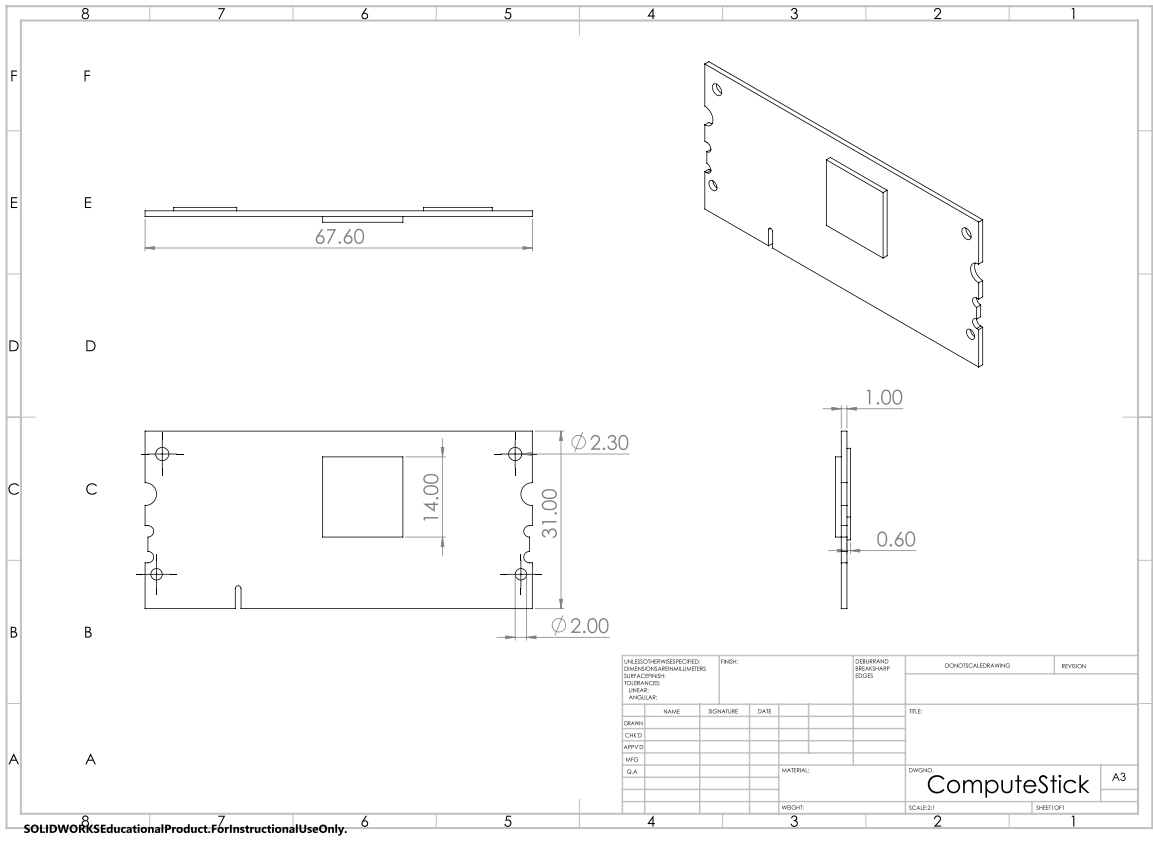


Figure 55: Drawing of Payload Board Compute Stick

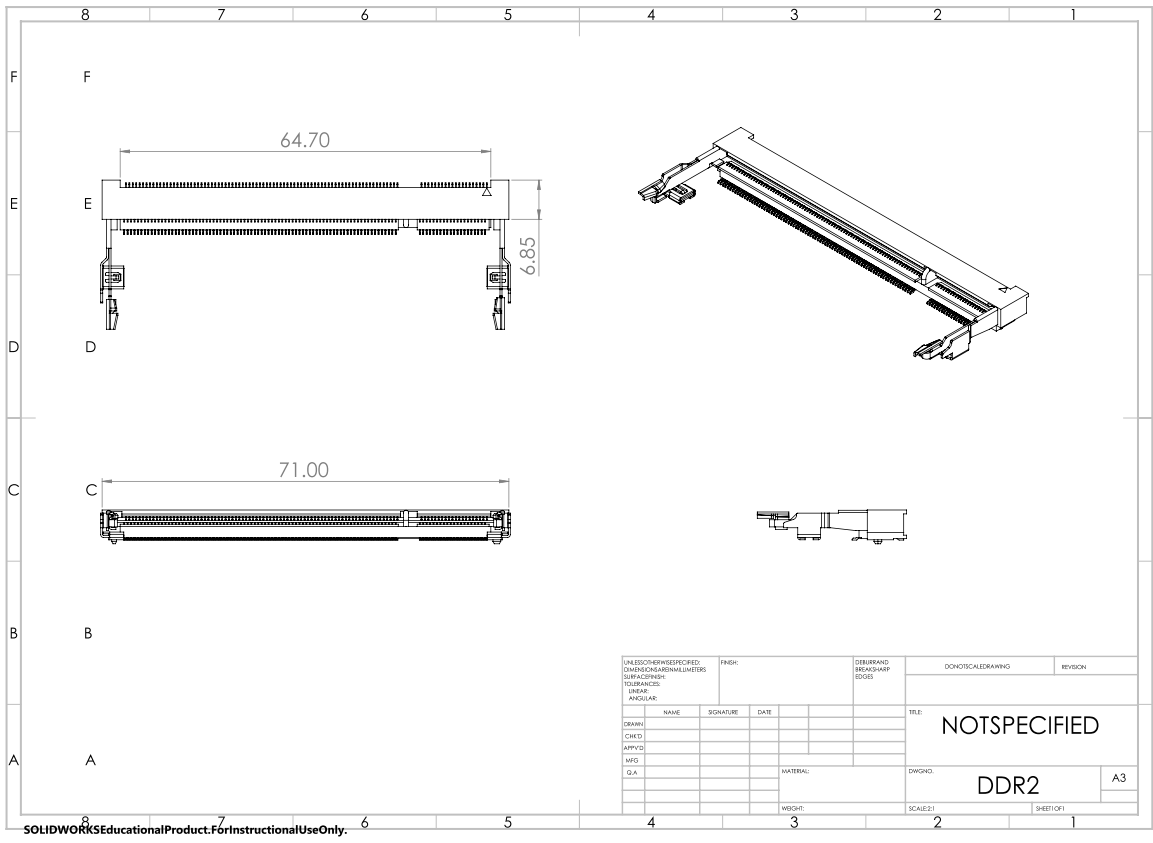


Figure 56: Drawing of DDR2 SRAM

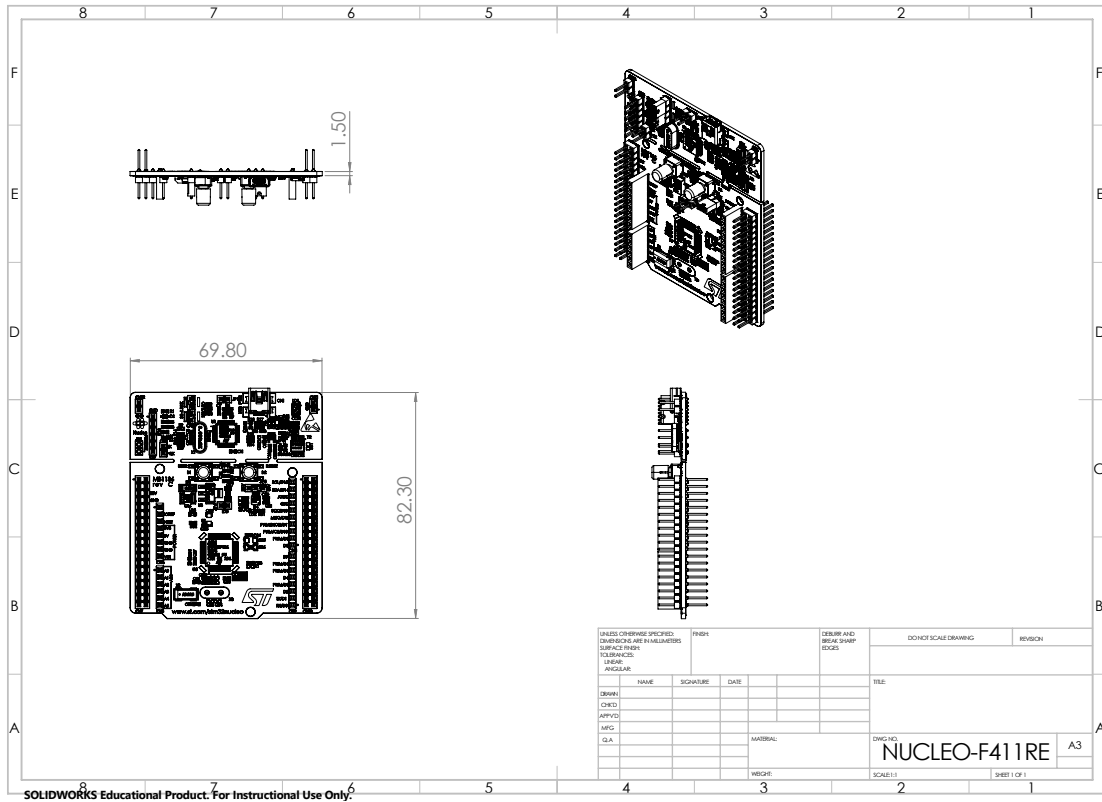


Figure 57: Drawing of Nucleo-64

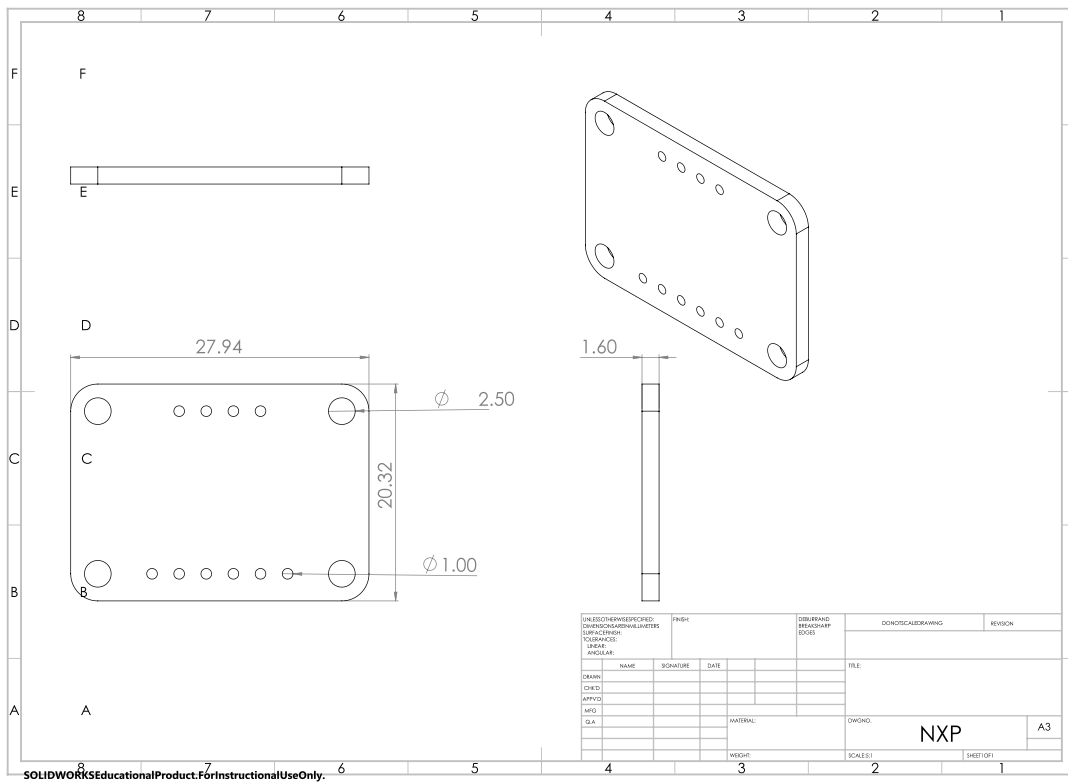


Figure 58: Drawing of NXP



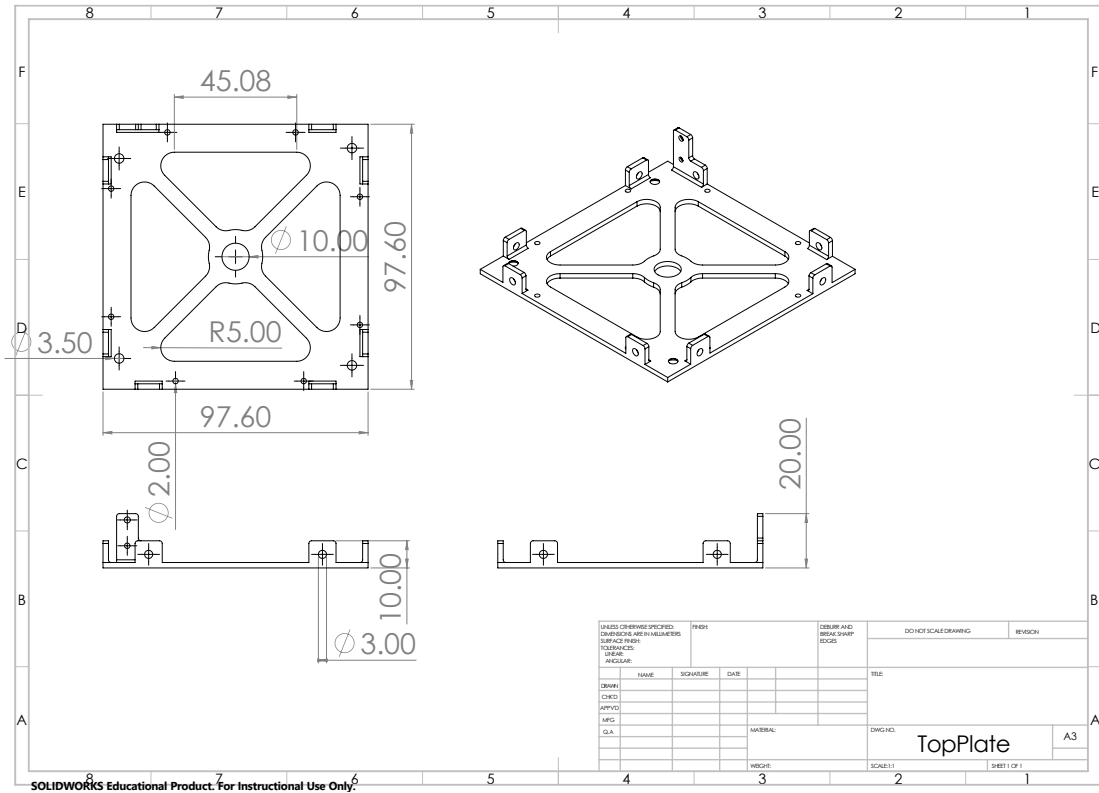


Figure 61: Top Plate Drawing

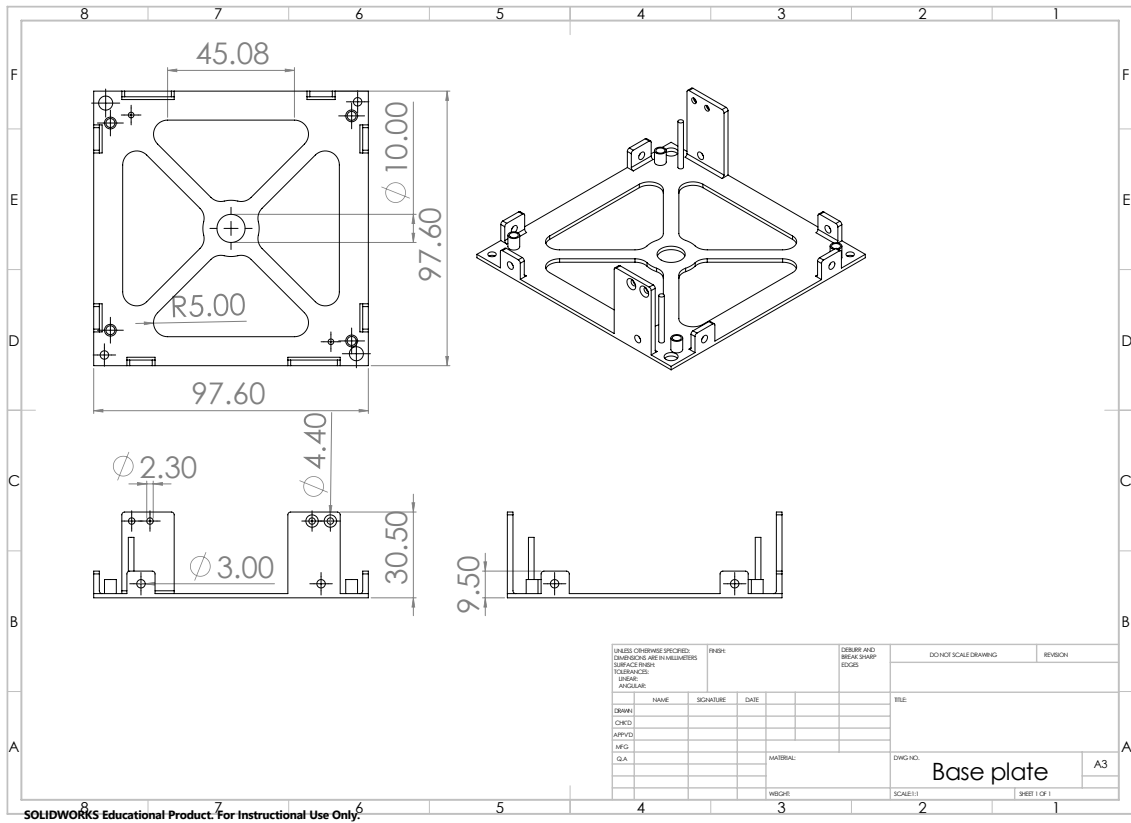


Figure 62: Base Plate Drawing

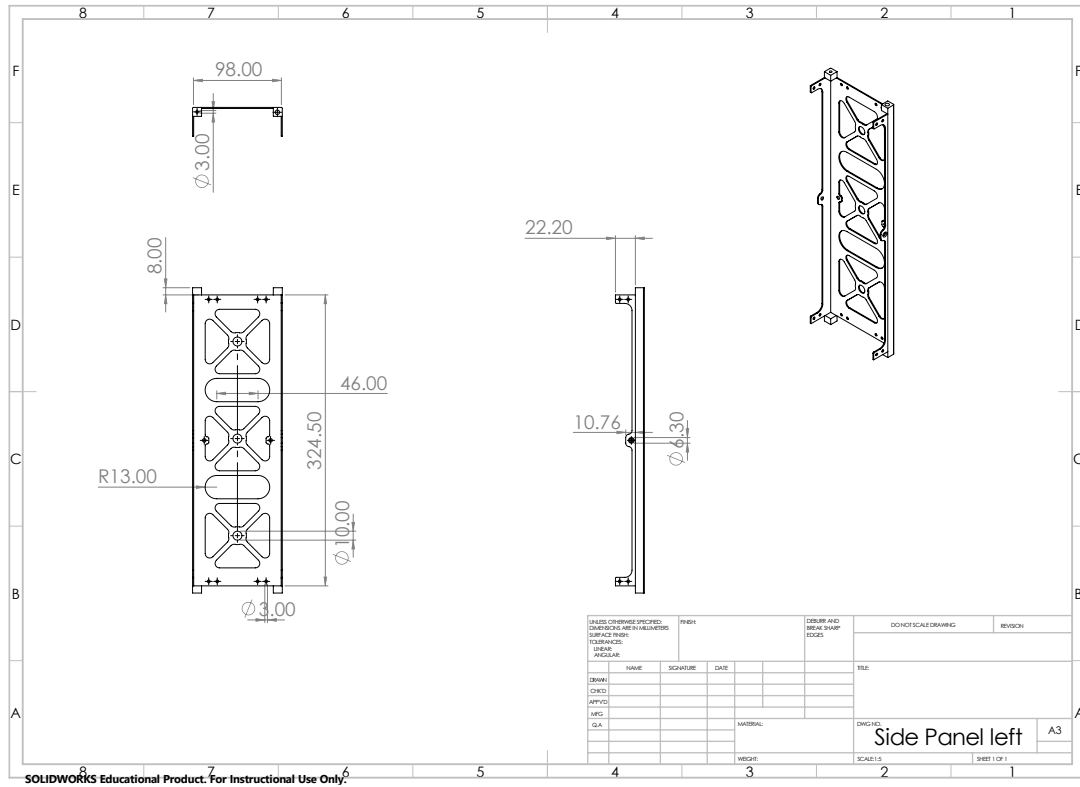


Figure 63: Side Panel Left Drawing

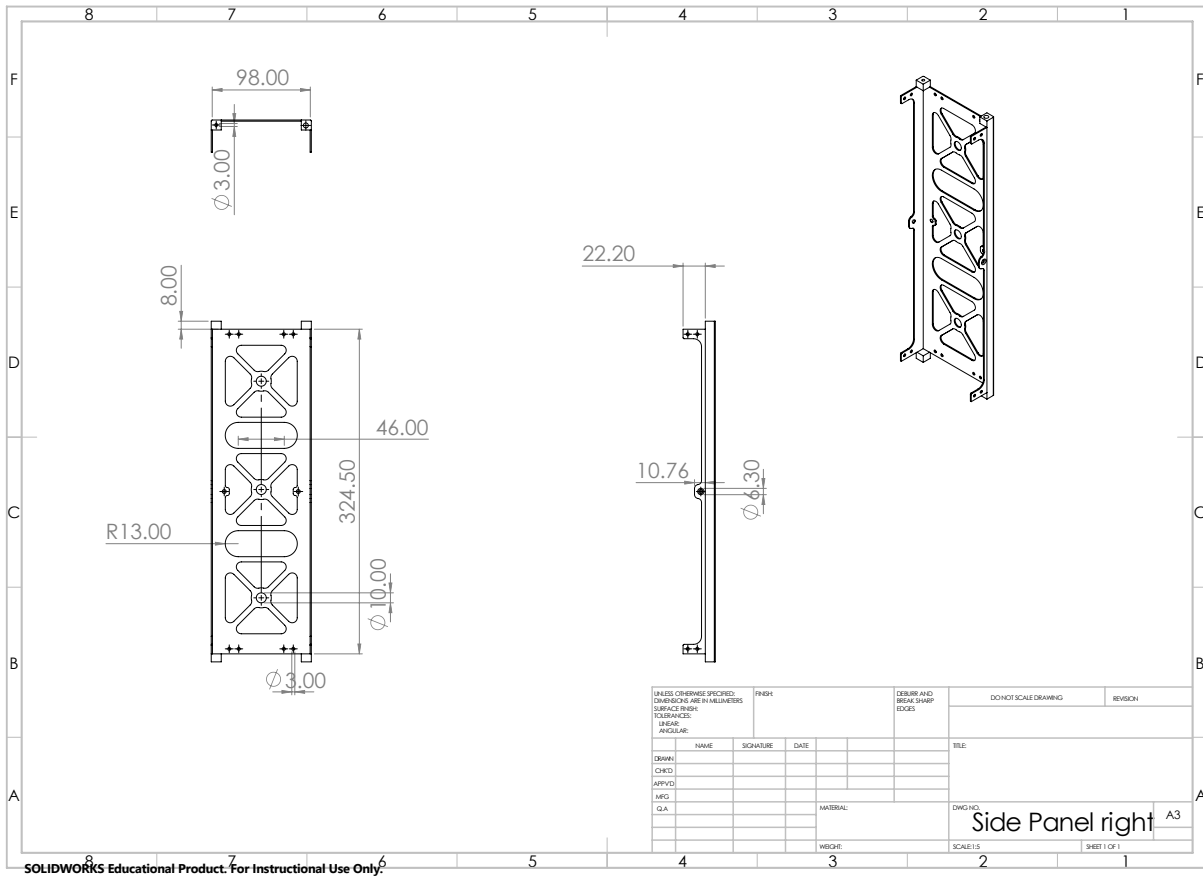


Figure 64: Side Panel Right Drawing



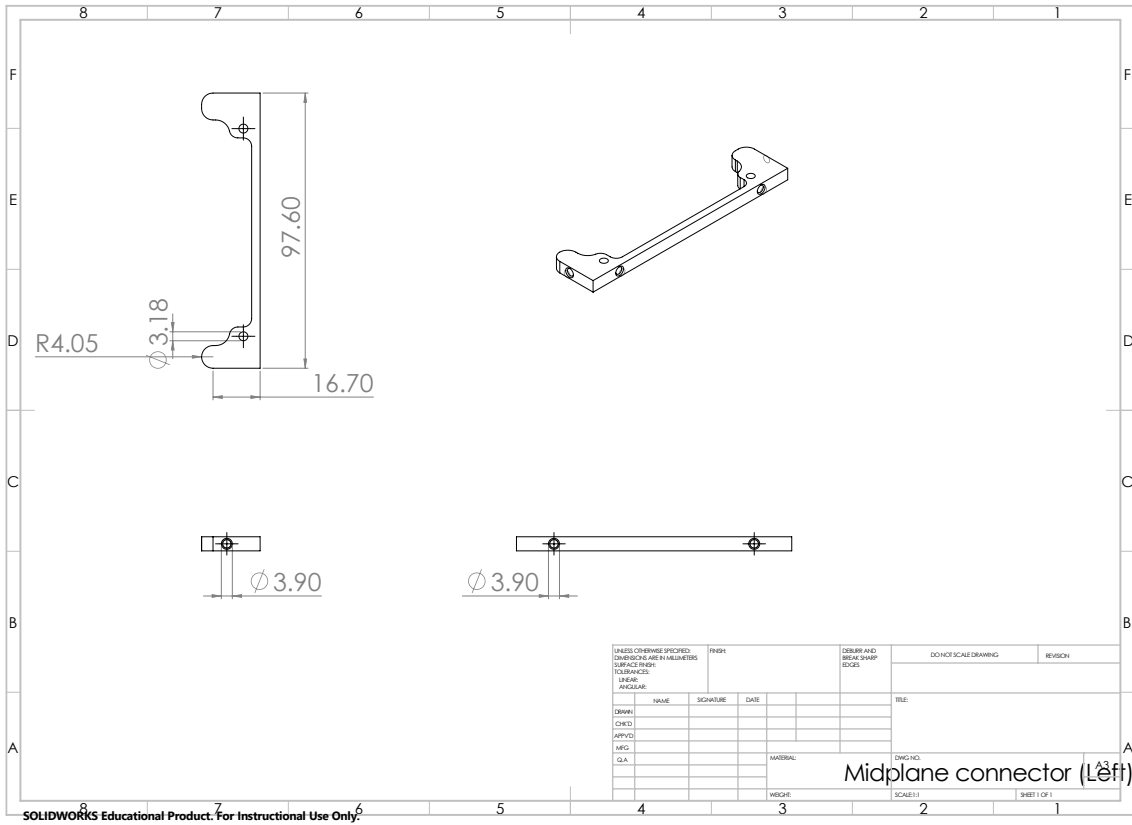


Figure 65: Midplane Connector Drawing

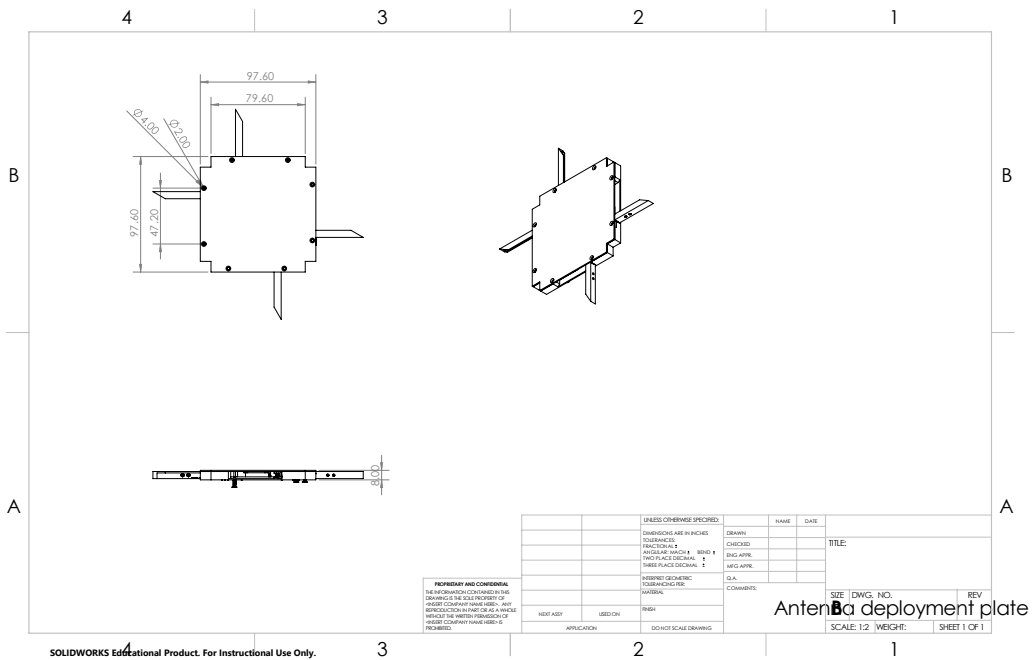


Figure 66: Drawing of ADS

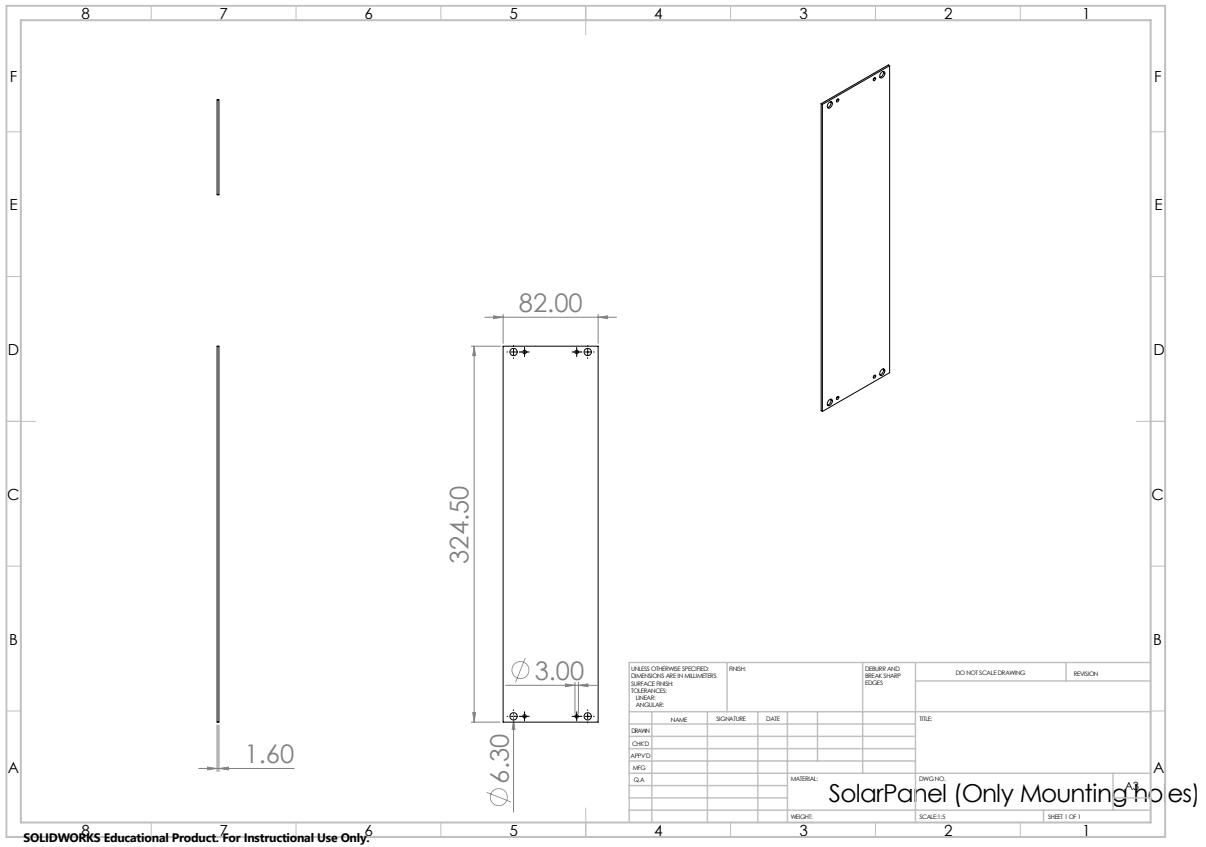


Figure 67: Solar Panel Plate Drawing

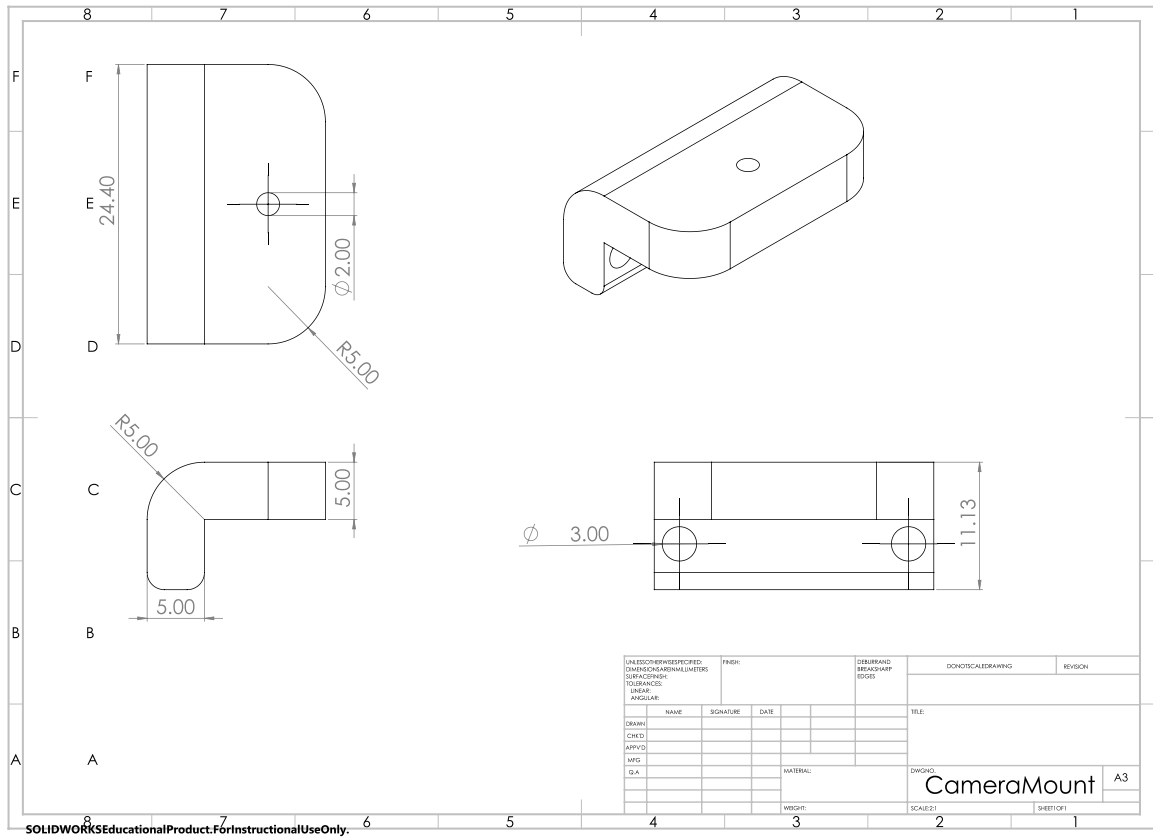


Figure 68: Camera Mount Design

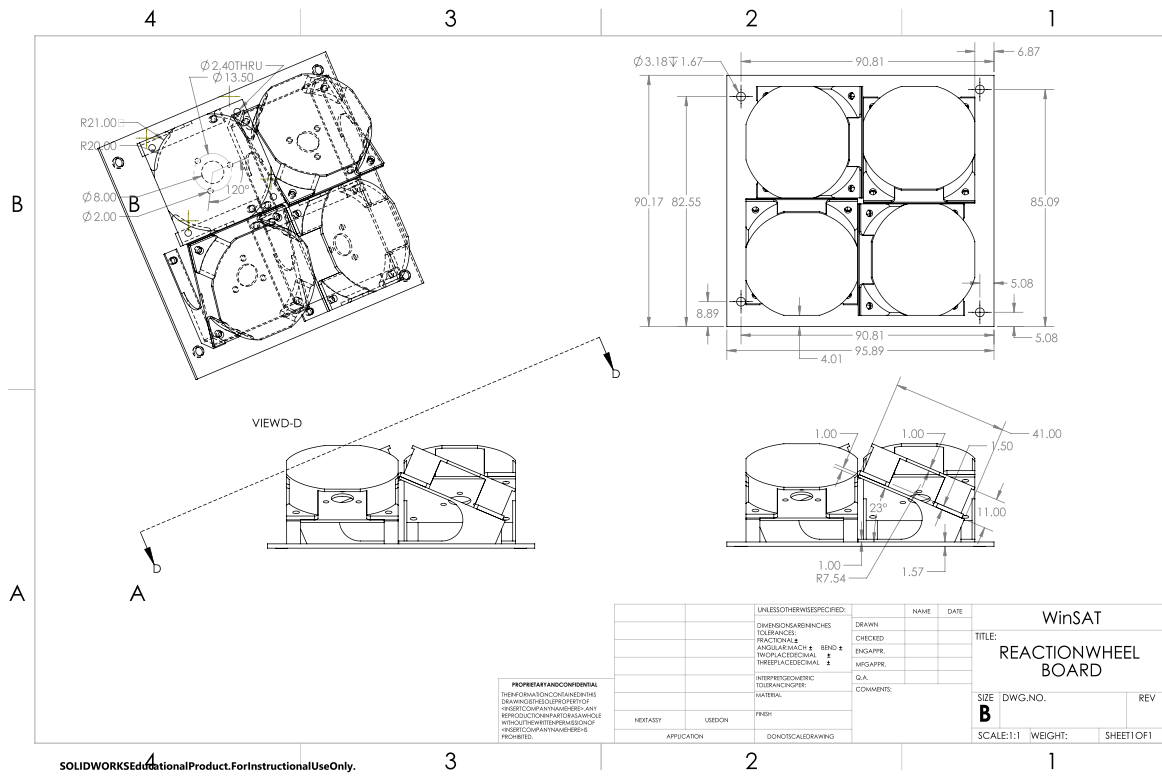


Figure 69: Reaction Wheel Board Schematic

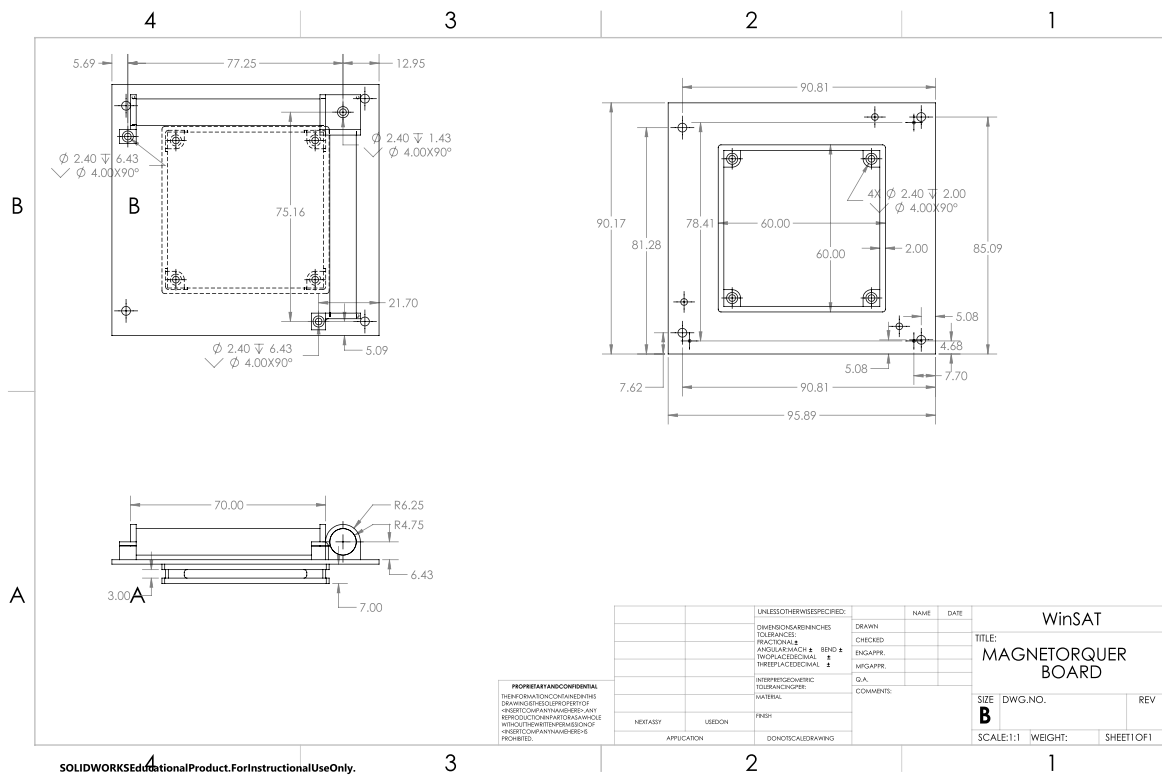


Figure 70: Magnetorquer Board Schematic

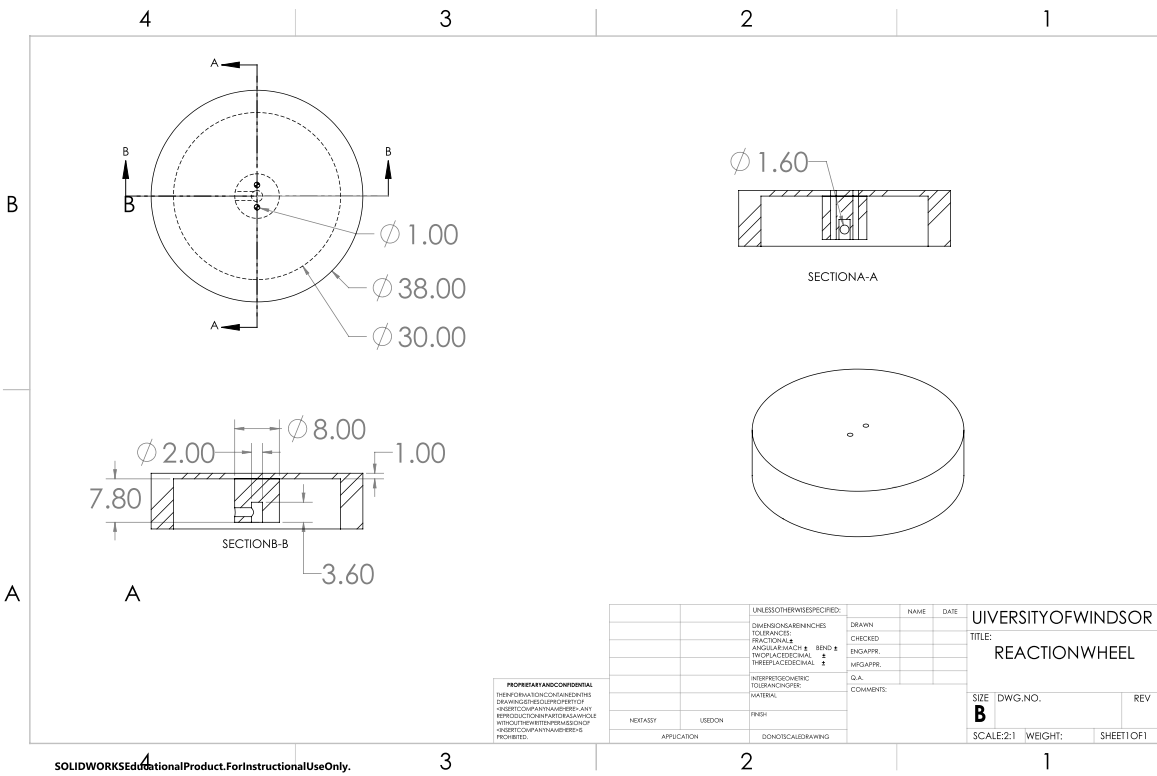


Figure 71: Reaction Wheel Schematic

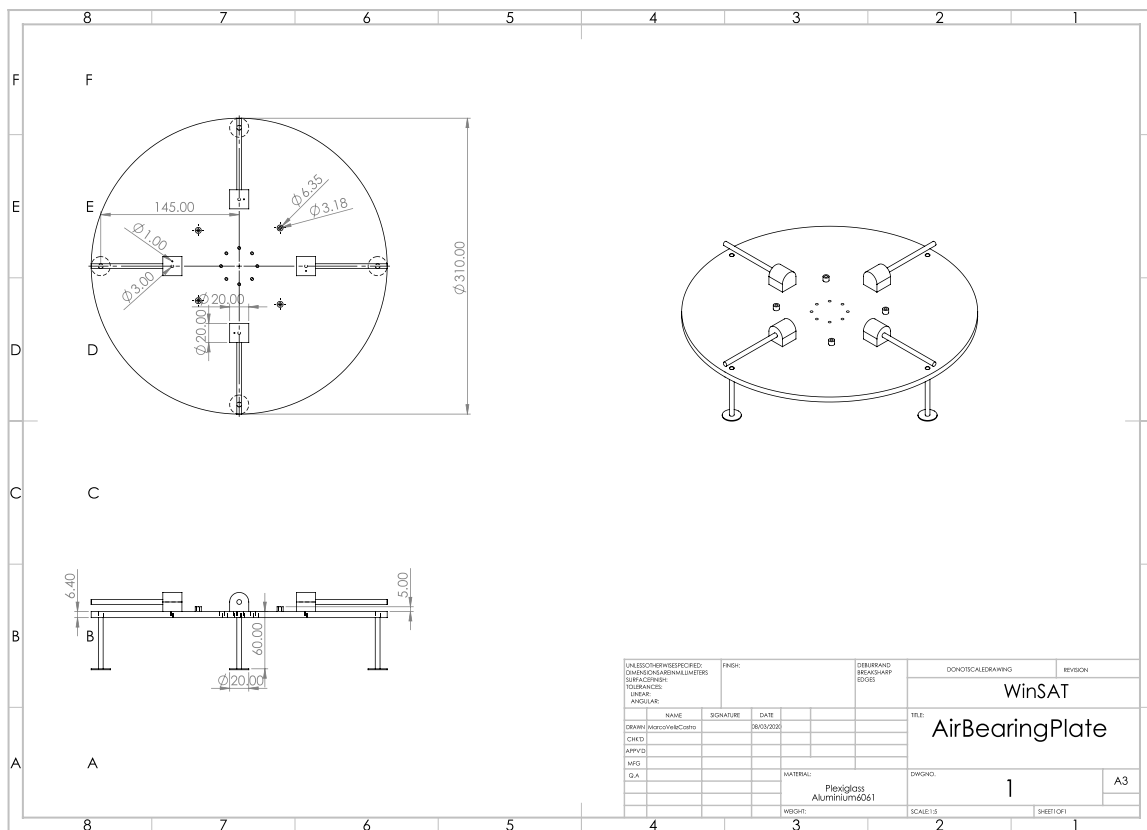


Figure 72: SABB Mounting Plate with 3-Axis Balancing System Schematic

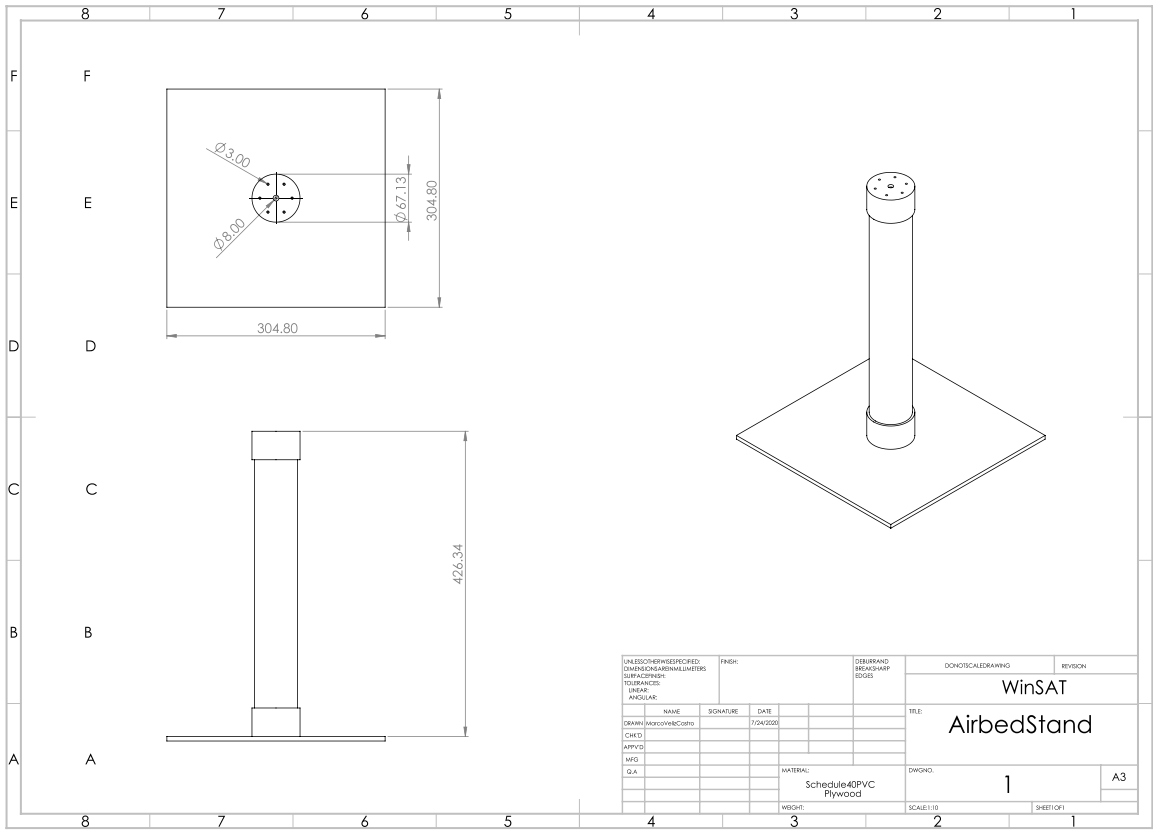


Figure 73: SABTB Platform Schematic

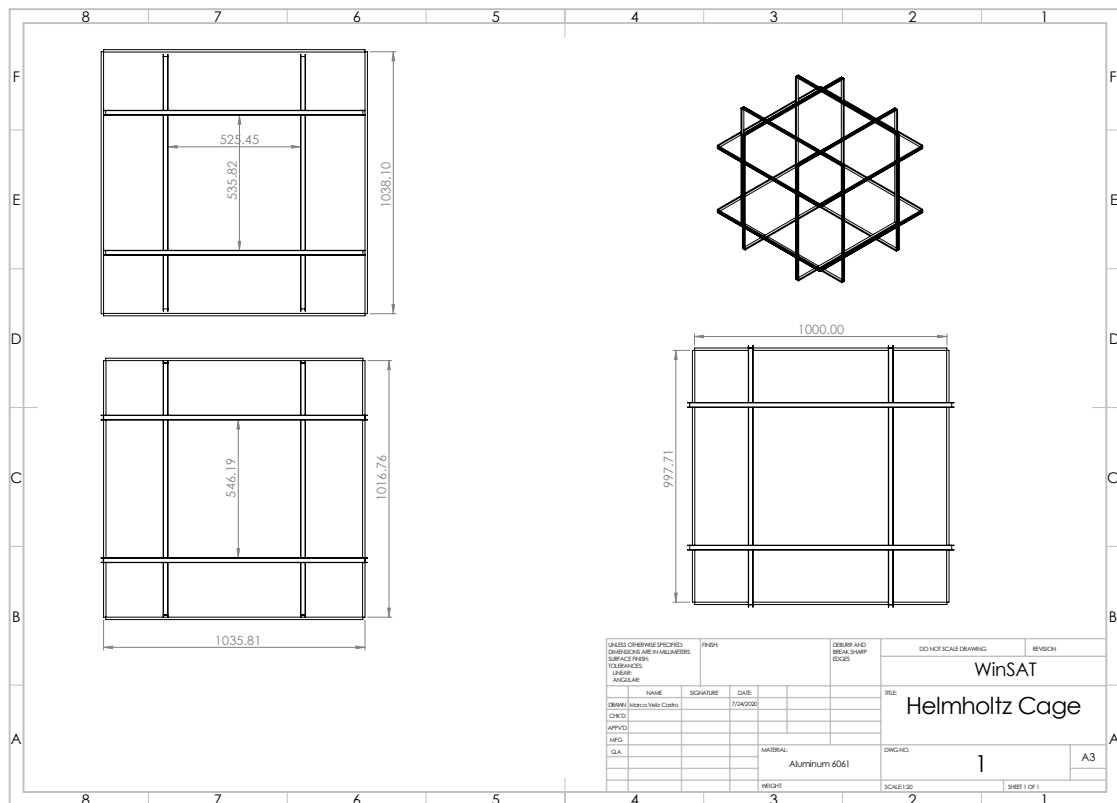


Figure 74: Helmholtz Cage Schematic

## APPENDIX B – STRUCTURAL SIMULATION RESULTS

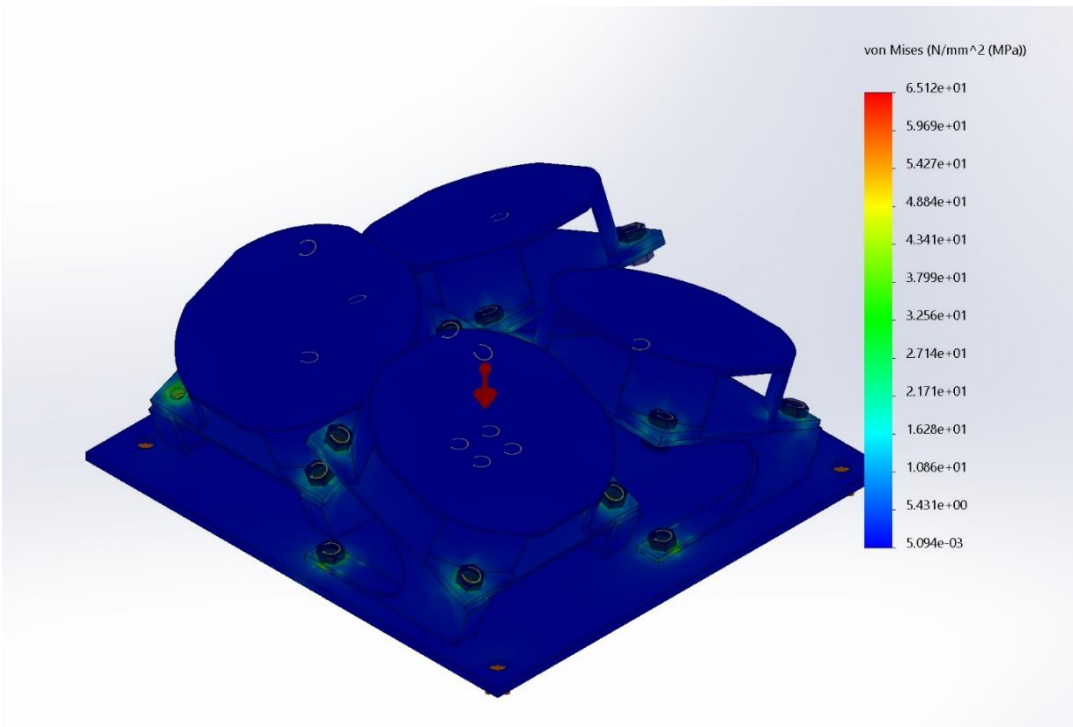


Figure 75: Von-Mises Stress Plot of RW Board Under 12 g Quasi-Static Acceleration

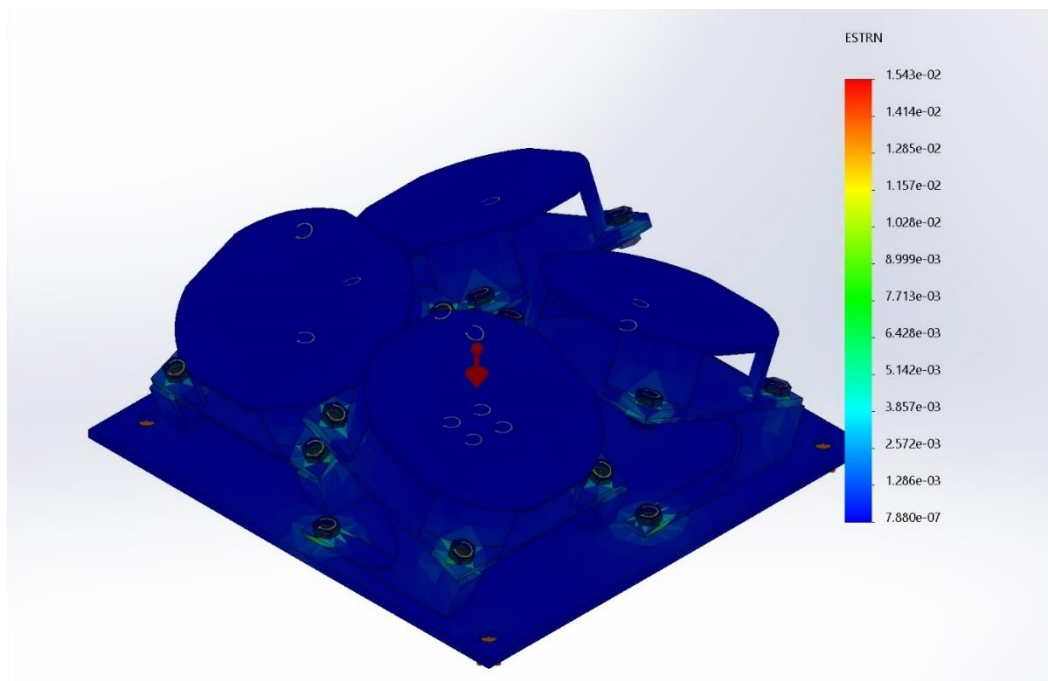


Figure 76: Strain Plot of RW Board Under 12 g Quasi-Static Acceleration

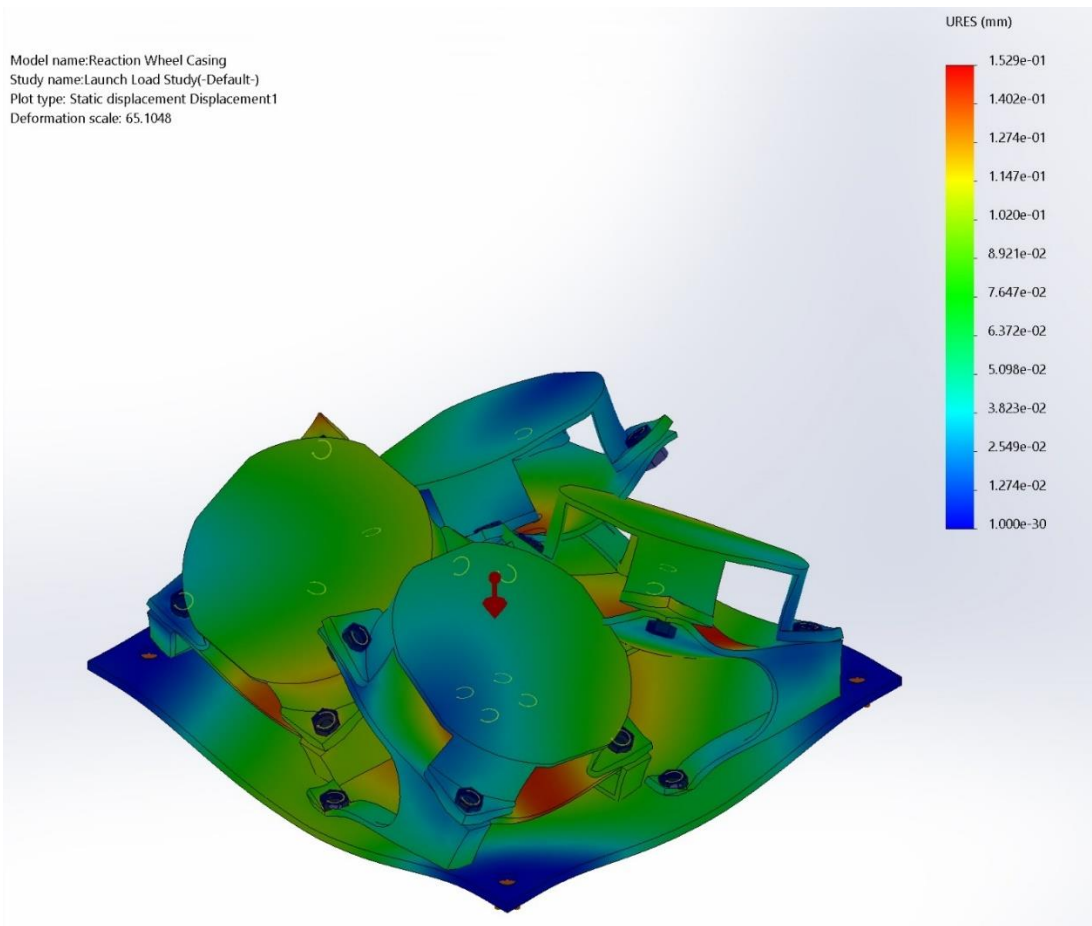


Figure 77: Displacement Plot of RW Board Under 12 g Quasi-Static Acceleration

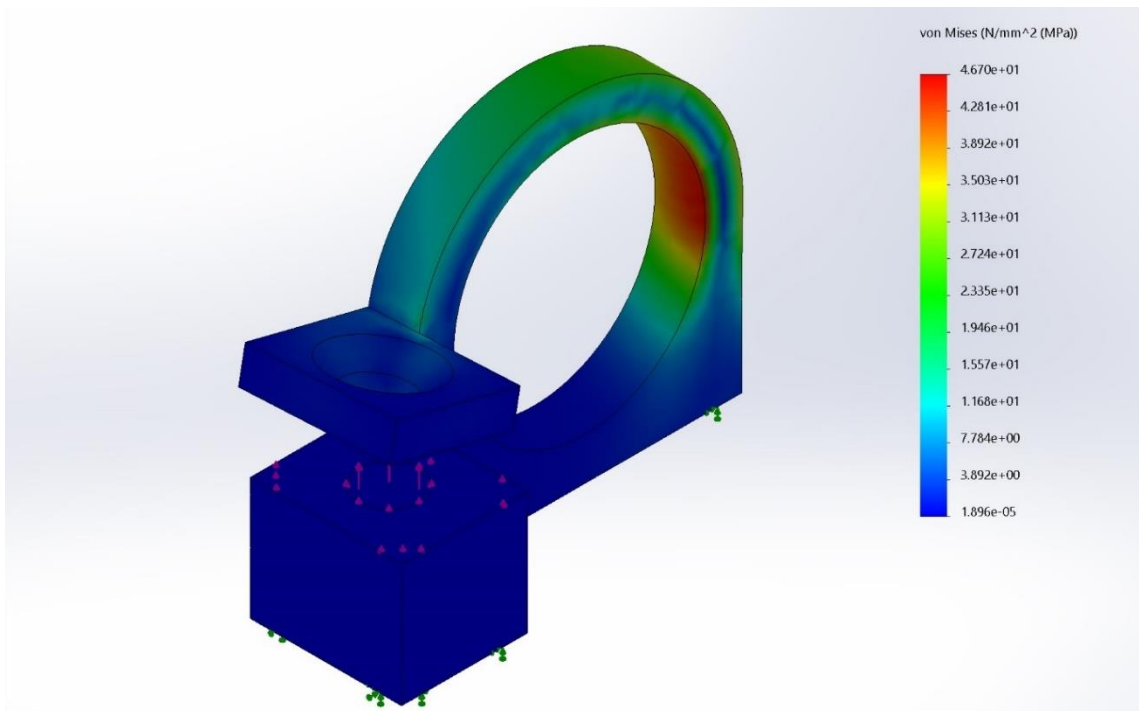


Figure 78: Von-Mises Stress Plot of Magnetorquer Mount Clamp w/ 5N Load

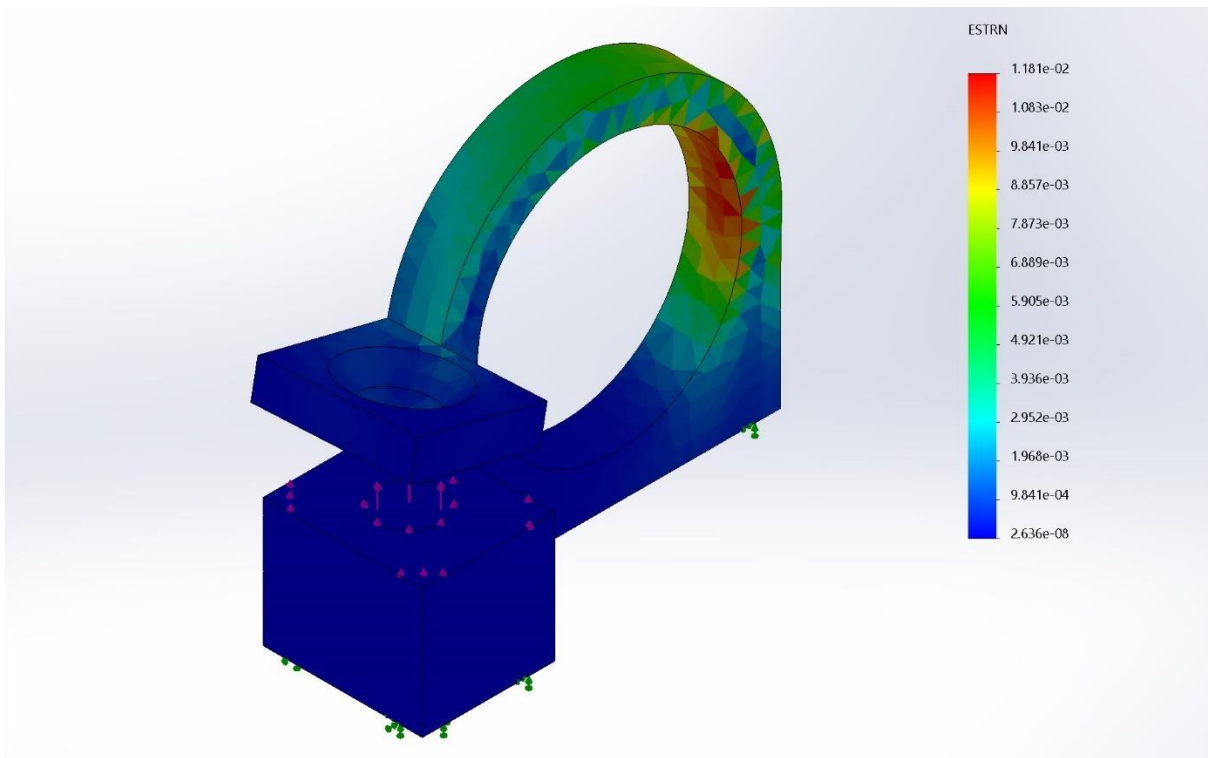


Figure 79: Strain Plot of Magnetorquer Mount Clamp with 5N Load Applied at Opening

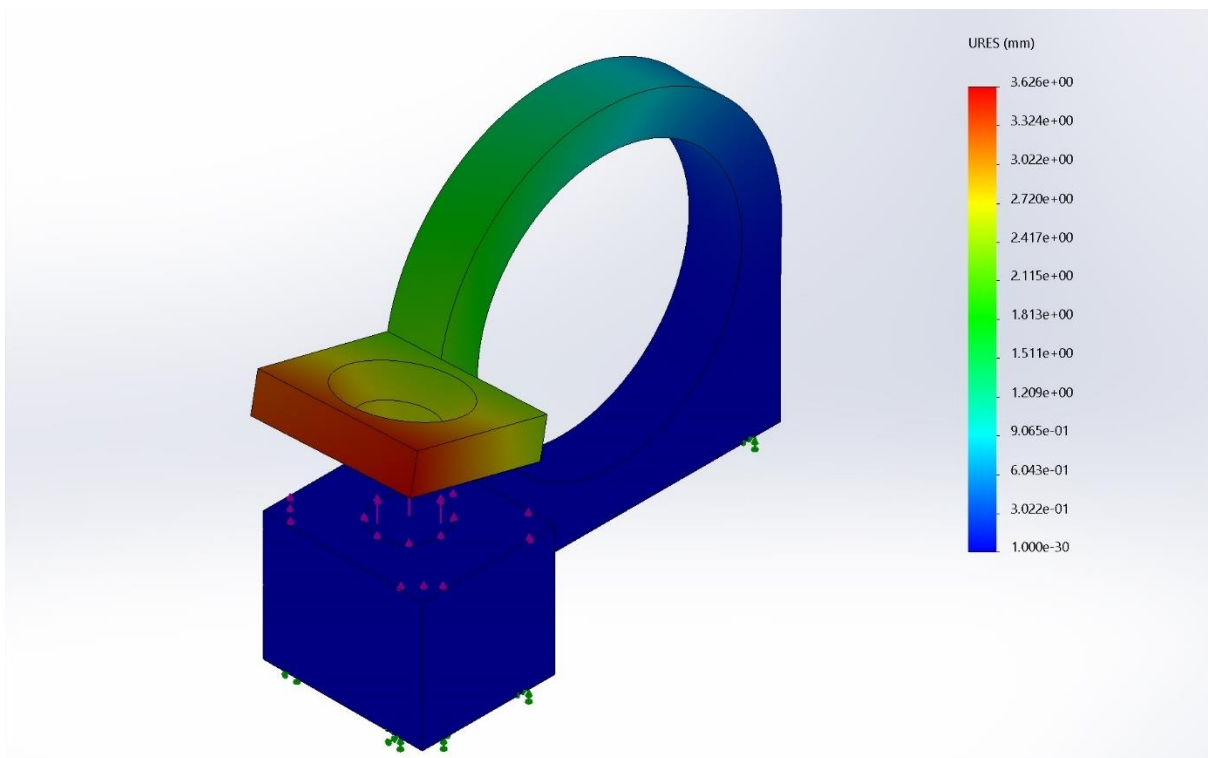


Figure 80: Displacement Plot of Magnetorquer Mount Clamp with 5N Load Applied at Opening



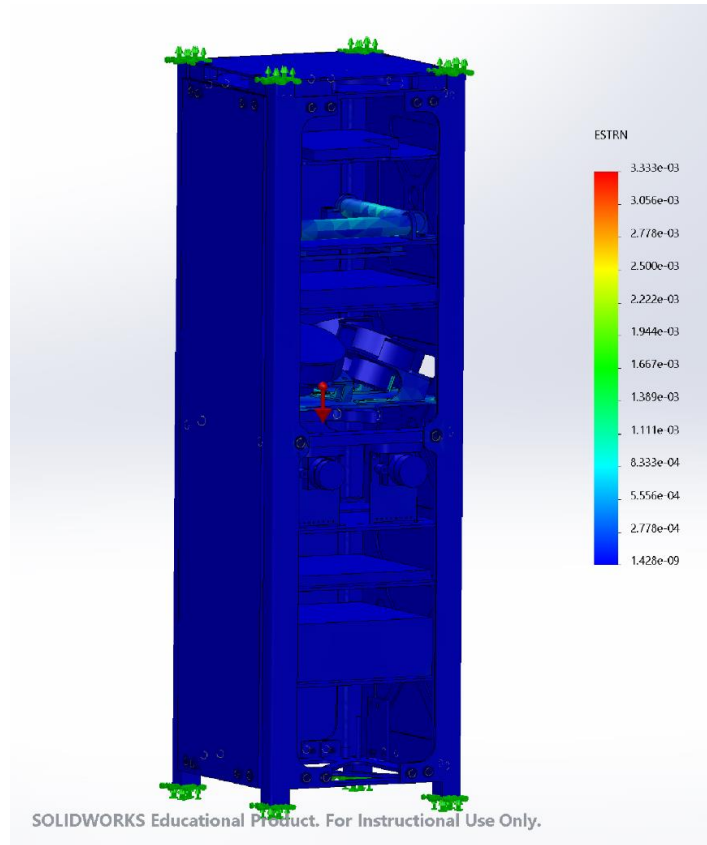


Figure 81: Vertical Loading – Internal Strain Result Example (-Z shown)

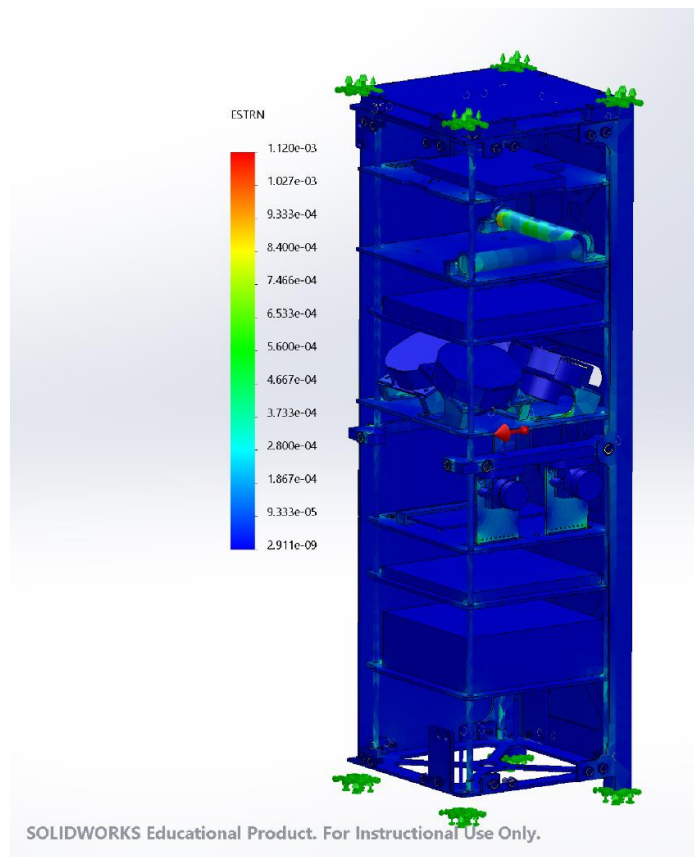


Figure 82: Horizontal Loading – Internal Strain Result Example (-Y shown)

## APPENDIX C – THERMAL SIMULATION RESULTS

Table 17: Temperature Range Results for ISS Hot Case

Component	Maximum Temp (°C)	Minimum Temp (°C)
Solar Panels	73	-54
FR4 Siding	79	-76
MBM2 Chip	29	1
ADCS Chip	20	-10
Payload Chip	34	20
Battery	31	20
Cameras	20	16
RW	30	20
RW Motors	32	20
Magnetorquers	20	-27
MBM2 PCB	29	1
ADCS PCB	20	-10
Payload PCB	34	20
Battery PCB	31	20
RW PCB	20	-3
RW Casing	30	-3
Magnetorquer PCB	20	-27
Antenna Plate	20	-40
Top Plate	20	-40
Bottom Plate	20	-40
Rails	20	-40
Aluminum Siding	20	-40
FR4 Camera Stands	32	19
Midplane Connectors	20	-40

Table 18: Temperature Range Results for ISS Cold Case

Component	Maximum Temp (°C)	Minimum Temp (°C)
Solar Panels	72	-63
FR4 Siding	76	-77
MBM2 Chip	29	-10
ADCS Chip	20	-29
Payload Chip	34	3
Battery	29	10
Cameras	20	10
RW	30	18
RW Motors	31	18
Magnetorquers	20	-45
MBM2 PCB	29	-10
ADCS PCB	20	-29
Payload PCB	34	3
Battery PCB	29	10
RW PCB	20	-21
RW Casing	30	-21
Magnetorquer PCB	20	-45
Antenna Plate	20	-53
Top Plate	20	-53
Bottom Plate	20	-53
Rails	20	-53
Aluminum Siding	20	-53
FR4 Camera Stands	25	8
Midplane Connectors	20	-53

Table 19: Temperature Range Results for Sun-Synchronous Hot Case

Component	Maximum Temp (°C)	Minimum Temp (°C)
Solar Panels	61	-56
FR4 Siding	74	-72
MBM2 Chip	33	-3
ADCS Chip	20	-29
Payload Chip	29	18
Battery	31	13
Cameras	20	12
RW	34	20
RW Motors	36	20
Magnetorquers	20	-26
MBM2 PCB	33	-3
ADCS PCB	20	-29
Payload PCB	29	18
Battery PCB	31	13
RW PCB	20	-11
RW Casing	35	-11
Magnetorquer PCB	20	-26
Antenna Plate	20	-46
Top Plate	20	-46
Bottom Plate	20	-46
Rails	20	-46
Aluminum Siding	20	-46
FR4 Camera Stands	24	17
Midplane Connectors	20	-46

Table 20: Temperature Range Results for Sun-Synchronous Cold Case

Component	Maximum Temp (°C)	Minimum Temp (°C)
Solar Panels	57	-57
FR4 Siding	65	-73
MBM2 Chip	31	-4
ADCS Chip	20	-30
Payload Chip	28	18
Battery	30	13
Cameras	20	9
RW	32	20
RW Motors	34	20
Magnetorquers	20	-28
MBM2 PCB	31	-4
ADCS PCB	20	-30
Payload PCB	28	18
Battery PCB	30	13
RW PCB	20	-12
RW Casing	33	-12
Magnetorquer PCB	20	-28
Antenna Plate	20	-48
Top Plate	20	-48
Bottom Plate	20	-48
Rails	20	-48
Aluminum Siding	20	-48
FR4 Camera Stands	22	16
Midplane Connectors	20	-48

## APPENDIX D – CAD MODELS

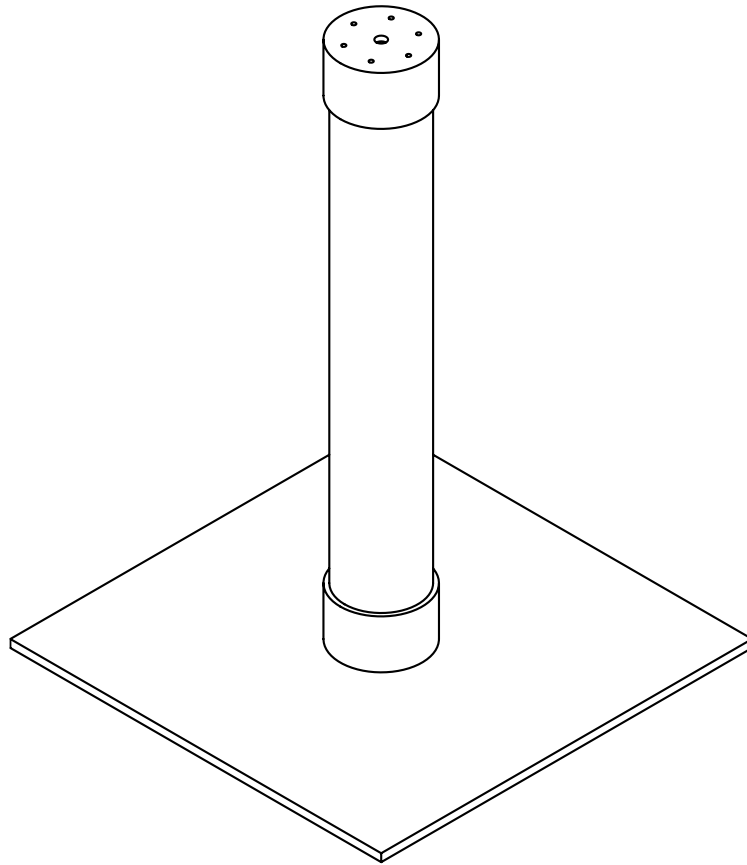


*Figure 83: CAD Model of SABTB Platform*

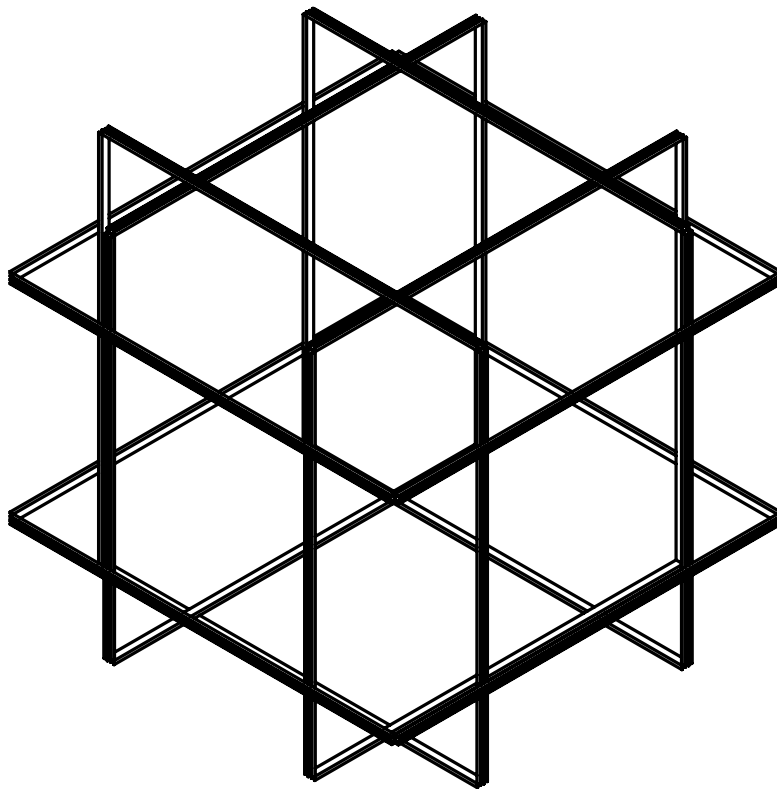


*Figure 84: CAD Model of Helmholtz Cage*

